Surface Micromachined Electrostatic Actuators

Dissertation
submitted to the Faculty of Sciences of the University of Neuchâtel
to obtain the degree of Doctor of Science

by

Victor P. Jaecklin

Dipl. Phys. ETHZ

Institute of Microtechnology
University of Neuchâtel
Rue A.-L. Breguet 2
CH-2000 Neuchâtel
Switzerland

printed by Imprimerie Moser SA
CH-2001 Neuchâtel

To My Parents

for love,

encouragement,

and support

IMPRIMATUR POUR LA THÈSE

Surface Micromachined Electrostatic

Actuators

de Monsieur Victor Jaecklin

UNIVERSITÉ DE NEUCHÂTEL

FACULTÉ DES SCIENCES

La Faculté des sciences de l'Université de Neuchâtel
sur le rapport des membres du jury,
Messieurs N. de Rooij, R. Dändliker,
P. Vettiger (IBM Rüschlikon) et
Ph. Renaud (EPF-Lausanne)
autorise l'impression de la présente thèse.

Neuchâtel, le 12 janvier 1994

Le doyen:

H.-H. Nägeli

Abstract

This thesis deals with the design, fabrication, and characterization of surface micromachined electrostatic actuators.

The presented devices are surface micromachined in single crystal silicon, polycrystalline silicon, and aluminum. For particular structures, also a combination of silicon bulk and surface micromachining has been employed. The characterization points out that silicon and polysilicon devices present higher yield strains but also higher processing temperatures and switching voltages; on the other hand, aluminum has higher surface reflectivities.

We have fabricated and operated comb actuators with submicrometer wide beam suspensions. They prove to be reliable micromechanical devices, which can perform controlled one-dimensional positioning at low voltages. Displacements of up to 7 µm are achieved for voltages lower than 15 V. For two-dimensional positioning, a comb-driven *xy*-nanopositioner has been devised. Experiments show that the current design can be used for positioning in the range of several micrometers, where the absolute position error due to the mechanical coupling of the two actuation directions is lower than 80 nm. This accuracy can be improved considerably if compensation for the interdependence of the displacements in *x*- and *y*-direction is employed. By combining bulk and surface silicon micromachining, an integrated scanning local probe unit has been fabricated for applications in nanoscale science and technology.

Torsional micromirrors have been conceived, which can be used to deflect incoming laser beams. In view of laser printing and projection displays, a 32 by 32 micromirror array has been fabricated. Optical microshutters allow to interrupt a focused laser beam of 5 µm in diameter. If operated in transmission mode, high contrast ratios are obtained and only a simple optical setup is required for the applications mentioned above. Finally, interference light modulators are presented. They are used to change either the height of a phase step or the width of an optical resonance cavity for a Fabry-Perot interferometer. These devices modulate light at high speed - the bandwidth of operation is typically above 1 Mhz.

Contents

List of Notations

Symbol	Description	Unit
γ	angle	rad
ε	strain	
ε_{el}	electric permittivity	C/Vm
ε_0	free space permittivity	8.85 10^{-12} C/Vm
ε_c	buckling strain	
ε_r	relative permittivity	C/Vm
ε_x	strain in x-direction	
ϕ	angle	rad
Φ	electric potential	V
ρ	density	kgm^{-3}
ρ_{el}	electric charge density	Cm^{-3}
ρ_Q	heat generation rate	J/m^{3}s
σ	stress	Nm^{-2}
σ_{el}	electric surface charge density	Cm^{-2}
τ	shearing stress	Nm^{-2}
τ_d	time constant of damping	s
Θ	twist per unit length	radm^{-1}
θ	rotation	rad
A	area	m^2
A_f	anisotropy of etching	
$A(f)$	amplitude at frequency f	m
b	length	m
C	capacitance	F = CV^{-1}
c	maximum distance from neutral axis	m
d	distance	m
$\boldsymbol{E}$	electric field	Vm^{-1}
E	Young's modulus	Nm^{-2}
$E(p)$	complete elliptic integral of first kind	
e	length of edge	m

$F_{b,g,w}$	force in b,g,w-direction	N
F	force	N
f	frequency	s^{-1}
f_l	natural frequency	s^{-1}
f_{res}	resonance frequency	s^{-1}
G	modulus of torsion	Nm^{-2}
g	gap	m
h	width of optical resonance cavity	m
Δh	height of phase step	m
I	mass moment of inertia	Nms^2
I_p	polar moment of inertia	m^4
I_t	torsional moment of inertia	m^4
$I_{x,y,z}$	area moment of inertia (around x,y,z-axis)	m^4
k	spring constant	Nm^{-1}
$k_{x,y,z}$	spring constant in x,y,z-direction	Nm^{-1}
K	thermal conductivity	W/Km
$K(p)$	complete elliptic integral of second kind	
L	length of beam	m
L_p	projection length of beam	m
$L_{1,2}$	length of beam 1, beam 2	m
l	overlap	m
M_c	mass of central piece	kg
M_b	mass of supporting beams	kg
$M(x,y)$	bending moment of beam at location (x,y)	Nm
m	constant (depending on boundary conditions)	
n	number of fingers	
Q	quality factor	
q	electric charge	C = As
r	radius	m
$r(x,y)$	radius of curvature at location (x,y)	m
r_m	mirror reflectance	
R	total reflectance	
S	surface	m^2
T_e	electric torque	Nm
T_m	mechanical torque	Nm
T	temperature	K
U	potential energy	J = Nm

t	thickness	m
V	volume	m^3
V	voltage	V
V_1	switch voltage	V
V_2	release voltage	V
V_c	hold voltage	V
V_d	height of voltage pulse	V
v_l	lateral etch rate	ms^{-1}
v_v	vertical etch rate	ms^{-1}
w	width	m
Δx, Δy, Δz	displacement in x,y,z-direction	m
$y(x)$	deflection of beam as function of x	m

Abbreviations

BHF	buffered hydrofluoric acid
CCD	charge coupled device
CMOS	complimentary metal-oxide-semiconductor field-effect transistor
COMETT	Community Programme for Education and Training in Technology
CSEM	Swiss Center for Electronics and Microtechnology Inc.
CVD	chemical vapor deposition
FSRM	Swiss Foundation for Microtechnology Research
IMT	Institute of Microtechnology
IC	integrated circuit
FEM	finite element modelling
LIGA	Litographie, Galvanoformung, Abformung
LPCVD	low pressure chemical vapor deposition
MEMS	microelectromechanical system
PGA	pin-grid array
PSG	phosphosilicate glass
RIE	reactive ion etching
SEM	scanning electron microscope
SFB	silicon fusion bonding
SFM	scanning force microscope

SRAM	static random-access memory
UETP	University Enterprise Training Partnership

Chapter One

Introduction

The overall performance of microelectronic elements has been increased since 1960 by about ten orders of magnitude. This has led to the wide use of microelectronics in computing, data storage, process control, and many other domains. The potential of new applications based on megabit memories and new types of processors is not exhausted yet. But it seems that the further penetration of microelectronics into new products is hampered by the lack of miniaturized sensors and actuators, which are able to master the tasks of automatic, multidimensional data acquisition, and process control. It will be important that these new devices are compatible with microelectronic elements in driving voltage, dimensions, complexity, and prize. This work is devoted to the development of electrostatic microactuators which could become part of such integrated microsystems.

The introduction chapter will place the work in a larger context. For this purpose, promising industrial applications for microactuators are described; then, a brief overview of the main micromachining techniques as well as the microactuation principles is given. Further, the state of research at the Institute of Microtechnology (IMT) and the Swiss Center for Electronics and Microtechnology Inc. (CSEM) at the beginning of this project is discussed, and its evolution is presented. Finally, the contents and the structure of this thesis are outlined.

1.1 Applications for Microactuators

Microactuators will not only be compatible with the processing power of microelectronics, but they will also have inherent advantages compared to their macromechanical correspondences such as speed, accuracy, and gentleness of operation [1.1]. Therefore, promising applications for microactuators in the near future are believed to be in fluidics, handling of cells and macro molecules, micro optics, positioning, and the surface analysis as well as the surface modification by microprobe devices [1.2]. All these applications have in common that only light objects like valves, cells, microprobes, or mirrors have to be moved, and therefore, small output forces are sufficient for operation.

In fluidics, research on ink jet printer nozzles has been initiated in the mid 1970s [1.3]. Using anisotropic etching techniques, these nozzles were fabricated, and soon they were combined with an ink cavity and a piezoelectric pressure oscillator to form a micromachined printing head [1.4]. Other research in fluidics concentrates on the fabrication of valves and pumps [1.5]. Recently, sophisticated devices such as a bioreactor for space research have been presented, where pumps, valves, flow sensors, and chemical sensors have been integrated into one microsystem [1.6].

Typical dimensions of biological objects are around 1-10 μm for cells and several nanometers in thickness by a few micrometers in lengths for macromolecules. The electric field distribution obtained by microfabricated electrodes can be controlled on the same length scale and is suitable for manipulating such objects [1.7, 1.8].

Precise positioning is an important technological field. Macromechanical servo motors and piezoelectric drives are two methods used frequently for achieving the required precision [1.9]. Micromachined electrostatically driven devices may be an interesting alternative. In the following chapters, we discuss one- and two-dimensional comb-driven positioners for this purpose.

For scanning microprobes, especially the tips and cantilevers have been microfabricated for a few years already [1.10-1.13]. Based on these successes, integrated scanning force sensor units have been realized recently [1.14-1.16]. A part of this work is also focused on the fabrication of micromachined tools for nanoscience. Particularly, a scanning unit with integrated probe tip will be presented, which is actuated by the comb-driven two-dimensional positioner.

Micro optical applications range from optical fiber switches [1.17] and optical fiber aligners [1.18, 1.19] over tunable Fabry-Perot interferometers [1.20, 1.21] to arrays of pivoting micromirrors [1.22]. To an important extent, the present work is dedicated to the realization and characterization of micromachined optical devices. In particular, optical shutters, pivoting mirrors, and interference light modulators will be described.

While there is a wide variety of possible applications for microactuators and a lot of research going on in these domains, there are only few commercially successful devices so far. This is in contrast to micromachined sensors, where already a substantial market is existing. A report from Market Intelligence estimates that in 1991 revenues for the world micromachines market reached 870 million US dollars, with a growth rate of 14.5% over the previous year [1.23]. For 1998, a market size of 2.9 billion dollars is expected, with an annual compound growth rate of 19.1%. In an earlier study by Nova Sensors, the share of microactuators on the 1988 micromachines market is estimated to be less than one percent [1.24]. This situation may not have changed much since then. However, the introduction of micromachined actuators and robots in higher volumes is expected in early 1995 (Market Intelligence).

1.2 Micromachining

Silicon micromachining has become the fundamental technology for the fabrication of microsensors and microactuators. Micromachining techniques include the basic processing steps of integrated circuits (IC) technology, namely, thin film growth, doping, lithography, and patterning. In addition, they incorporate special etching, deposition, and bonding processes, which allow for the sculpturing of three-dimensional microstructures. The main silicon micromachining techniques fall into two categories: bulk micromachining and surface micromachining.

First developments in bulk and surface micromachining have been performed in the 1950s and 1960s respectively. Bulk but also surface micromachining are widely used for the fabrication of microsensors and actuators at a production level [1.25-1.28]. The development as well as the current state of the two technologies will be discussed in the introduction of Chapter 3. Electroplating is an important supplement to micromachining. Initially, it was mainly employed for the fabrication of thin film heads for magnetic recording [1.29]. In recent years, this method is applied to the fabrication of micro electromechanical systems (MEMS). Microstructures made of electroplated metals on silicon substrates have been demonstrated. The patterning of the metal is given by the electroplating mold. Mainly two methods are successful for creating the mold: either a polyimide is structured by conventional lithography [1.30], or a polymethyl methacrylate is patterned by deep x-ray lithography - the entire technology is then called LIGA processing (a German acronym for Lithographie, Galvanoformung, Abformung) [1.31, 1.32]. There exist further techniques like beam induced deposition, sculpturing and welding of microstructures [1.33, 1.34], which are not yet in batch fabrication and are not subject of this study.

In this work, new surface micromachining techniques for single crystal silicon, polycrystalline silicon, and aluminum structures will be presented in view of the realization of a variety of electrostatic microactuators. Structures with identical geometric dimensions have been constructed in the three different technologies. This allows to compare the advantages and disadvantages of a certain material choice directly. Furthermore, a combination of silicon bulk and surface micromachining is discussed which enables the fabrication of complex microsystems such as a scanning system with integrated probe tip.

1.3 Microactuation Principles

Most of the microactuators described in the literature are employing thermal, piezoelectric, or electrostatic driving principles. Thermal powering for MEMS is mainly realized by bimetal (bimorph) actuation or simple thermal expansion. Bimorph actuation is based on the different thermal expansion coefficients of a sandwich structure. Hence, by changing the temperature, the overall stress state of the device can be modified, and by choosing an appropriate design, this results in controlled displacements [1.35-1.37]. The temperature changes are normally induced by current heating. Simple thermal expansion uses a material with a high thermal expansion coefficient; if heated, it may, for example, deform a thin membrane. An interesting aspect of this method is that very thin and flexible optical fibers can be used to power the device from the outside [1.38]. The main advantage of thermal actuation is that large amplitudes of several micrometers and considerable forces can be created at IC-compatible voltages. The disadvantages are that they have a rather high power consumption and the displacement characteristics is influenced by the thermal environment. The bandwidth of operation is maximally in the hundreds of Hertz.

Microactuators like pumps [1.5] or optical scanners [1.39] are often driven by piezostacks. Hence, a hybrid assembly is required, which is ideal for the fabrication of prototype devices but makes the fabrication at a large scale more difficult. Recently, however, piezoelectric actuators based on zinc oxide (ZnO) or lead-zirconate-titanate (PZT) thin films have been presented [1.40]. It has been shown that vibrations of small amplitudes can be employed to construct actuators like a micromotor [1.41, 1.42]. An optical chopper, which has been presented recently, is employing the piezoelectric effect of quartz for the actuation [1.43]. The actuation voltage for piezoelectric actuators is in general rather high, i. e., in the range of 100 - 200 V, and there is a considerable performance dependence on temperature. However, an advantage of piezoelectric actuators is that they can create rather large forces and they can also operate in dusty environments.

Electrostatics is the third widely used actuation principle. Already in the 1970s, electrostatically deflectable membranes [1.44] and deflectable cantilevers for light modulation [1.45] have been constructed. In the late 1980s and early 1990s, rotating motors have been realized by different laboratories [1.46-1.49]. In the same time period and often by the same laboratories, linear actuators suspended by thin beams have been constructed [1.50-1.53]. Recently, also electrostatically driven valves and pumps have been proposed [1.54-1.56]. IC-compatible voltages are easily attained; high frequency and low power actuation is possible, and the electrostatic actuation is relatively independent of the thermal environment. Further, it is not susceptible to hysteresis in the positioning. A disadvantage, however, is that electrostatic microactuators have to be protected from dust and humidity. Because electrostatic actuation has many intriguing features, this work has been focused on the study of electrostatic microactuators.

There are many further actuation principles like electromagnetics [1.57] or shape memory alloys [1.58], which are nowadays mainly in a research state and will not be discussed here.

1.4 Background and Evolution of the Work

In spring 1991, when this work started, the silicon bulk micromachining was a well established technology at the IMT with almost a decade of continued experience [1.59-1.61]. The polysilicon surface micromachining was implemented in the laboratory in the late 1980s [1.62]. First integrated micromechnisms have been constructed such as silicon bolometers for nuclear radiation detection [1.63], resonating beams for transducer applications [1.64, 1.65], and biaxial scanning mirrors [1.37]; further, electrostatic micromotors were in fabrication [1.66]. The CSEM on the other hand had years of experience with the microfabrication of optical microshutters [1.67], capacitive accelerometers [1.68], and capacitive microphones [1.69]. A project supported by the Swiss Foundation for Microtechnology Research (FSRM 90/08) defined a joint development (IMT-CSEM) of integrated micromechanisms in silicon and polysilicon. In particular, the development of the two layer polysilicon process has been a close collaboration - the wafers have been processed partly at the IMT and partly at the CSEM. In a rather early state of the project, the silicon and polysilicon technologies have been already developed successfully so that further reaching goals could be integrated into the work. Thus, an aluminum surface micromachining process has been developed, and an integrated silicon scanning unit has been constructed, which is partly based on the IMT knowledge of tip and cantilever fabrication [1.13]. The development of light modulators is another domain, where the IMT-CSEM collaboration has been close, and for this part of the work, also partners from the private industry showed a distinct interest.

1.5 Outline of the Thesis

The thesis is subdivided into six chapters. This introduction chapter is followed by a chapter that focuses on the design of electrostatic microactuators. In the first part of Chapter 2, the driving forces are estimated; for simple cases, analytical formulae are derived, and for more complex setups, finite element modelling (FEM) is employed to estimate the forces and moments acting on the electrodes. The electrodes have to be guided by mechanical suspensions. Therefore, in a second part, the spring constants, elastic properties and stresses of the suspensions are studied. Again, analytical formulae are derived for simple setups, and FEM is used for optimizing the more complex suspensions.

Chapter 3 discusses the fabrication technology in details. Structures have been fabricated using surface micromachining and employing the three different materials single crystal silicon, polycrystalline silicon, and aluminum. The micromachining of each material required specific processes which are explained. The realization of complex silicon actuators has been possible by an elaborated combination of bulk micromachining and surface micromachining in single crystal silicon.

Chapter 4 describes the working principles, testing, and performance of the following electrostatic actuator devices: the comb actuator, which allows a linear displacement and positioning over a range of 15 μm; the *xy*-nanopositioner, which can be used for precise two-dimensional positioning; and the light modulators, which can be used to alter the phase or amplitude of a laser beam. For all these devices, static displacements in function of the applied voltage have been investigated, and resonance frequencies have been determined.

In the following Chapter 5, mechanical and optical properties of the employed materials are investigated. In particular, internal stresses, sticking, and yield strengths have been determined, and the endurance test stability has been observed. In addition, investigations of optical properties such as reflectivities and surface scattering of the finished devices are presented.

Finally, Chapter 6 gives a summary. Conclusions are drawn, especially in view of further developments of the actuators into microsystems as well as of opportunities for a commercialization of the presented technology and the fabricated devices.

References

[1.1] W. S. N. Trimmer, "Microrobots and micromechanical systems", *Sensors and Actuators*, vol. 19 (1989), pp. 267-287.

[1.2] H. Fujita and K. J. Gabriel, "New opportunities for micro actuators", in *Proc. 4th IEEE Workshop on Micro Electro Mechanical Systems*, Nara, Japan, Jan. 1991, pp. 14-20.

[1.3] E. Bassous, "Nozzles formed in mono-crystalline silicon", *U.S. patent 3 921 916*, 1975.

[1.4] K. E. Petersen, "Fabrication of an integrated, planar silicon ink jet structure", *IEEE Trans. Electron Devices*, vol. ED-26 (1979), p. 1918.

[1.5] J. H. J. Fluitman and T. S. J. Lammerink, "Micro fluid flow controllers", in *UETP-MEMS Course on Microactuators*, Neuchâtel, Switzerland, 1993.

[1.6] B. van der Schoot, S. Jeanneret, A. van der Berg, and N. F. de Rooij, " A silicon integrated miniature chemical analysis system", *Sensors and Actuators*, vol. B-6 (1992), pp. 57-60.

[1.7] G. Fuhr, R. Hagedorn, and T. Müller, "Linear motion of dielectric particles and living cells in microfabricated structures induced by traveling electric fields", in *Proc. 4th IEEE Workshop on Micro Electro Mechanical Systems*, Nara, Japan, Jan. 1991, pp. 259-264.

[1.8] M. Washizu, "Manipulation of biological objects in micromachined structures", in *Proc. 5th IEEE Workshop Micro Electro Mechanical Systems*, Travemünde, Germany, Feb. 1992, pp. 196-201.

[1.9] S. Futami, A. Furutani, and S. Yoshida, "Nanometer positioning and its micro-dynamics", *Nanotechnology*, vol. 1 (1990), pp. 31-37.

[1.10] T. R. Albrecht, S. Akamine, T. E. Carver, and C. F. Quate, "Microfabrication of cantilever styli for the atomic force microscope", *J. Vac. Sci. Technol.*, vol. A8 (1990), p. 3386.

[1.11] O. Wolter, Th. Bayer, and J. Greschner, "Micromachined silicon sensors for scanning force microscopy", *J. Vac. Sci. Technol.*, vol. B9 (1991), pp. 1353-1357.

[1.12] M. M. Farooqui and A. G. R. Evans, "Silicon sensors with integral tips for atomic force microscopy: a novel single mask fabrication process", *J. Micromech. Microeng.*, vol. 3 (1993), pp. 8-12.

[1.13] J. Brugger, R. A. Buser, and N. F. de Rooij, "Silicon cantilevers and tips for scanning force microscopy", *Sensors and Actuators*, vol. A34 (1992), pp. 193-200.

[1.14] S. Akamine, T. R. Albrecht, M. J. Zdeblick, and C. F. Quate, "A planar process for the microfabrication of a scanning tunneling microscope", *Sensors and Actuators*, vol. A21-A23 (1990), pp. 964-970.

[1.15] T. Itoh and T. Suga, "Piezoelectric force sensor for scanning force microscopy", in *Tech. Dig. 7th International Conference on Solid-State Sensors and Actuators*, Yokohama, Japan, June 1993, pp. 610-613.

[1.16] J. J. Yao, S. C. Arney, and N. C. MacDonald, "Fabrication of high frequency two-dimensional nanoactuators for scanned probe devices", *J. Electromech. Syst.*, vol. 1 (1992), pp. 14-22.

[1.17] J. Mohr, M. Kohl, and W. Menz, "Micro optical switching by electrostatic linear actuators with large displacements", in *Tech. Dig. 7th International Conference on Solid-State Sensors and Actuators*, Yokohama, Japan, June 1993, pp. 120-123.

[1.18] R. Jebens, W. Trimmer, and J. Walker, "Microactuators for aligning optical fibers", *Sensors and Actuators*, vol. 20 (1989), pp. 65-73.

[1.19] Y. Kikuya, M. Hirano, K. Koyabu, and F. Ohira, "Micro alignment machine for optical coupling", in *Tech. Dig. IEEE Workshop on Micro Electro Mechanical Systems*, Ft. Lauderdale, FL, USA, Feb. 1993, pp. 36-41.

[1.20] J. H. Herman and D. J. Clift, "Miniature Fabry-Perot interferometers micromachined in silicon for use in optical fiber WDM systems", in *Tech. Dig. 6th International Conference on Solid-State Sensors and Actuators*, San Francisco, CA, USA, June 1991, pp. 372-375.

[1.21] K. Aratani, P. J. French, P. M. Sarro, R. F. Wolffenbuttel, and S. Middlehoek, "Process and design considerations for surface micromachined beams for a tuneable interferometer array in silicon", in *Tech. Dig. IEEE Micro Electro Mechanical Systems Workshop*, Ft. Lauderdale, FL, USA, Feb. 1993, pp. 230-235.

[1.22] L. J. Hornbeck, "Deformable-mirror spatial light modulators", in *Proc. Soc. Photo-Opt. Instrum. Eng.*, vol. 1150 (1989), pp. 86-102.

[1.23] "Tough competition ahead in micromachines", *Electro Optics*, Sept. 1993, p. 15.

[1.24] Nova Sensor, *Silicon Sensors and Microstructures*, USA, June 1990.

[1.25] K. Petersen, "Silicon as a mechanical material", *Proc. IEEE*, vol. 70 (1982), pp. 420-457.

[1.26] S. J. Sherman, W. K. Tsang, T. A. Core, R. S. Payne, D. E. Quinn, K. H.-L. Chau, J. A. Farash, S. K. Baum, "A low cost monolithic accelerometer; product/technology update", *IEDM*, 1992, pp. 501-504.

[1.27] Lj. Ristic, R. Gutteridge, J. Kung, D. Koury, B. Dunn, and H. Zunino, "A capacitive type accelerometer with self-test feature based on a double-pinned polysilicon structure", in *Tech. Dig. 7th International Conference on Solid-State Sensors and Actuators*, Yokohama, Japan, June 1993, pp. 810-813.

[1.28] J. B. Sampsell, "The digital micromirror device and its application to projection displays", in *Tech. Dig. 7th International Conference on Solid-State Sensors and Actuators*, Yokohama, Japan, June 1993, pp. 24-27.

[1.29] L. T. Romankiw, "Thin film inductive heads: from one turn to thirty one turns", in *Proc. Electrochem. Soc. Magnetic Materials, Processes and Devices*, NJ, USA, 1990, pp. 39-53.

[1.30] M. G. Allen, "Polyimide-based processes for the fabrication of thick electroplated microstructures", in *Tech. Dig. 7th International Conference on Solid-State Sensors and Actuators*, Yokohama, Japan, June 1993, pp. 60-65.

[1.31] W. Menz, W. Bacher, M. Harmening, and A. Michel, "The LIGA technique - a novel concept for microstructures and the combination with Si-technologies by injection molding", in *Tech. Dig. IEEE Micro Electro Mechanical Systems Workshop*, Nara, Japan, Jan. 1991, pp. 69-73.

[1.32] H. Guckel, K. J. Skrobis, T. R. Christenson, J. Klein, S. Han, B. Choi, and E. G. Lovell, "Fabrication of assembled micromechanical components via deep x-ray lithography", in *Tech, Dig, IEEE Micro Electro Mechanical Systems Workshop*, Nara, Japan, Jan. 1991, pp. 74-79.

[1.33] M. Boman, H. Westberg, S. Johanson, and J.-A. Schweitz, "Helical microstructures grown by laser assisted chemical vapor deposition", in *Tech. Dig. IEEE Micro Electro Mechanical Systems Workshop*, Travemünde, Germany, Feb. 1992, pp. 162-167.

[1.34] W. H. Brünger and K. T. Kohlmann, "E-beam induced fabrication of microstructures", in *Tech. Dig. IEEE Micro Electro Mechanical Systems Workshop*, Travemünde, Germany, Feb. 1992, pp. 168-170.

[1.35] W. Riethmüller and W. Benecke, "Thermally excited silicon microactuators", *IEEE Trans. Electron Devices*, vol. 35 (1988), pp. 758-763.

[1.36] D. Moser, O. Brand, and H. Baltes, "A CMOS compatible thermally excited silicon oxide beam resonator with aluminum mirror", in *Tech. Dig. 6th International Conference on Solid-State Sensors and Actuators*, San Francisco, CA, USA, June 1991, pp. 547-550.

[1.37] R. A. Buser, N. F. de Rooij, H. Tischhauser, A. Domman, and G. Staufert, "Biaxial scanning mirror activated by bimorph structures for medical applications", *Sensors and Actuators*, vol. A31 (1992), pp. 28-34.

[1.38] H. Mizoguchi, M. Ando, T. Mizuno, T. Takagi, and N. Nakajima, "Design and fabrication of light driven micropump", in *Tech. Dig. IEEE Micro Electro Mechanical Systems Workshop*, Travemünde, Germany, Feb. 1992, pp. 31-36.

[1.39] H. Goto, H. Kamoda, M. Yoneda, and K. Imanaka, "Miniature two-dimensional optical scanner utilizing a multilayered piezoelectric actuator with new displacement expansion mechanism", in *Tech. Dig. VDI/VDE 3rd International Conference on New Actuators*, Bremen, Germany, June 1992, pp. 68-70.

[1.40] W. Tjehn, T. Tamagawa, C. P. Ye, C. C. Hsueh, P. Shiller, and D. L. Polla, "Properties of piezoelectric thin films for micromechanical devices and systems", in

Tech. Dig. IEEE Micro Electro Mechanical Systems Workshop, Nara, Japan, Jan. 1991, pp. 114-119.

[1.41] A. M. Flynn, L. S. Tavrow, S. F. Bart, R. A. Brooks, D. J. Ehrlich, K. R. Udayakumar, and L. E. Cross, "Piezoelectric micromotors for microrobots", *J. Microelectromech. Syst.*, vol. 1 (1992), pp. 44-51.

[1.42] G.-A. Racine, R. Luthier, and N. F. de Rooij, "Hybrid ultrasonic micromachined motors", in *Tech. Dig. IEEE Micro Electro Mechanical Systems Workshop.*, Ft. Lauderdale, FL, USA, Feb. 1993, pp. 128-132

[1.43] H. Toshiyoshi, H. Fujita, T. Kawai, and T. Ueda, "Piezoelectrically operated actuators by quartz micromachining for optical applications", in *Tech. Dig. IEEE Micro Electro Mechanical Systems Workshop*, Ft. Lauderdale, FL, USA, Feb. 1993, pp. 133-138.

[1.44] J. A. van Raalte, "A new Schlieren light valve for television projection", *Appl. Opt.*, vol. 9 (1970), pp. 2225-2230.

[1.45] K. E. Petersen, "Micromechanical light modulator array fabricated on silicon", *Appl. Phys. Lett.*, vol. 31, no. 8 (1977), pp. 521-523.

[1.46] L. S. Fan, Y. C. Tai and R. S. Muller, "IC-processed micro-motors: design, technology and testing" in *Tech. Dig. IEEE Micro Electro Mechanical Systems Workshop*, Salt Lake City, UT, USA, Feb. 1989, pp. 1-6.

[1.47] M. Mehregany, P. Nagarkar, S. D. Senturia, and J. H. Lang, "Operation of microfabricated harmonic and ordinary side-drive motors", in *Tech. Dig. IEEE Micro Electro Mechanical Systems Workshop*, Napa Valley, CA, USA, Feb. 1990, pp. 1-8.

[1.48] U. Wallrabe, P. Bley, B. Krevet, W. Menz, and J. Mohr, "Theoretical and experimental results of an electrostatic micro motor with large gear ratio fabricated by the LIGA process", in *Proc. IEEE Micro Electro Mechanical Systems Workshop*, Travemünde, Germany, Feb. 1992, pp. 139-140.

[1.49] L. Paratte and N. F. de Rooij, "Electrodeposited electrostatic wobble motors on silicon for wristwatch applications", in *Abstracts of Late News 7th International Conference on Solid-State Sensors and Actuators*, Yokohama, Japan, June 1993, pp. 4-5.

[1.50] W. C. Tang, T. H. Nguyen, and R. T. Howe, "Laterally driven polysilicon resonant microstructures", *Sensors and Actuators*, vol. A20 (1989), pp 25-32.

[1.51] C. J. Kim, A. P. Pisano, and R. S. Muller, "Silicon-processed overhanging microgripper", in *J. Microelectromech. Syst.*, vol. 1, no. 1 (1992), pp. 31-36.

[1.52] N. Takeshima, K. J. Gabriel, M. Ozaki, J. Takahashi, H. Horiguchi, and H. Fujita, "Electrostatic parallelogram actuators", in *Tech. Dig. 6th International Conference on Solid-State Sensors and Actuators*, San Francisco, CA, USA, June 1991, pp. 63-66.

[1.53] J. Mohr, P. Bley, M. Strohrmann, U. Wallrabe, "Microactuators fabricated by the LIGA process", *J. Micromech. Microeng.*, vol. 2 (1992), pp. 234-241.

[1.54] T. Ohnstein, T. Fukiura, J. Ridley, and U. Bonne, "Micromachined silicon microvalve", in *Tech. Dig. IEEE Micro Electro Mech. Syst. Workshop*, Napa Valley, CA, USA, Feb. 1990, pp. 95-98.

[1.55] M. Shikida. K. Sato, S. Tanaka, Y. Kawamura, and Y. Fujisaki, "Electrostatically-actuated gas valve with large conductance", in *Proc. 7th International Conference on Solid-State Sensors and Actuators*, Yokohama, Japan, June 1993, pp. 94-97.

[1.56] K. J. Gabriel, O. Tabata, K. Shimaoka, S. Sugiyama, and H. Fujita, "Surface-normal electrostatic/pneumatic actuator", in *Tech. Dig. IEEE Micro Electro Mechanical Systems Workshop*, Ft. Lauderdale, FL, USA, Feb. 1993, pp. 128-131.

[1.57] H. Guckel, T. Christenson, and K. Skrobis, "Metal micromechanisms via deep x-ray lithography, electroplating and assembly", *J. Micromech. Microeng.*, vol. 2 (1992), pp. 225-228.

[1.58] J. A. Walker, K. J. Gabriel, and M. Mehregany, "Thin-film processing of TiNi shape memory alloy", *Sensors and Actuators*, vol. A21-A23 (1990), pp. 243-246.

[1.59] R. A. Buser, "Theoretical and experimental investigations on silicon single crystal resonant structures", *Ph. D. Dissertation*, Institute of Microtechnology, University of Neuchâtel, Switzerland, 1989.

[1.60] B. Kloeck, "Design, fabrication and characterization of piezoresistive pressure sensors, including the study of electrochemical etch-stop", *Ph. D. Dissertation*, Institute of Microtechnology, University of Neuchâtel, Switzerland, 1989.

[1.61] T. Tschan, "Simulation, design and characterization of a piezoresistive accelerometer, fabricated by a bipolar-compatible industrial process", *Ph. D. Dissertation*, Institute of Microtechnology, University of Neuchâtel, Switzerland, 1992.

[1.62] C. Linder, "Electromechanical polysilicon structures and micromachining processes for sensor and actuator applications", *Ph. D. Dissertation*, Institute of Microtechnology, University of Neuchâtel, Switzerland, 1993.

[1.63] G.-A. Racine, R. A. Buser, N. F. de Rooij, G. Stucki, R. Stucki, and K. Pretzl, "Low-temperature operating silicon bolometers for nuclear radiation detection", *Sensors and Actuators*, vol. A21-A23 (1990), pp. 478-481.

[1.64] C. Linder and N. F. de Rooij, "Investigations on free-standing polysilicon beams in view of their application as transducers", *Sensors and Actuators*, vol. A21-23 (1990), pp. 1053-1059.

[1.65] C. Linder, E. Zimmermann, and N. F. de Rooij, "Capacitive polysilicon resonator with MOS detection circuit", *Sensors and Actuators*, vol. A25-27 (1991), pp. 591-595.

[1.66] L. Paratte, G.-A. Racine, N. F. de Rooij, E. Bornand, "Design of an integrated electrostatic stepper motor with axial field", *Sensors and Actuators*, vol. A25-27 (1991), pp. 597-603.

[1.67] M. A. Cadman, A. Perret, F. Porret, R. Vuilleumier, and P. Weiss, "New micromechanical display using metallic films", *IEEE Electron. Dev. Lett.*, vol. 4, no. 1 (1983).

[1.68] F. Rudolf, A. Jornod, J. Bergqvist, and H. Leuthold, "Precision accelerometers with µg resolution", *Sensors and Actuators*, vol. A21 (1990), pp. 297-302.

[1.69] J. Bergqvist and F. Rudolf, "A new condenser microphone in silicon", *Sensors and Actuators*, vol. A21 (1989), pp. 123-125.

Chapter Two

Design Considerations

Electrostatic actuators have a long history. Already in the 1750s, *Gordon* built an electric bell [2.1], and *Franklin* constructed a spark motor named the electric wheel [2.2]. Since then, a myriad of different electrostatic actuators have been proposed and fabricated. But despite their distinguished history, electrostatic actuators have found few practical applications because of the high voltages and the mechanical accuracies required. Micromechanics, however, has changed prospects for electrostatic actuators. There are mainly three reasons which favor electrostatic drive in the sub-millimeter dimensions. First, thin insulation layer withstand high electric fields; breakdown strengths as high as 10 MV/cm are easily obtained in SiO_2 thin films [2.3]. Further, the breakdown strength of air is greatly increased for small gaps as described by the Paschen's law [2.4]; *Tavrow* has reported on micromechanical structures a breakdown strength for a 1.65 μm gap of 4 MV/cm [2.5]. The second reason is that the electrostatic force is a surface force and obeys a favorable scaling law for small dimensions [2.6]. Third, the required precision of the mechanical assembly is easily achieved by the lithography based micromachining. A general advantage of electrostatic actuators is that they are essentially driven by voltage. Voltage switching is fast and energy losses associated with Joule heating are small [2.7]; further, no energy has to be supplied to keep the actuator in any stable position. As follows from the electrostatic considerations, mechanical structures are required to keep the movable actuator elements in place and to guide them on a defined track. Since friction scales for micromechanical applications unfavorably [e.g., 2.8], it has to be avoided whenever possible. Therefore, we investigated only bending and twisting suspensions.

For constructing electromechanical microactuators, it is crucial to have a good knowledge of the electrostatic part, which is mainly concerned with creating the required forces, as well as of the mechanical part, which includes the design of suspensions, indispensable for the controlled actuation and displacement. The analytical calculation of electrostatic forces will be discussed in Chapter 2.1. For complex electrode setups, finite element modelling (FEM) is useful to estimate the electrostatic forces. For various actuator types, the expected force has been numerically determined. The electrostatic levitation phenomenon is investigated with the help of FEM. Chapter 2.2 discusses the mechanical suspension of laterally movable actuators. For comb actuator suspensions, the spring constants in different directions are calculated. The suspension of vertically movable actuators is treated in Chapter 2.3. For all actuators, the electromechanical performance has been estimated using typical geometric dimensions. Since the polysilicon technology is the furthest developed surface micromachining technique reported in this work, material properties of polysilicon are employed as input parameters for all computations and simulations.

2.1 Electrostatic Forces

Electrostatic forces created in microactuators are not well explored today, and there are many possibilities open for optimization and new designs. Therefore, during this project, special attention has been focused on a better understanding of electrostatics for micromechanics. By employing the theory of Section 2.1.1 (parallel plate capacitor), the following two electrostatic forces can be calculated analytically: the force vertical to the two plates and the alignment force parallel to the misaligned plates. In Section 2.1.2, this theory is applied to calculate the forces created in an electrostatic comb actuator. For more accurate estimations, two- and three-dimensional FEM, as explained in Section 2.1.3, is required. FEM also allows a better understanding of the levitation phenomenon, which is described in Section 2.1.4.

2.1.1 Basic theory of electrostatics

The Coulomb's law is describing the force between two charged bodies which are not moving relative to each other. Then, the force between two point charges in a homogeneous medium of infinite extent is proportional to the product of the magnitudes of the charges divided by the square of the distance between them. For practical calculation of forces, it is often useful to describe the electrostatic interaction by employing the concept of the electric field E, where the force F can be expressed as

$$F = Eq \tag{2.1}$$

where q is the electric charge. For the vector field $E(r)$, the two basic equations of electrostatics can be written as

$$\varepsilon_{el} \nabla \cdot E = \rho_{el} \tag{2.2}$$

$$\mathrm{rot} E = 0 \tag{2.3}$$

Equation 2.2 is the Gauss's law, where ε_{el} is the electric permittivity and ρ_{el} is the electric charge density. Since for metallic bodies the charges are accumulated on the surface, Equation 2.2 can be rewritten by using the surface charge density σ_{el} instead of the charge density ρ_{el}

$$\varepsilon_{el} E = \sigma_{el} \tag{2.4}$$

Equation 2.3 allows to introduce the electric potential Φ, a scalar quantity

$$E = -\nabla \Phi \tag{2.5}$$

Further, it is useful to define the capacitance C. If two charges $\pm q$ are brought on two isolated electrodes a potential is created which can be expressed as

$$\Phi = \frac{q}{C} \tag{2.6}$$

With these expressions and basic laws it will be possible to calculate and to estimate the electrostatic forces created in the microactuators.

2.1.2 Analytical calculations for comb actuators

The subsequent considerations of electrostatic forces created in a comb actuator electrode follow in the beginning the reasoning of a paper from *Trimmer and Gabriel* [2.6]. Two conducting rectangular parallel plates separated by an insulating layer create a capacitor with a capacitance given by

$$C = \varepsilon_r \varepsilon_0 w \frac{b}{g} \tag{2.7}$$

where w is the width of the plates, b is the length of the plates, g is the gap between the two plates, and ε_0 and ε_r are the free space and relative permittivities, respectively. Because we are only considering devices which have an air gap between the electrodes, we will assume ε_r to be equal to 1, and we will omit the relative permittivity in the following calculations. If a voltage is applied across the two plates, the potential energy of this capacitor is

$$U = -\frac{1}{2} C V^2 = -\frac{\varepsilon_0 w b V^2}{2g} \tag{2.8}$$

The force in any of the three directions (w, b, g) is given by the negative partial derivative of the potential energy in each direction. To calculate the force in w-direction, consider the plates offset so that they overlap by l as shown in Figure 2.1. In terms of the overlap by l, the potential energy of the capacitor is now

$$U = -\frac{\varepsilon_0 b l V^2}{2g} \tag{2.9}$$

and taking the derivative with respect to l gives the force

$$F_w = -\frac{\partial U}{\partial l} = \frac{1}{2} \frac{\varepsilon_0 b V^2}{g} \tag{2.10}$$

The forces in b- and g-direction are similarly

$$F_b = -\frac{\partial U}{\partial b} = \frac{1}{2} \frac{\varepsilon_0 w V^2}{g} \tag{2.11}$$

and

$$F_g = -\frac{\partial U}{\partial g} = -\frac{1}{2} \frac{\varepsilon_0 w b V^2}{g^2} \tag{2.12}$$

While the tangential forces F_w and F_b are independent of the displacement in the respective direction, the vertical force F_g is strongly dependent on the displacement. As will be seen in the following, in function of the application, either tangential or vertical forces are chosen.

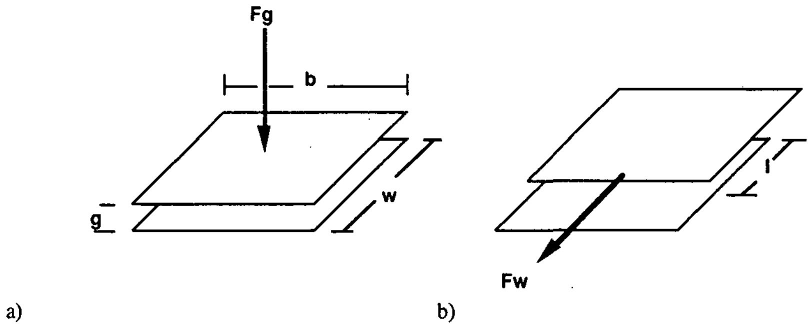

Fig 2.1 Forces created in a parallel plate capacitor: **a)** F_g, the force perpendicular to capacitor plates; **b)** F_w, the force parallel to capacitor plates.

Equation 2.10 can be used to calculate the force created in a comb actuator. A detail of one movable finger between two stator fingers is shown in Figure 2.2. The thickness *t* of the finger corresponds to the length *b* of the plates. For a comb drive with *n* fingers, the force can be expressed as

$$F = \frac{\varepsilon_0 n t V^2}{g} \tag{2.13}$$

With the given limitations of the technology, one can fabricate comb actuators

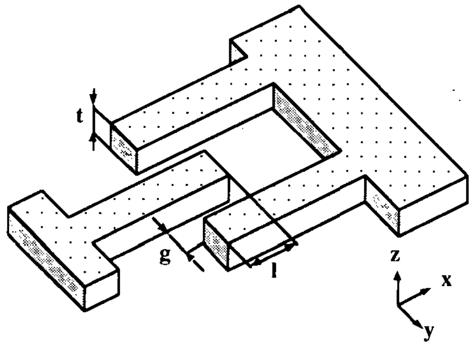

Fig 2.2 Schematic drawing of one movable finger of a comb actuator between two stator fingers.

with a gap between the fingers of 3.2 µm and a thickness of the fingers of 2 µm. With these values, we can calculate the created force of one finger per voltage squared - it is 5.53 pN/V^2. Hence, for a typical comb drive with ten fingers, the total force amounts to 55.3 pN/V^2. As will be seen in Chapter 2.2, the suspension of the comb actuators have to be made very flexible in order to achieve reasonable displacements at low voltages (≤ 15 V), where the created forces in the comb electrodes are generally less than 20 nN.

2.1.3 Finite element modeling of electrostatic forces

In analyzing a complex structure, it is a common procedure to decompose it into an ensemble of discrete, structurally known entities. By doing this in a systematic and clearly defined manner, an overall solution for the assembly of substructures can be found. In 1941, *Hrenikoff* introduced a so-called "framework" method in which elastic problems could be numerically solved. This and other pioneering works in the 1940s formulated a technique which was later known as finite element modeling (FEM). FEM is nowadays a computer based powerful tool for science and engineering. It is widely used, for example, in aerospace industry or in civil and mechanical engineering. For microelectromechanical systems (MEMS) it has been used for simulating the electrostatic field [2.9, 2.10] as well as the behavior of mechanical components [2.11-2.14]. The simulations presented in this work have been performed using the university version of the commercially available finite element program ANSYS® from Swanson Analysis Systems Inc. The only restriction of this version is its limitation to a wavefront of 500. The number of equations which are active after any element has been processed during the solution procedure is called the wavefront at a given point. The program is run on a Hewlett Packard Series 400 work station.

ANSYS® has procedures and elements to treat thermal analyses. The differential equation that governs the phenomenon of heat conduction is the following

$$\nabla \cdot (K \nabla T) = -\rho_Q \tag{2.14}$$

where K is the thermal conductivity, T is the (unknown) temperature, and ρ_Q is the heat generation rate. The Poisson's equation of electrostatics (cf. Equations 2.2 and 2.5) is mathematically of the same form

$$\nabla \cdot (\varepsilon_{el} \nabla \Phi) = - \rho_{el} \tag{2.15}$$

Hence, by analogy, this program can be used to solve problems of electrostatics. A typical simulation showing the equipotential lines of a movable finger between two stator fingers - the identical setup as used for the analytical calculation - is given in Figure 2.3.

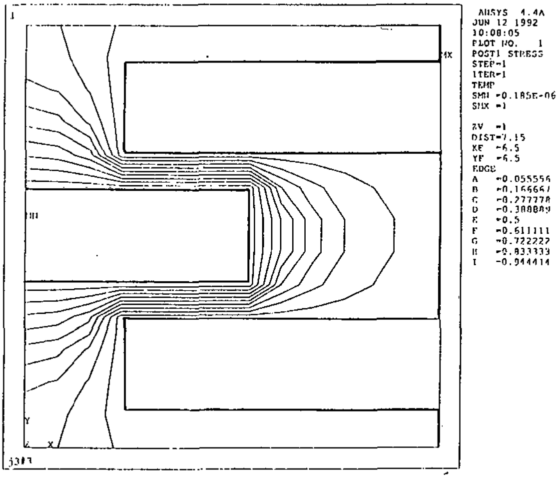

Fig 2.3 Finite element modeling of potential distribution between a movable finger and two stator fingers (ANSYS).

From the potential distribution, the forces acting on the elements can be readily calculated as follows. Based on Equation 2.1, the driving force F can be determined by

$$F = \oint_S E \sigma_{el} \mathrm{d}S \tag{2.16}$$

where the integration is performed over the entire surface S of the movable electrode. σ_{el} and E can be expressed in function of the potential distribution using Equations 2.4 and 2.5, respectively. Hence, the resulting force can be written as

$$F = \varepsilon_0 \oint_S (-\nabla \Phi)|\nabla \Phi| \, \mathrm{d}S \tag{2.17}$$

The integration over the surface S of the electrodes can be done using predefined routines of the ANSYS® program. For preliminary estimations, it can be deduced that strong forces are, where large gradients in the potential distribution occur. As can be seen in Figure 2.3, there are strong forces in y-direction, which are, however, compensated as long as the movable finger is exactly in the middle of the two stator fingers. On the other hand, there are forces in x-direction, which are not compensated and which cause the linear displacement. As will be seen further down, FEM is not only useful to visualize forces, but it allows above all to estimate forces numerically for complex electrode assemblies, where analytical calculations would get complicated or impossible.

For the setup of the movable finger suspended between two stator fingers, we can state that for a small displacement Δy in y-direction, the forces are no longer compensated, and a net driving force F_y is created, which can be expressed as follows

$$F_y = \frac{\varepsilon_0 n t l V^2}{2} \left(\frac{1}{(g - \Delta y)^2} - \frac{1}{(g + \Delta y)^2} \right) \tag{2.18}$$

As shown by *Hirano et al.* [2.15], this force has to be compensated by the rigidity of the mechanical suspension. Therefore, special spring elements have to be employed. We will reconsider this problem when discussing the suspension of comb actuators in Chapter 2.2.

Another effect has been neglected when we were considering Equation 2.13. The force F_p generated by a parallel plate capacitor, which consists of the capacitor plate formed by the front end of the movable fingers, and of the parallel part of the fixed electrode in front of it. Since the capacitor gap is large compared with the capacitor area, the approach allows for a rough estimation only

$$F_p = \frac{\varepsilon_0 n t w V^2}{(d - \Delta x)^2} \tag{2.19}$$

In addition to the variables of the earlier equations, there is the width w of the fingers, d, the initial distance of the front ends of the fingers if no actuation occurs, and Δx, the displacement in x-direction. The increase in the driving force due to this additional capacitor is shown in Figure 2.4. The force numerically calculated using the analytical Equation 2.19 and the force calculated using FEM, based on the structure shown in Figure 2.3, are given in the diagram. For this setup, analytical calculations and FEM are in good agreement.

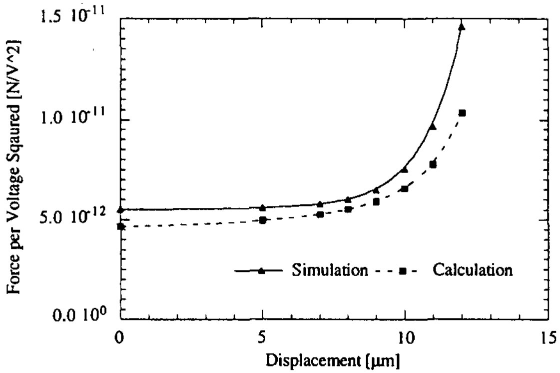

Fig 2.4 Electrostatic force on one movable finger. The lateral force increases as function of the displacement due to the parallel plate capacitors formed by the front end of the comb drive fingers. Finite element modeling and analytical calculations deliver similar results.

2.1.4 Electrostatic levitation

Electrostatic comb drive levitation has been described first by *Tang et al.* [2.16]. In order to avoid sticking of the movable structures on the substrate, successfully operating electrostatic actuators require a ground plane under the structure to shield it from vertical fields [2.17]. The ground plane, however, contributes to an unbalanced potential distribution (cf. Figures 2.5 and 2.6), which causes the levitation. FEM is again a powerful tool for investigating this electrostatic phenomenon. Figure 2.7 shows the simulated force per voltage squared in function of the applied voltage. The dimensions for the simulated setup are 6 µm wide and 2 µm thick fingers with a gap of 2 µm between them; the stator fingers are suspended 2 µm above the ground plane. These initial dimensions have been chosen because of restrictions in the fabrication technology on the one hand and on the other hand, because of theoretical considerations predicting a maximum capacity for a comb electrode system having a finger width to gap ratio of three [2.18]. The maximum levitating force is observed when the movable finger is in plane with the stator fingers - it is 10.6 pN/V^2 for one movable finger. Hence, the levitation force is about twice the lateral driving force we calculated earlier. As the levitation height increases, the force gets lower until it reaches a zero value for a levitation of 1.2 µm. At higher levitations the force will be negative - it will pull back the movable finger to the equilibrium position. Thus, the electrostatic levitation causes the movable electrodes to be displaced at higher actuation voltages at a level of 1.2 µm above the fixed electrodes. In summary, there are two main problems resulting from this effect. First, the z-position of the movable actuator element varies during operation and second, the net driving force will be reduced thereby. Therefore, a good understanding of this effect is necessary for constructing electrostatic microactuators. It is also conceivable that, based on the electrostatic levitation, new types of electrostatic actuators may be realized. Thus, employing electrostatic forces, an electric levitation bearing for micromotors has been proposed by *Kumar et al.* [2.19]; it is an open loop stable system using the tuning of the frequency to determine the position of the levitated structure.

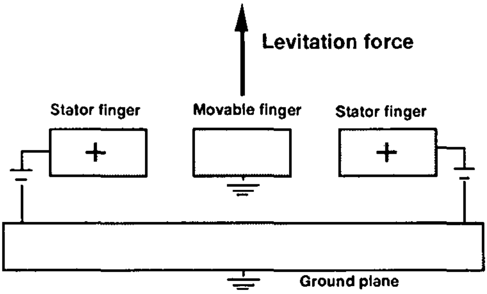

Fig. 2.5 Schematic cross section of the driving part of a comb actuator. While the ground plate and the movable finger are on ground potential, a voltage is applied on the stator fingers. The mirror charges induced on the ground plate and the movable finger are causing the levitation force.

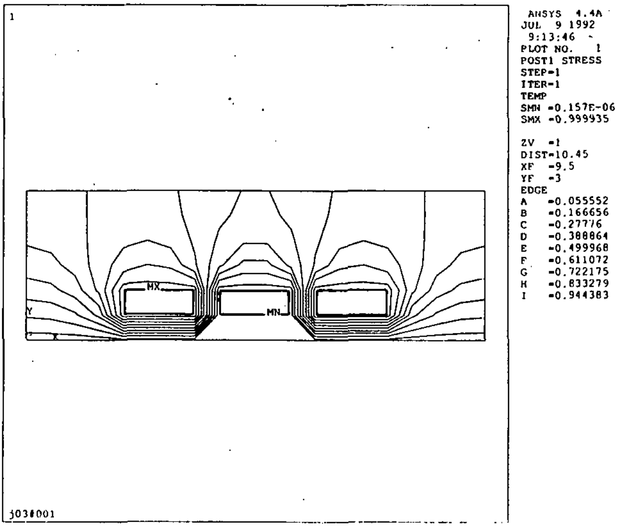

Fig. 2.6 Finite element modeling of the potential distribution around one movable finger and two stator fingers. The fingers are 2 µm thick and 6 µm wide, and the gap between them is 2 µm; the stator fingers are suspended 2 µm above the ground plane.

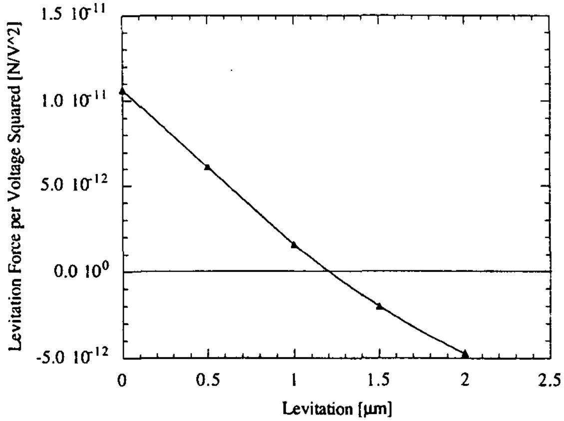

Fig. 2.7 Simulated levitation force per voltage squared for one movable finger.

2.1.5 Electrostatic torque of torsional mirrors

For investigations of torsional mirrors, the electrostatic torque is calculated. Figure 2.8 shows a schematic view of a torsional micromirror. The deflection model discussed here is based on the following assumptions:

i) Fringing fields are ignored.

ii) A mirror element is electrostatically attracted only by the surface charges from the addressing electrode.

This is, of course, a much simplified view of the actual situation. In reality, other parts of the mirror which are not directly in front of the address electrode as well as adjacent mirror elements and landing electrodes will contribute to and modify the total electric field. The total electric torque T_e on the mirror element is calculated by integrating the incremental torque of the segment which is directly in front of the address electrode

$$T_e = \int_0^b \mathrm{F}(x)x\,dx \tag{2.20}$$

where b is the length of the address electrode. For rotations of an angle θ (radians), the electrode gap can be expressed as $d(x) = d - \theta x$, where d is the initial gap between mirror and address electrode (see Figure 2.8). Based on Equation 2.20, an expression for the electric torque T_e can be found

$$T_e = \frac{1}{2}\varepsilon_0 V^2 w \int_0^b \frac{x\,dx}{(d - \theta x)^2} = \frac{\varepsilon_0 V^2 w}{2\theta^2}\left(\ln\left(1 - \frac{\theta b}{d}\right) + \frac{\theta b/d}{1 - \theta b/d}\right) \tag{2.21}$$

where w is the width of the electrode. For small rotations, Equation 2.21 can be approximated by

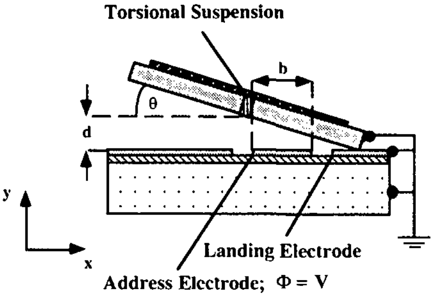

Fig. 2.8 Schematic drawing of a tilted torsional micromirror.

$$T_e = \frac{\varepsilon_0 V^2 w b^2}{4d^2} \tag{2.22}$$

Hence, the electrostatic torque is proportional to the square of the electrode length b, to the electrode width w, and inversely proportional to the square of the electrode separation d. For numerical calculations, a torsional mirror with an address electrode of 22 µm by 30 µm is assumed, while the electrode gap d is 2 µm. Thus, the electric torque per voltage squared is 8.04 fNm/V^2.

2.2 Suspensions for Laterally Movable Actuators

For lateral displacements, the basic structure is the folded beam suspension, which has been introduced for comb actuators by *Tang et al.* [2.20]; it allows a guided displacement and its restoring force is linear for rather large displacement amplitudes. Its mechanical design properties have been discussed, based on an analytical approach, by *Pisano and Cho* [2.21]. Section 2.2.1 recalls some results of the basic theory of elasticity, and Section 2.2.2 describes the performance of the comb actuator suspension. Using FEM, suspensions have been optimized, and in particular, the ratio of the spring constant in stroke direction to the spring constant in the perpendicular direction has been increased as will be discussed in Section 2.2.3. For optical microshutters the surface occupied by the folded beam suspension has been minimized by using a new type of suspension, called the meander shaped folded beam suspension; the characteristics of this new suspension will be explained in Section 2.2.4. Finally, in Section 2.2.5 the suspension for an *xy*-nanopositioner will be discussed. For all these different structures, formulae for the spring constant, resonance frequency, and maximum strain are derived. In order to give a 'feeling' for the real devices, numerical calculations have been performed with geometric dimensions and material properties of the fabricated devices.

2.2.1 Basic theory of elasticity

Many characteristics of the suspensions can be calculated by employing analytical expressions from simple theory of elasticity. Therefore, some of the basic results will be recalled before considering the different types of suspensions.

The relation between stress σ and strain ε is given by the Hooke's law

$$\sigma = E\varepsilon \tag{2.23}$$

where E is the Young's modulus. Hence, the deformation of a straight beam under axial loads can be directly calculated. In this section, we follow the reasoning proposed by *Timoshenko* [2.22]. For a beam under transverse load, the strain in x-direction can be expressed using Figure 2.9.

$$\varepsilon_x = \frac{SS'-NN'}{NN'} = \frac{(r+z)\phi - r\phi}{r\phi} = \frac{z}{r} \tag{2.24}$$

Based on Figure 2.10, a relation between the radius of curvature r and the torque T_m can be established. Let dA denote an elemental area of the cross section at distance z from the neutral axis. The force acting on this element is the product of the stress σ and the area dA. The moment acting on the element with respect to the neutral axis is $(Ez/r)z\mathrm{d}A$. Adding all these moments over the cross section results in the moment T_m.

$$\int_A \frac{E}{r} z^2 \mathrm{d}A = \frac{EI_y}{r} = T_m \tag{2.25}$$

$I_y = \int z^2 \mathrm{d}A$ is the moment of inertia of the cross section with respect to the neutral axis y. For small deflections the curvature radius can be approximated by the derivative of the second order of a function $z(x)$ describing the shape of the bent beam.

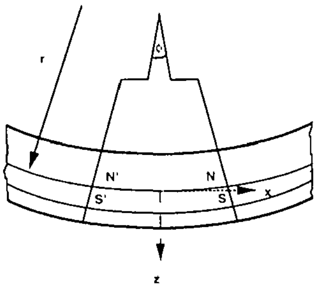

Fig. 2.9 Bent beam; after [2.22]

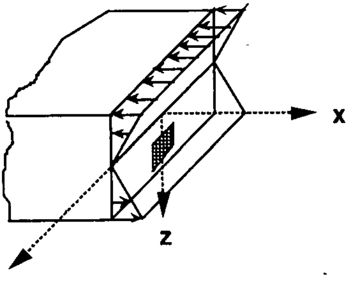

Fig. 2.10 Stress distribution on a cross section of the beam; after [2.22]

$$\frac{1}{r} = -\frac{d^2z}{dx^2} \tag{2.26}$$

Thus, Equation 2.25 can be rewritten as

$$EI_y\frac{d^2z}{dx^2} = -T_m \tag{2.27}$$

2.2.2 Analytical considerations for comb actuator suspensions

One major requirement for comb actuator suspensions is that they have to guide the displacement of the movable comb electrode. This can be achieved with a spring that has a low spring constant in the stroke direction; however, in the transverse direction it has to be high because of the strong forces created for the slightest misalignment of the movable fingers between the stator fingers (cf. Section 2.1.3). Furthermore, its spring constant should not depend, even for rather large amplitudes, on the displacement. The folded beam suspension, introduced for lateral comb actuators by *Tang et al* [2.16], fulfills these requirements. A schematic drawing of a typical suspension for a comb actuator is shown in Figure 2.11. The structure is fixed to the underlying substrate on the four points A, B, C, and D; the rest of the beam structure is freely suspended. As shown in the drawing, the vertical beams are thinner than the horizontal beams. The reason is that they deliver the high flexibility in x-direction, while the horizontal beams are contributing to the stiffness in y-direction. Using simple beam theory [e.g., 2.23], a general expression allows to determine the spring constant for different boundary conditions

$$k = \frac{mEI}{L^3} \tag{2.28}$$

where m is a constant depending on the boundary conditions, E is the Young's modulus, assumed to be 170 GPa for polysilicon and I is the moment of inertia. The standard comb actuator suspension is an assembly of beams which are fixed on one end and guided on the other end. For this boundary conditions, m is equal 12. For horizontal deflection of beams with rectangular cross section, the moment of inertia is $I = tw^3/12$, where t is the thickness of the beam and w is the width of the beam. Thus, the spring constant in x-direction can be written as

$$k_x = \frac{4Etw^3}{L_1^3 + L_2^3} \tag{2.29}$$

where L_1 and L_2 are the lengths of the vertical beams as indicated in Figure 2.11. Hence, the spring constant is proportional to the beam thickness and to the cube of the beam width, and it is inversely proportional to the cube of the beam lengths. Typical dimensions, called standard dimensions in the following, of the suspensions are: 2 µm beam thickness t, 0.4 µm beam width w, 180 µm for the length L_1, and 200 µm for the length L_2. With these dimensions, the calculated spring constant is 6.29 mN/m. When interpreting the actual displacement results in Chapter 4.1, we will see that these simple formulae are very useful and quite accurate for predicting the behavior of the actuators. For roughly estimating the electromechanical performance, we can employ the force per voltage squared of 55.3 pN/V^2 calculated in Section 2.1.2; a displacement per voltage squared of 8.79 nm/V^2 can be computed.

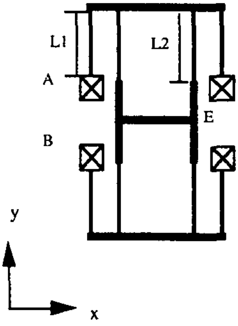

Fig. 2.11 Schematic drawing of the folded beam suspension for a comb actuator. The structure is fixed to the substrate at the points A, B, C, and D. The rest of the beam structure is freely suspended

While it is the intention to use our devices as actuators and not as resonating sensors, it is still useful, especially for high frequency applications, to know the resonance frequencies. For determining an analytical expression of the first natural frequency, the Rayleigh's method [2.24] is employed. The formula is [2.16]

$$f_l = \frac{1}{2\pi}\sqrt{\frac{k_x}{M_c + 0.3714M_b}} \tag{2.30}$$

where M_c and M_b are the masses of the central piece and the supporting beams, respectively. The spring constant k_x has been already calculated in Equation 2.29. Hence, Equation 2.30 can be rewritten as

$$f_l = \frac{1}{\pi}\sqrt{\frac{Etw^3}{(L_1{}^3 + L_2{}^3)(M_c + 0.3714M_b)}} \tag{2.31}$$

For the comb actuator with standard dimensions, the first resonance frequency amounts to 2.63 kHz.

The standard comb actuators are designed for maximum displacements of about 10 µm. This allows to compute the maximum fiber stress based on the maximum torque $T_{m_{max}}$ as calculated by simple beam theory [2.23]. If just one beam of the folded beam suspension is considered, the end restraints of this beam are: fixed on one side and guided on the other side. For these conditions, the maximum bending moment is $T_{m_{max}} = FL/2$, where F is the applied load (for the folded beam suspension 1/8 of the total load). For simplicity, all the beams are assumed to have the same length L. The maximum fiber stress can be expressed as [2.23]

$$\sigma_{max} = \frac{T_{mmax}}{I/c} = \frac{3FL}{w^2t} \tag{2.32}$$

where c is the maximum distance from the neutral axis, which is $w/2$ for our case. Hence, the maximum fiber stress is proportional to the applied load F and to the length L, and it is inversely proportional to the square of the beam width w and to the beam thickness t. The calculated value of σ_{max} is 14.7 MPa; this is around 0.4 % of the fracture stress of 3.57 GPa, which can be determined using the experimental yield strain values of polysilicon from Section 5.1.3. Hence, the elastic limits of the material are not attained.

2.2.3 Finite element modeling of comb actuator suspensions

The present comb actuators have their limitation in actuation range because the drive and the actuation comb tend to touch each other - side sticking. In order to increase this actuation range, the stiffness in the non-actuation direction has to be increased. In the following, the simulated rigidity of different folded beam suspensions will be compared.

The results of different suspensions will be presented here. A typical structure is shown in Figure 2.11. For the simulations, all the forces and moments are applied on the point E. The four presented designs have all similar geometric dimensions; for one design, they are shown in Figure 2.12.

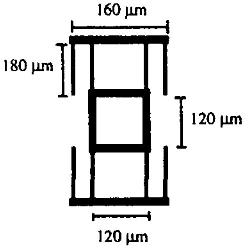

Fig. 2.12 Typical dimensions used for the finite element modeling.

As already discussed earlier, two different beam widths are used. For the simulation, the thinner beams have a width of 2 µm; the width of the thicker beams has been varied - it is either 6 µm or 10 µm. Four different types of folded beam suspensions are used. They are presented in Figure 2.13.

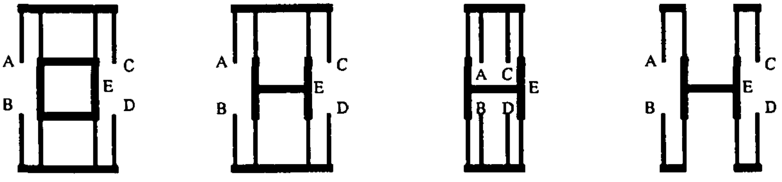

Type 1 Type 2 Type 3 Type 4

Fig. 2.13 Four different folded beam spring elements that were used for a comparison of suspension properties by finite element modeling.

The structure Type 3 is known because of the numerous experiments done by *Tang et al.* [2.16]; structure Type 1 has been used by *Hirano et al.* [2.15]. The other two suspensions are less characterized, and they are shown for comparison.

For the simulation, three-dimensional, uniaxial beam elements have been used to build up a model of the folded beam suspension. The elements have six degrees of freedom, namely, elongations in three directions and rotations in three directions - they have tension, compression, bending, and twisting capabilities (STIF 4 element). As for the analytical calculations, a Young's modulus of 170 GPa has been assumed. The program can account for nonlinearities of the restoring force due to large deflections. The forces and moments are applied on point *E*.

The results of the different simulations are shown in Table 2.1. The spring constants in *x*- and in *y*-direction are listed. While the structure should be very flexible in the *x*-direction, it is preferably very rigid in the *y*-direction. The rigidity against torsion is given by the torsion constant; it should also be as high as possible.

Sim. No.	Suspension	Beam Width	kx [N/m]	ky [N/m]	Tor. [Nm/rad]
1	Type 1	6 μm	0.9166	675.07	2.444 E-7
2	Type 2	6 μm	0.8961	673.25	1.752 E-7
3	Type 3	6 μm	0.8961	714.29	1.731 E-7
4	Type 1	10 μm	0.9268	1897.13	1.096 E-6
5	Type 2	10 μm	0.9225	1897.13	7.127 E-7
6	Type 3	10 μm	0.9225	1706.80	6.952 E-7
7	Type4	10 μm	0.9225	15.39	1.235 E-7

Table 2.1 The results of the finite element modeling of different folded beam suspensions.

First, from the table it can be seen that the beam width has a great influence on the rigidity of the structure. For all the designs, an increase of the beam width from 6 μm to 10 μm has the following effect: while the spring constant in *x*-direction changes only by a few percents, the rigidity in *y*-direction increases by approximately a factor of three and the torsional rigidity against twisting moments increases by roughly a factor of four.

The center square piece, respectively the center H-piece seem to have an effect on the rigidity against torsion - an improvement of 40 - 50 % for the square-piece is observed. The choice of the center piece, however, has little effect on the spring constants. The difference between suspension Type 2 and Type 3 is that the clamped supporting beams are outside, respectively inside the rest of the structure. This seems to have a rather small influence on the spring constants and the torsional rigidity. The suspension Type 4 has only disadvantages. The stiffness in the y-direction is completely lost; compared to Type 2, it is more than a factor 100 smaller. Also the rigidity against torsion is about a factor of 6.5 lower. For a given beam width, the suspension Type 3 has the highest spring constant in y-direction while the suspension Type 1 shows the highest rigidity against torsion.

The study shows that there are considerable differences between the seven designs. However, the factor that influences the rigidity most is the width of the supporting beams. The model does not take into account buckling of the suspension beams. Whatsoever, experiments on fabricated structures have demonstrated that not only continuous bending but also buckling can be a failure mechanism resulting in side sticking. Section 4.1.3 reports observations on the deformation of the suspension caused by electrostatic sticking; it is illustrated that for certain structures elastic properties as well as deformation of the suspension are predicted accurately.

2.2.4 Compact suspensions for optical shutters

Traditional micromechanical comb actuators require folded beam suspensions, which occupy a rather large surface in the range of 0.1 mm^2 [2.15, 2.16]. For optical applications, a high density of active elements is required; therefore, the surface occupied by the suspension has to be reduced. The problem hereby is that the high selectivity of compliance, i.e., the spring constant in the stroke direction is much lower than the spring constant in the transverse direction, has to be maintained. Using ANSYS®, a meander shaped folded beam suspension has been developed, which offers still a high selectivity of compliance while the surface occupied by the suspension has been reduced by one order of magnitude.

The idea was to use meander shaped suspensions as shown in Figure 2.14. The design had now to be optimized in order to achieve the high selectivity of compliance and a minimum surface occupied by the suspension. The elements used for the simulation are STIF 4 elements. The optimized design is shown in Figure 2.15. The beams have a height t of 2 μm and a width w of 0.4 μm or 8.4 μm; the suspension has three long double beams, where the length L_1 is 120 μm and two short double beams, where the length L_2 is 50 μm. These dimensions will be the standard dimensions for the double beam meander suspension. The inverse of the spring constant k_x for the folded beam meander structure can be expressed as (springs in series)

$$\frac{1}{k_x} = \frac{3L_1^3}{24EI} + \frac{2L_2^3}{24EI} \tag{2.33}$$

where three double beam springs with long beams and two double short beams are assembled in series. Calculation of the spring constant gives a value of 8.0 mN/m for the double beam meander suspension with standard dimensions.

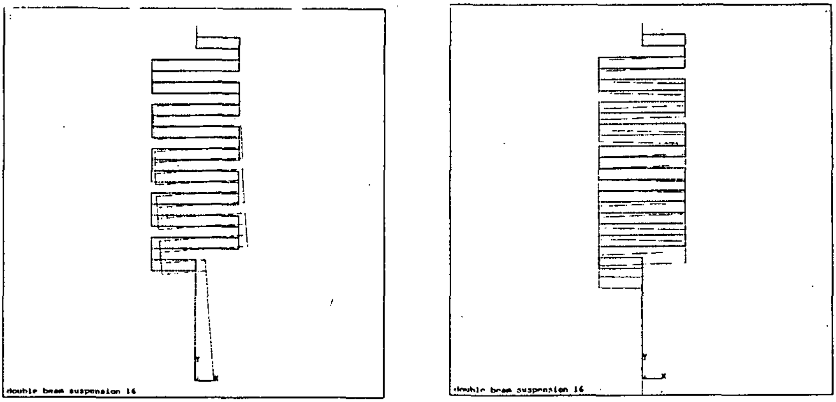

a) b)

Fig. 2.14 Layouts (not optimized) of folded beam meander suspensions with loads: **a)** in y-direction; **b)** x-direction.

The shutter has a width of 24 µm, a length of 100 µm, and a thickness of 2 µm. This gives a rather large mass for the shutter (11.0 ng) compared to the suspensions (4.2 ng). Therefore, for a rough estimation of the resonance frequency, the moving mass of the suspension will be ignored; the calculated first resonance frequency is then 4.29 kHz.

The maximum strain for a 10 µm displacement can be computed by using the same assumptions and theory as in Section 2.2.2. The maximum bending moment is 0.80 pNm - this results in a maximum stress value of 15.0 MPa, which is similar to the value calculated for the standard comb actuator suspension.

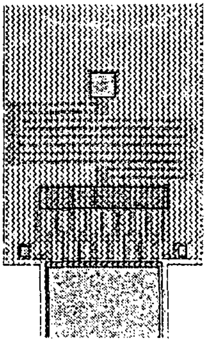

Fig. 2.15 Mask Layout of folded beam meander suspension (optimized design).

The electromechanical performance can be estimated: for the calculated force of a comb actuator in Section 2.1.2, the displacement per voltage squared is 6.91 nm/V^2.

2.2.5 Suspensions for xy-nanopositioners

An *xy*-nanopositioner can be conceived where the actuation is realized by the comb actuators (cf. Figure 2.16). The design is based on a pull mechanism - the table is moved to any position in the *xy*-plane by energizing two of the four comb drives. The decoupling of the *x*- and *y*-position is given by the construction of the suspension.

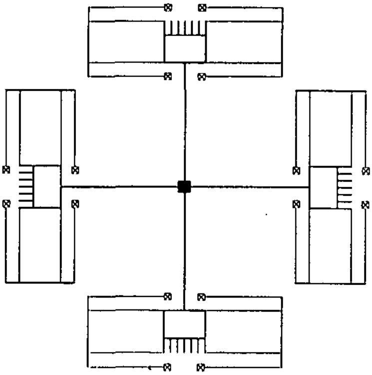

Fig. 2.16 For the *xy*-nanopositioner four comb actuators are assembled in a pull structure.

For calculating the flexibility in x- and y-direction, the following three springs, which are in parallel, have to be considered: the two springs of the comb actuators and the spring resulting from the transverse beam of the pull assembly. The last spring will be regarded as a beam where the two ends are fixed. The constant m for Equation 2.28 is in this case 192. Hence, the total spring constant can be expressed as

$$k_x = 2\frac{4Etw^3}{L_1{}^3 + L_2{}^3} + \frac{16Etw^3}{L^3} \tag{2.34}$$

where L is the total length of the cross beam. For the length L of 700 µm, the spring constant k_x can be computed by employing the standard geometric dimensions for the comb actuators - it amounts to 13.6 mN/m. Using earlier calculations, the displacement per voltage squared can be determined - it is 4.07 nm/V^2.

In a simplified model, the vertical suspension of the stage can be interpreted as an assembly of springs, which are arranged in series and in parallel. Hence, the spring constant k_z, can be expressed as

$$\frac{1}{k_z} = \frac{1}{2}\left(\frac{(L_1 + L_2)^3}{2Et^3w} + \frac{L^3}{16Et^3w}\right) \tag{2.35}$$

Numerical computation using the standard geometric dimensions gives a value of 22.3 mN/m.

FEM simulations of this particular structure showed that precise positioning can be performed because there is a good mechanical decoupling of the displacements in x- and in y-direction. For the simulation, the identical three-dimensional, uniaxial beam elements as already employed for the modeling of the folded beam suspension have been used to build up a model of the stage. For the standard xy-positioner, the simulated coupling is shown in Figure 2.17. As can be deduced from the graph, the absolute position of the stage can deviate due to coupling up to 3.6 %. If the device is used for positioning in the xy-plane in the range of 10 µm by 10 µm, the coupling influences the absolute position less than 180 nm. However, for using this structure as positioner with nanometer precision, compensation has to be employed; by applying corrected voltages, the required precision can be achieved.

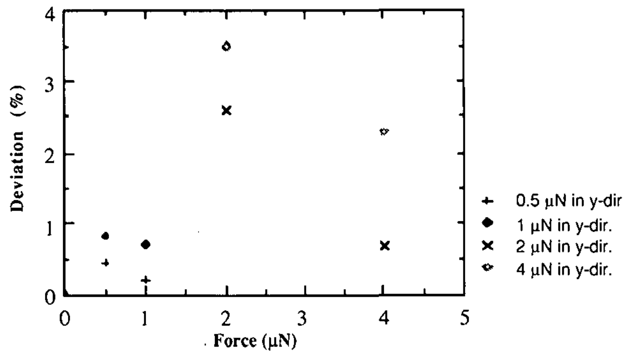

Fig. 2.17 FEM of mechanical coupling of *xy*-nanopositioner. The diagram shows the changes of the *x*-position due to actuation in *y*-direction.

2.3 Suspensions for Vertically Movable Actuators

For vertically movable actuators, the analysis of the suspension employs analytical formulae only. While the suspension for the interference light modulators can be calculated using the theory developed in Chapter 2.2, the twisting bar suspension for the pivoting mirror elements needs additional theoretical background; therefore, the basic theory of torsion will be recalled in Section 2.3.1. As shown in Section 2.3.2, the investigations of the mechanical suspension of interference light modulators is straightforward, and it follows the reasoning of classical textbooks. The pivoting micromirrors discussed in Section 2.3.3 are suspended by two torsion beams, and the analysis is rather simple as well.

2.3.1 Basic theory of torsion

The theory presented in this section is based on the considerations proposed by *Timoshenko* [2.22]. If a shearing stress τ is applied on the element *abcd* of Figure 2.18, it is distorted, and the following relation for a small distortion angle γ, also called the shearing strain, can be established

$$\gamma = \frac{\tau}{G} \tag{2.36}$$

where G is the modulus of torsion. Let an isolated disc be in the following state of strain: there is a rotation of its lower cross section with respect to its upper cross section by an angle of $\mathrm{d}\phi$ (cf. Figure 2.19). Then, the shearing strain γ is found from the triangle cac'

$$\gamma = \frac{c'c}{ac'} \tag{2.37}$$

Since $c'c$ is the small arc of radius r corresponding to the difference $\mathrm{d}\phi$ in the angle of rotation of the two adjacent cross sections, $c'c = r\mathrm{d}\phi$, and we obtain

$$\gamma = \frac{\mathrm{d}\phi}{\mathrm{d}x} r \tag{2.38}$$

The quantity $\mathrm{d}\phi/\mathrm{d}x$ is constant, and it represents the angle of twist per unit length - it will be called Θ. Using Equation 2.36, the shearing stress can be written as

$$\tau = G\Theta r \tag{2.39}$$

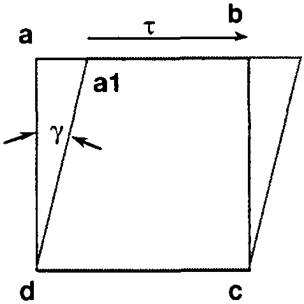

Fig. 2.18 Distortion due to shearing stress [2.22].

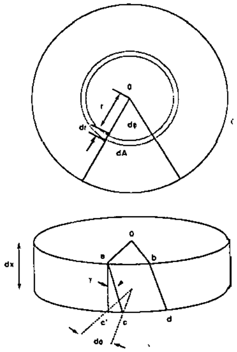

Fig. 2.19 Twisting of a circular shaft [2.22].

Finally, we are seeking a relationship between the applied torque T_m and the stresses it produces. The shearing stresses distributed over the cross section are statically equivalent to a couple equal and opposite to the torque T_m. For each element of area $\mathrm{d}A$ the shearing force is $\tau\mathrm{d}A$. The moment of this force about the axis of the shaft is $(\tau \mathrm{d}A)r = G\Theta r^2 \mathrm{d}A$. The torque T_m is the summation, taken over the entire cross-sectional area, of these moments

$$T_m = \int_A G\Theta r^2 \mathrm{d}A = G\Theta \int_A r^2 \mathrm{d}A = G\Theta I_p = \frac{G\theta I_p}{l} \qquad (2.40)$$

where I_p is the polar moment of inertia, and θ is the total angle of twist. Equation 2.40 can also be used for non-circular cross sections. In this case, however, I_t, the torsional moment of inertia has to be employed instead of I_p, the polar moment of inertia.

2.3.2 Bridges for interference light modulators

A straight beam fixed to the substrate on both ends and suspended over an addressing electrode can be employed as interference light modulator. Two light modulation principles of the simple structure will be explained in Section 4.3.3. Either a phase step is modified, or the device can be operated as a Fabry-Perot interferometer, where the width of an optical resonance cavity is changed. For this bridge structure, the constant m is 192 when using the general Equation 2.28 for determining the spring constant. The standard dimensions for this light modulator are a length L of 70 µm, a width w of 50 µm, and a thickness t of 0.5 µm. The spring constant can be determined - it is 49.6 N/m. The first natural frequency f_1 can be calculated using the following formula [2.25]

$$f_1 = \frac{1}{2\pi}\left(\frac{4.730}{L}\right)^2 \sqrt{\frac{Et^2}{12\rho}} \qquad (2.41)$$

It follows that the resonance frequency is proportional to the thickness of the beam and inversely proportional to the square of the length of the beam.

By using the geometric inputs from above and a density ρ of the polysilicon of 2300 kg/m^3, the calculated resonance frequency is 902 kHz.

The maximum bending moment for a straight beam with fixed ends is $T_{m_{max}} = FL/8$, which is for a vertical displacement of 2 µm equal to 868 pNm. Hence, the maximum stress can be calculated - it is 34.6 MPa. This value is less than 1.0 % of the yield stress.

2.3.3 Torsion beams for pivoting mirror elements

The electric torque T_e, calculated in Section 2.1.5, has to be counteracted by the mechanical torque T_m, created in the torsion suspension. The magnitude of the mechanical torque depends on the geometry and the material properties of the beams, as described in Equation 2.40. Following the reasoning of *Guckel et al.* [2.26], a shear modulus of 66 GPa is assumed for the polysilicon. The torsion bars used for the numerical calculations have a length b of 15 µm and the cross section given above. The torsional moment of inertia for beams with rectangular cross section (width w and thickness t) is given by [2.23]

$$I_t = tw^3 \left(\frac{1}{3} - 0.21 \, \frac{w}{t} \left(1 - \frac{w^4}{12t^4} \right) \right) \quad \text{for } t \geq w \tag{2.42}$$

With the typical dimensions of a torsional micromirror, the torsional moment of inertia I_t can be determined - it is 37.3 10^{-27} m^4. The mechanical torque per degree of twist, T_m/θ, can be derived using Equation 2.40 - it is 328 pNm/rad (both torsion beams are considered). From Equations 2.40 and 2.42, it can be deduced that the torsional moment of the mirrors is inversely proportional to the length and directly proportional to the thickness and the third power of the width of the beams (for $t>>w$). The electromechnical performance of the torsional mirror can be roughly predicted using the electric torque T_e of 8.04 fNm/V2 calculated above. Hence, the twisting angle per voltage squared is 24.5 10^{-6} rad/V^2.

From Equations 2.21 and 2.42, the voltage and the angle of abrupt tilting can be calculated. However, this involves the solving of transcendental equations - they can be determined only numerically [2.27].

The bandwidth of the torsional mirror is determined by its first natural frequency f_1. How much of the bandwidth is actually usable depends on the damping of the system and the application. For calculating the natural frequency, we are assuming that the torsion beams are massless - that is not having a mass moment of inertia. When a mirror element is twisted by an angle ϕ, the torque exerted on the torsion bars is split up equally on them. Thus, the analysis of the torsional mirror is simplified to that of a classical torsional pendulum [2.28]. The torsional natural frequency is then given by

$$f_1 = \frac{1}{2\pi} \sqrt{\frac{2 I_t G}{I b}} \tag{2.43}$$

where b is the length of the torsion beams and I is the mass moment of inertia, which is defined as

$$I = \int_V r^2 \mathrm{d}m \tag{2.44}$$

with r, the distance from the axis of rotation. For square shaped mirror where the torsion bars are fixed near the mirror edge, the mass moment of inertia is $I = \rho t e^4/3$ for $e >> t$, where e is the length of mirror edge. Hence, Equation 2.43 can be expressed as

$$f_1 = \frac{1}{2\pi}\sqrt{\frac{6I_tG}{\rho t b e^4}} \tag{2.45}$$

The natural frequency of the torsional mirror can be computed - it is 81.8 kHz.

Reliability is an important issue for this kind of dynamic structure, and therefore, it is appropriate to investigate also here the maximum stresses encountered. A torsional mirror suspended with torsion bars of rectangular cross section is subjected to a maximum shear stress τ_{max} in the torsion bars; at the midpoint of the wide side it is given by [2.23]

$$\tau_{max} = \frac{T_m(1.5t + 0.9w)}{w^2t^2} \quad \text{for } t >> w \tag{2.46}$$

With the given geometric dimensions and the calculated mechanical torque from above, the maximum shear stress can be determined - it is 114 MPa. This is over 30 times lower than the fracture stress of polysilicon.

References

[2.1] P. Benjamin, *A History of Electricity*, John Wiley, New York, USA, 1898, pp. 506-507.

[2.2] J. Sparks (ed.), *The Works of Benjamin Franklin*, vol. 5, Whittermore, Niles, and Hall, Boston, USA, 1856, p. 301.

[2.3] S. M. Sze, *Semiconductor Devices - Physics and Technology*, John Wiley, Singapore, 1985.

[2.4] F. Paschen, "Ueber die zum Funkenübergang in Luft, Wasserstoff und Kohlensäure bei verschiedenen Drucken erforderliche Potentialdifferenz", *Annalen der Physik*, vol. 37 (1889), pp. 69-96.

[2.5] L. S. Tavrow, "A LOCOS-based microfabricated radial-gap electric motor", *Ph. D. Dissertation*, Massachusetts Institute of Technology, Cambridge, MA, USA, 1991.

[2.6] W. S. N. Trimmer and K. J. Gabriel, "Design considerations for a practical electrostatic motor", *Sensors and Actuators*, vol. 11 (1987), pp. 189-206.

[2.7] S. F. Bart, T. A. Lober, R. T. Howe, J. H. Lang, and M. F. Schlecht, "Design considerations for micromachined electric actuators", *Sensors and Actuators*, vol. 14 (1988), pp. 269-292.

[2.8] A. P. Pisano, "Resonant-structure micromotors: historical perspective and analysis", *Sensors and Actuators*, vol. A20 (1989), pp. 83-89.

[2.9] L. S. Tavrow, S. F. Bart, and J. H. Lang, "Operational characteristics of microfabricated electric motors", *Sensors and Actuators*, vol. A35 (1992), pp. 33-44.

[2.10] U. Wallrabe, P. Bley, and J. Mohr, "Entwicklung, Optimierung und Test von elektrostatischen Mikromotoren nach dem LIGA-Verfahren", *Ph. D. Dissertation*, University of Karlsruhe, Germany, September 1992.

[2.11] B. Puers, E. Peeters, W. Sansen, "CAD tools in mechanical sensor design", *Sensors and Actuators*, vol. A17 (1989), pp. 423-429.

[2.12] F. Pourahmadi, P. Barth, K. Petersen, "Modeling of thermal and mechanical stresses in silicon microstructures", *Sensors and Actuators*, vol. A21-A23 (1990), pp. 850-855.

[2.13] R. L Mullen, M. Mehregany, M. P. Omar and W. H. Ko, "Theoretical modeling of boundary conditions in microfabricated beams", in *Tech. Dig. IEEE Micro Electro Mechanical Systems Workshop*, Nara, Japan, Jan. 1991, pp. 154-159.

[2.14] F. Pourahmadi, D. Gee, K. Petersen, "The effect of corner radius of curvature on the mechanical strength of micromachined single-crystal structures", in *Tech. Dig. 6th International Conference on Solid-State Sensors and Actuators*, San Francisco, CA, USA, June 1991, pp. 197-200.

[2.15] T. Hirano, T. Furuhata, K. J. Gabriel and H. Fujita, "Design, fabrication and operation of submicrometer gap comb-drive microactuators", *J. Electromech. Syst.*, vol. 1, no. 1 (1992), pp. 52-59.

[2.16] W. C. Tang, M. G. Lim, R. T. Howe, "Electrostatic comb drive levitation and control method", *J. Electromech. Syst.*, vol. 1, no. 4 (1992), pp. 170-178.

[2.17] Y.-C. Tai, L.-S. Fan, and R. S. Muller, "IC-processed electrostatic micromotors", *Sensors and Actuators*, vol A20 (1989), pp. 41-47.

[2.18] W. Chr. Heerens and S. D. Tarasenko, "The absolute strain gauge", *Sensors and Actuators*, vol. A25-A27 (1991), pp. 829-833.

[2.19] S. Kumar, D. Cho, and W. N. Carr, "Experimental study of electric suspension for microbearings", *J. Microelectromech. Syst.*, vol. 1 (1992), pp. 23-31.

[2.20] W. C. Tang, T. H. Nguyen and R. T. Howe, "Laterally driven polysilicon resonant microstructures", *Sensors and Actuators*, vol. A20 (1989), pp 25-32.

[2.21] A. P. Pisano and Y.-H. Cho, "Mechanical design issues in laterally-driven microstructures", *Sensors and Actuators*, vol. A21-A23 (1990), pp. 1060-1064.

[2.22] S. Timoshenko, *Strength of Materials, Part I*, Robert E. Krieger Publishing Company, Malabar, Florida, USA, 1956.

[2.23] R. J. Roark and W. C. Young, *Formulas for Stress and Strain*, 5th ed., McGraw-Hill International Editions, Singapore, 1976.

[2.24] S. Timoshenko, D. H. Young, W. Weaver, Jr., *Vibration Problems in Engineering*, 4th ed., John Wiley & Sons, New York, USA, 1974, pp. 31-40.

[2.25] R. Blevins, *Formulas for Natural Frequency and Mode Shape*, R. Krieger Publishing Company, New York, USA, 1979.

[2.26] H. Guckel, D. W. Burns, H. A. C. Tilmans, D. W. DeRoo and C. R. Rutigliano, "Mechanical properties of fine grained polysilicon - the repeatability issue" in *Tech. Digest Solid-State Sensor and Actuator Workshop*, Hilton Head Island, SC, USA, June 1988, pp. 96-99.

[2.27] G. C. Wetsel, K. J. Strozewski, "Dynamical model of microscale electromechanical spatial light modulator", *J. Appl. Phys.*, vol. 73, no. 11 (1993), pp. 7120-7124.

[2.28] A. Higdon and D. W. Stiles, *Engineering Mechanics, Volume II: Dynamics*, Prentice-Hall Inc., Englewood Cliffs, NJ, USA, 1961.

Chapter Three

Fabrication

Bulk micromachining means the construction of micromechanical structures out of the single crystal silicon wafer. In the 1950s, it was discovered that alkaline solutions attack different facets or planes of the silicon wafer at very different angles. Using these etchants, grooves and nozzles have been realized; further, thin membranes can be formed by backside etching of the silicon substrate [e.g., 3.1]. Together with etch-stop techniques [e.g., 3.2], precisely defined membranes and cantilevers are fabricated. For making complex structures, the ability to bond silicon wafers is an important asset to bulk micromachining. Developed in the 1960s, this high temperature process fuses silicon wafers together at the atomic level without the need for an interface layer. Bulk micromachining has meanwhile become a well-established technology [3.3]. Nowadays, a number of companies such as Lucas NovaSensors [3.4], ICSensors [3.5], Silicon Microstructures, Ascom [3.6], and others successfully manufacture and market silicon transducers based on bulk processing.

The first micromechanical device - the resonant gate transistor - fabricated with surface micromachining has been realized in the late 1960s by *Nathanson et al.* [3.7]. In this technology, as sacrificial layer and structural layer, two electroplated metals have been used. However, it was only in the 1980s that surface micromachining has become a technology of widespread interest. In particular, the development of a polysilicon technology by *Howe and Muller* [3.8] attracted a lot of attention. Such three-dimensional microstructures are located on the wafer surface and consist of structured and partially free standing thin films [3.9]. An advantage of surface-micromachined devices is their easy integration with electronic components since the wafer surface is also the working area of integrated circuits (IC). Compared to bulk micromachining, there are fewer - however, an increasing number of devices - fabricated by surface micromachining at a commercial level. In contrast to the bulk micromachined devices, active development of new devices is mainly performed by large size chip manufacturers such as Texas Instruments [3.10], Motorola [3.11], and Analog Devices [3.12].

In this work, surface micromachining, bulk micromachining, and also the combination of the two will be discussed. Chapter 3.1 treats the polysilicon surface micromachining with emphasis on the characterization of anisotropic dry etching of polysilicon, which is a key step for the fabrication of highly flexible suspensions. Chapter 3.2 presents the surface micromachining of aluminum devices, where the new process step is the etching of the sacrificial silicon dioxide layer without attacking the structural aluminum. Finally, Chapter 3.3 discusses the single crystal silicon surface and bulk micromachining. Further, the combination of the two are presented in view of the fabrication of an integrated scanning force microscope (SFM).

3.1 Polysilicon Surface Micromachining

Low-pressure chemical vapor deposited (LPCVD) polycrystalline silicon (polysilicon) is a well-known material for the fabrication of gate electrodes and interconnections in standard IC production facilities. Apart from its favorable electric properties, it has excellent mechanical properties, which are similar to those of single crystal silicon [3.13]. For these reasons, polysilicon is an interesting material for the realization of micromechanical structures in an IC-compatible fabrication process. In particular, free-standing polysilicon structures can be realized by the sacrificial layer technology, whose key processing steps are the following: deposition and patterning of a sacrificial silicon dioxide layer, deposition and structuring of a polysilicon film, and removal of the sacrificial oxide by lateral etching in hydrofluoric acid. This processing sequence results in patterns which are completely free-standing, where the polysilicon covered the oxide. While, as already stated in the introduction, polysilicon surface micromachining was developed in the United States [3.8, 3.14, 3.15], in Europe pioneering work on polysilicon resonators has been performed at the Institute of Microtechnology (IMT) by *Linder et al.* [3.16, 3.17].

Section 3.1.1 describes the two layer polysilicon process, which is the basic technology for the different devices presented in this work. Section 3.1.2 focuses on the anisotropy of the dry etching process. The control of this processing step is essential for the construction of the mechanical suspension as well as the electrodes. In particular, the influences of the photoresist environment and the processing pressure on the anisotropy of etching are investigated.

3.1.1 Two-layer polysilicon process

While the polysilicon process developed in our laboratory for the resonator and microswitch applications [3.17] employed a diffusion in the substrate to define a counter electrode, it was decided that for the present work a first thin polysilicon layer shall be used for this purpose. The reasoning was that it is advantageous to separate the two electrodes only by an air gap and not by an additional dielectric layer, where always a risk of trapped charges exists. Further, by having both electrodes isolated from the grounded substrate by a dielectric layer instead of a pn-junction, the devices can be operated at higher voltages (up to 200 V). As will be shown later, this approach has also an unforeseen advantage in view of controlling the surface sticking of the movable structure.

The devices are fabricated in collaboration with the Swiss Center for Electronics and Microtechnology Inc. (CSEM). An overview of the three mask fabrication sequence is given in Figure 3.1. First, the substrate is passivated by a silicon dioxide / silicon nitride double layer: a 900 Å thick thermal oxide is grown on a n-type silicon substrate, afterwards a 1500 Å thick LPCVD nitride is deposited (Figure 3.1a); it serves as insulator and as etch stop layer during the final step of the sacrificial oxide. A 0.2 μm thick LPCVD polysilicon film is used as ground plate and for interconnection (Figure 3.1b). A five weight percent phosphorus-doped CVD silicon dioxide (low temperature oxide) with a thickness of 2 μm serves as sacrificial layer (Figure 3.1c); in the following, this film is also called phosphosilicate glass (PSG). A second, 2 μm thick polysilicon is deposited by LPCVD (thermal decomposition of silane) at 600 °C and 200 mTorr. The deposition temperature is close to the transition temperature at 200 mTorr from amorphous to (poly)-crystalline layers (≈580°C, e.g., [3.13]). Thermal annealing in nitrogen converts the as-deposited, built-in compressive strain into a controllable tensile strain depending on the annealing temperature [3.18]. For our polysilicon, the optimum conditions have been found to be an anneal at 1050 °C for 30 minutes [3.16]. During the anneal, it is also doped by diffusion from the sacrificial layer as well as from a second phosphorus-doped oxide on top of it (Figure 3.1d).

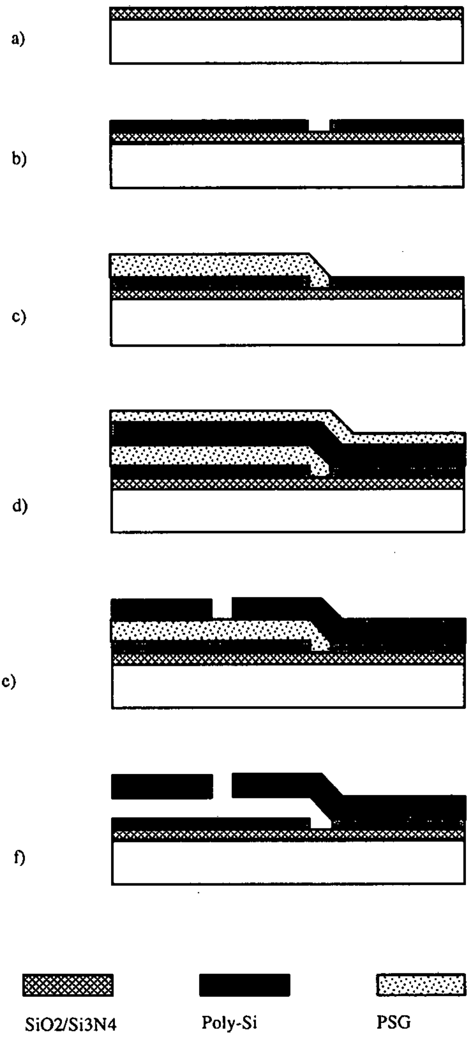

Fig. 3.1. Two layer polysilicon process: **a)** passivation of substrate by a silicon oxide / silicon nitride stack; **b)** deposition and patterning of first polysilicon layer (Mask 1); **c)** deposition and patterning of sacrificial oxide (Mask 2); **d)** deposition of second polysilicon layer and second phosphorus-doped oxide, diffusion, and anneal; **e)** removal of second phosphorus-doped oxide and patterning of second polysilicon (Mask 3); **f)** etching of sacrificial oxide.

With this process it is possible to construct comb actuators with long suspension beams, which do not exhibit any buckling. A further delicate processing step is the etching (Figure 3.1e) of the submicrometer wide suspension beams, which guarantees the high flexibility and consequently the large displacements of the actuators at low driving voltages. A standard photoresist is used for the patterning of the polysilicon by dry etching in a C_2ClF_5/SF_6 plasma [3.19]. As will be shown in Section 3.1.2, high selectivity, controlled undercut, and almost vertical sidewalls are accomplished. The final processing step is the release of the mechanically movable parts (Figure 3.1f). The wafers are immersed in buffered hydrofluoric acid (BHF); a lateral etch rate of 0.25 µm/min has been established for the phosphorus doped oxide in BHF 7:1. Afterwards, the devices are rinsed in isopropyl alcohol; great care has to be taken that the released structures are not destroyed by rough handling in the liquids.

The maximum length of free-standing bridges, straight beams fixed to the substrate on both sides, is about 600 µm; most longer bridges are sticking on the substrate. As cause for the stiction, different forces like process-induced electrostatic forces [3.20], van der Waals forces, solid bridging, and liquid bridging have been proposed [3.21]. Figure 3.2 displays a finished device - the

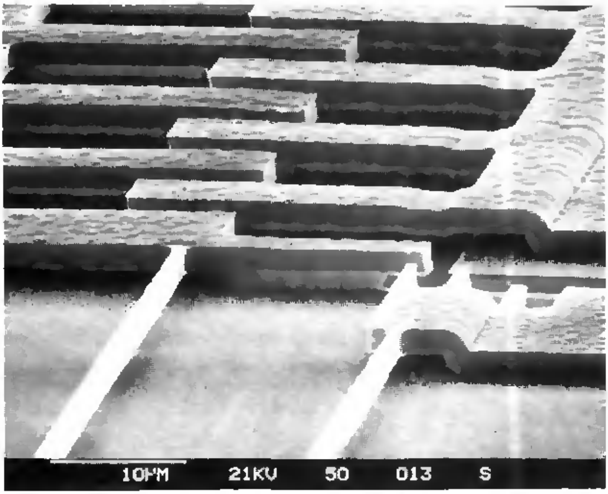

Fig. 3.2 Detail (SEM) of finished comb actuator showing the precise profile of the polysilicon etching as well as other processing steps.

detailed view allows to visualize the different process steps.

The sheet resistance of the finished polysilicon structure has been measured using a four point probe. It is 144 Ω per square, which results in an average resistivity of 28.8 mΩcm. Further mechanical and optical properties of the polysilicon devices are given in Chapter 5.

3.1.2 Anisotropic etching of polysilicon

In this section etch tests performed on a Leybold Z401S dry etching machine using a C_2ClF_5 / SF_6 gas mixture will be discussed. The equipment is a parallel plate reactor powered by a 13.56 MHz generator. For our experiments, the RF power is capacitively coupled to the upper electrode while the wafer is sitting on the grounded lower electrode plate (plasma etch mode). The gases are fed into the reaction chamber through a shower head in the upper electrode. For the tests, a sequence of layers has been used which is simpler than the one required for the actuator structures. A silicon dioxide / silicon nitride sandwich is used for the passivation followed by a LPCVD polysilicon having a thickness of 1.2 - 1.4 µm. Afterwards, a CVD silicon dioxide sandwich (1000 Å 5% P-doped, 3000 Å non doped) is deposited. The polysilicon is doped and annealed at the conditions given in Section 3.1.1. In the following, the CVD silicon dioxide is removed, and an Olin Hunt 6517 photoresist is used for the photolithography; it has a thickness of 2 µm. The initial etch conditions were taken from previous experiments [3.16]. For all runs, the power has been fixed at 160 Watt, and the C_2ClF_5 and SF_6 gas flows have been equal at a setting of 11 sccm. The only factors which have been varied are the time and the pressure. These settings as well as the etch depth and the remaining resist thickness are given in Table 3.1. The complete processing sequence is illustrated in Figure 3.3. Figure 3.4 displays the results from the table graphically. There are mainly two things that can be concluded from the diagram. First, two etch velocities can be clearly distinguished. During the first four minutes mainly polysilicon is etched - the etch velocity is high (3'500 Å/min). Throughout the second four minutes, only nitride is etched - the etch velocity is low (320 Å/min). The second conclusion is that the polysilicon etch rate seems to depend on the process pressure - the lower the pressure the higher the etch rate. The selectivity of the etch rates of polysilicon versus photoresist is 2.5. Hence, if a standard resist of 2 µm thickness is used, a maximum layer of about 5 µm polysilicon can be etched.

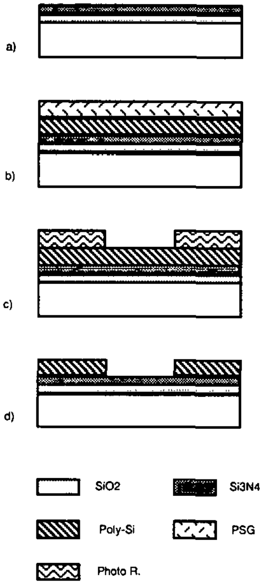

Fig. 3.3 Processing sequence for etch test structures: **a)** deposition of SiO_2-Si_3N_4 sandwich for isolating the substrate; **b)** deposition of polysilicon and PSG, doping, and annealing of polysilicon; **c)** removal of PSG, deposition, and patterning of photoresist; **d)** RIE of test structures and removal of photoresist.

Time [min]	Pressure [mbar]	Step [Å]	Photoresist [Å]
0	0.00	0	20'850
2	0.07	9'000	16'500
4	0.07	13'850	14'950
8	0.07	14'600	13'250
2	0.10	7'850	17'650
4	0.10	14'000	15'200
8	0.10	15'250	12'300
2	0.13	6'950	18'150
4	0.13	13'900	15'550
8	0.13	15'750	12'450

Table 3.1 Summary of etch tests.

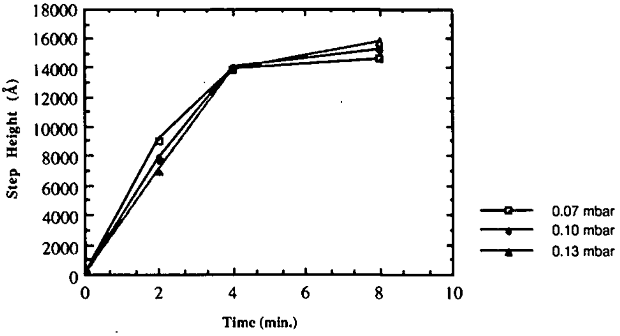

Fig. 3.4 Etch velocities at different process pressures.

Another goal of this test run was to get information about the etch anisotropy. There, the observation has been made that the anisotropy depends to a large degree on the photoresist environment. The two SEM pictures in Figure 3.5 visualize the profile of two polysilicon lines. While Figure 3.5a displays a line positioned in the middle of a dense array of lines with a small 2 μm spacing between each other, Figure 3.5b shows a line positioned in an array which is more spread out; the spacing between the lines is about 10 μm. The profile on the two pictures is different - the dense lines have a much higher anisotropy. Since it would not be very instructive to reproduce all the SEM pictures, the results are summarized graphically in Figure 3.6. The following expression for determining the degree of anisotropy A_f has been used [3.22]

$$A_f = 1 - \frac{v_l}{v_v} \tag{3.1}$$

where v_l and v_v are the lateral and the vertical etch rates, respectively. For determining the lateral etch velocity, the minimal line width has been employed. On the x-axis the different line types are given: 2 min. D are the lines out of the dense array of lines which were etched during two minutes; 2 min. A are the lines out of the spread out array of lines which were also etched for two minutes; 4 min. D and 4 min. A are the line profiles out of the respective arrays etched for four minutes.

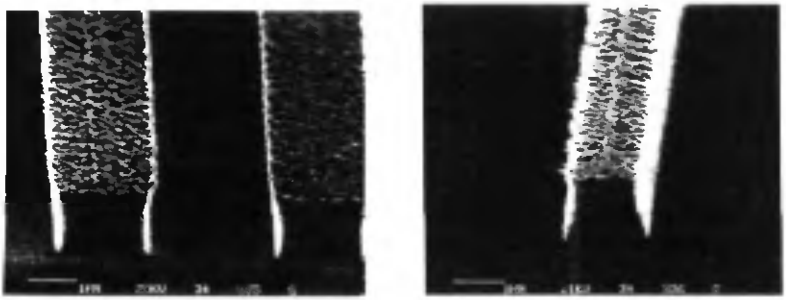

a) b)

Fig 3.5 SEM pictures of 2 µm lines dry etched under the following conditions: power 160 Watt, pressure 0.1 mbar, C_2ClF_5-flow 11 sccm, SF_6-flow 11 sccm, time 4 min. **a**) lines from a dense array of lines; **b**) line from a spread out array of lines.

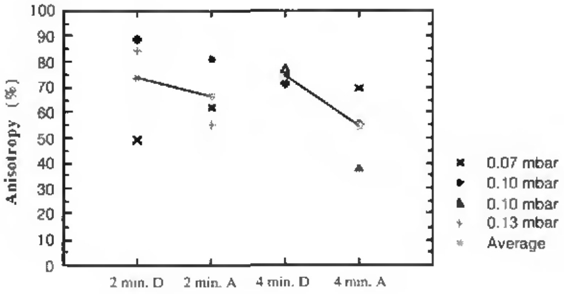

Fig. 3.6 Etch anisotropy for different conditions. Two minute and four minute etch time. D: lines from dense arrays; A: lines from spread out arrays of lines.

Two conclusions can be drawn. First, there is a repeatable difference between the anisotropy of the dense lines and the anisotropy of the spread out lines. This confirms earlier observations reported by *Mc Vittie and Gonzales* [3.23] that the photoresist around the structure influences the lateral etch rate. Second, the process pressure does not have a repeatable effect on the anisotropy - cf. Figure 3.6, where two consecutive runs at 0.1 mbar showed different anisotropy. Concerning the shape of the profiles, the trend is that the lines out of the dense arrays have preferably a V shaped profile while the lines out of the spread out arrays have an A shaped profile.

3.2 Aluminum Surface Micromachining

Since the late 1960s, thin metal films have been used for the fabrication of micromechanical devices. In particular, the sacrificial layer technology has been used employing a metal in the following structural-sacrificial layer combinations: metal-metal by *Nathanson et al.* [3.7], chrome-polyimide by *Schmidt et al.* [3.24], and aluminum-photoresist by *Hornbeck* [3.25]. Other devices are using metallized layers like thin polymer films [3.26, 3.27]. Compared to other metals, aluminum is an interesting material for micromachining because it has to be annealed at a relatively low temperature only for getting a stress free structure [3.28]. Further, it is a well characterized material in microelectronics, and therefore, the technology allows an easy integration of the mechanics and electronics.

In the following section, a novel processing sequence is presented which uses aluminum as the structural layer and silicon dioxide as the sacrificial layer.

3.2.1 Single mask aluminum process

For investigating this new surface micromachining technology, the single mask process, as shown in Figure 3.7, proves to be an efficient tool. A 2 μm thick aluminum (Al1%Si - alloy of pure aluminum and one weight percent of silicon) film is sputter deposited over a phosphorus doped CVD silicon dioxide. In order to release the initial compressive stress, an annealing in N_2-atmosphere at 450 °C during 30 minutes has been performed. Afterwards, the film is structured by RIE on a Leybold Z401S dry etching machine employing a Cl_2-$SiCl_4$-N_2 chemistry.

The final, delicate process step is the releasing of the aluminum structures. Since BHF etching will attack also the aluminum, the selectivity of SiO_2 to Al has to be increased. Two types of inhibitors proved to effectively decrease the velocity of etching the aluminum. One is polyhydric alcohols, which are peptizing the corrosion product of aluminum, i.e., bring it into the colloidal solution; thereby, the total corrosion rate falls off [3.29]. In particular, glycerol added to the BHF has been successful [3.30]. The following etch solution has been used: 3 parts of BHF (7:1) and 1 part of glycerol. For our applications, this method has been particularly useful when an aluminum metallization has to be protected which is on top of the polysilicon structural layer. The lateral etch rate of the PSG is only slightly modified - it is around 0.21 µm/min compared to 0.25 µm/min without added glycerol. The etch rate of the unannealed Al1%Si is drastically reduced, and aluminum mirrors resist etching over two hours. An advantage of this etching technique is that the initial high reflectivity is hardly modified. However, for annealed aluminum structures the selectivity is not high enough and the second method has to be employed.

The etch rate of Al can also be suppressed by chemically biasing the reaction towards electrochemical passivity with small amounts of strong oxidizers [3.29]. Added potassium dichromate ($K_2Cr_2O_7$) is very efficient [3.31]. The following process has given optimum results: before etching the chips are immersed in a 0.01 M water solution of $K_2Cr_2O_7$ for 30 minutes at 20 °C, this step produces already a thin layer of protective Al_2O_3; then, the chips are etched in a 0.005 M solution of $K_2Cr_2O_7$ in BHF (7:1) at a temperature of 0 °C during about 2.5 hours. The selectivity of etch velocities is more than 50 for etching silicon dioxide and aluminum respectively. As can be seen in Figure 3.8, the surface of the etched aluminum gets very rough. A further disadvantage of this method is that the silicon will also be attacked; because the potassium bichromate is a strong oxidizer, a silicon dioxide is formed on the silicon surface which is etched by the BHF.

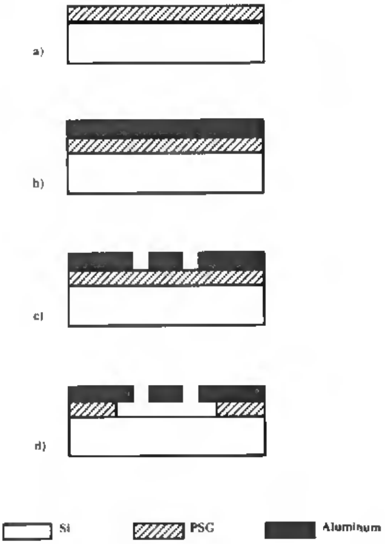

Fig. 3.7 Single mask aluminum process: **a)** deposition of 2 μm PSG, **b)** sputter deposition of 2 μm of aluminum (Al1%Si), **c)** patterning of aluminum by dry etching, **d)** liberating structures by etching in a BHF-$K_2Cr_2O_7$ solution.

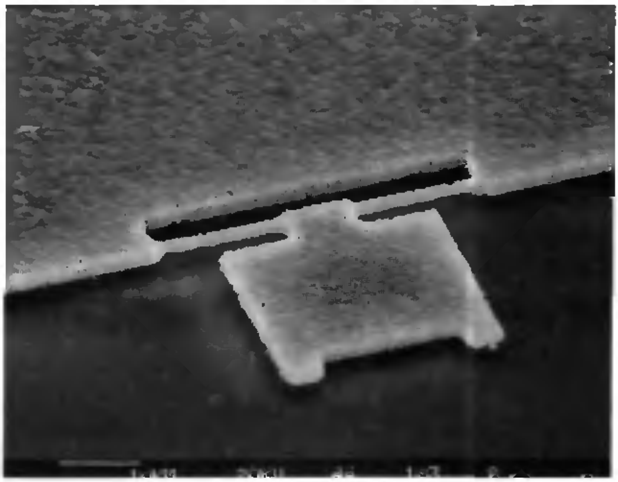

Fig. 3.8 Top view (SEM) of a surface micromachined mirror in aluminum. Due to the processing in the BHF-$K_2Cr_2O_7$ etch solution, the surface of the aluminum is very rough.

3.3 Silicon Surface and Bulk Micromachining

While the surface micromachining in polysilicon and in aluminum are newer technologies, the silicon bulk micromachining is the traditional technology in which still most of the commercially successful devices are fabricated [3.3]. The mechanical properties of silicon are very similar to those of polysilicon (cf. Chapter 5.1). The main interest of studying silicon surface micromachining in the frame of this project is its readiness to a combination of surface and bulk micromachining. Further advantages with respect to polysilicon micromachining exist. First, the single crystal layer as well as the "spacer" gap can be both substantially thicker compared to the thin film sacrificial etching process [3.32]. Second, both the mechanical and electrical characteristics of single crystal silicon are easily and universally reproducible with no special equipment requirements. Third, single crystal silicon has the capability of providing well-characterized diffused resistors with large, well-known piezoresistive coefficients for stress sensing [3.33]; since we are considering only electrostatic actuators in this work, we will not take advantage of this fact.

Recently, silicon on insulator substrates (SOI) have been used for the surface micromachining of silicon. The insulating layer is for example a silicon dioxide formed by a separation by ion implantation of oxygen (SIMOX). This technology developed by *Diem et al.* allowed to develop a variety of surface micromachined silicon devices [3.34]. However, for the fabrication of the devices, which are described in the following, bonding is a key step. The technical term for this process is silicon fusion bonding (SFB); at elevated temperatures two oxidized wafers are fused together to form a bi-crystal structure. Compared to other bonding techniques, no intermediate adhesives have to be used. The effect was first applied by NEC in the early 1960s [3.35], later it was described and explained by *Lasky* [3.36]. Since then, it has found many applications in micromechanics [3.37, 3.38].

The other key step in our bulk micromachining process is the effect that potassium hydroxide (KOH) will attack silicon anisotropically - it has an etch velocity of silicon in <100> direction, which is much higher than in <111> direction. The ratio of etch rate of plane (100) to etch rate of plane (111) is approximately 150 for KOH 40 weight percent at 60 °C. KOH is easy to handle and relatively harmless. A further advantage is that standard IC materials as silicon dioxide or silicon nitride can be used as masks.

Section 3.3.1 describes the single mask process which allows the surface micromachining of silicon structures. Based on this experience, a more complicated process has been developed permitting the combination of silicon bulk and surface micromachining. This technology is presented in Section 3.3.2 in view of the fabrication of an integrated SFM.

3.3.1 Single mask silicon process

The structure is fabricated employing a combination of SFB, wafer thinning in KOH, and patterning by dry etching (cf. Figures 3.9 and 3.10). The process starts with two phosphorus doped (0.03 Ωcm), double-side polished 280 µm thick silicon wafers with (100) crystalline orientation which are thermally oxidized to 1.5 µm. After a cleaning and hydrophilization procedure in HNO_3 and H_2SO_4:H_2O_2, both wafers are aligned and "sandwiched" face to face. The hydrobond forces are strong enough to keep the wafers together on the SiO_2-SiO_2 contact surfaces while transporting the stack into the annealing furnace. SFB at 1100 °C during about 4 hours seals the wafers together [e.g., 3.39]. Then, the thermal oxide on the upper wafer is removed, and the wafer is thinned down to a thickness of about 3 µm in a KOH solution at 60 °C. Since the etch rate of this solution is around 17 µm/h, more than half a day is required for the etching. The thickness of the membrane is defined by a timed stop. Because the etch velocity of KOH is not very repeatable, at certain intervals the sheet resistance of the remaining membrane has been determined with a four point probe. The resistivity of the silicon wafer is known; hence, these measurements allow to calculate the thickness of the membrane. Afterwards, the identical dry etching process as employed for the structuring of the polysilicon devices (see Section 3.1.2) is used for patterning the silicon membrane. Finally, the devices are released by a timed etching in BHF. While the smaller surfaces are completely under etched, the larger surfaces are still fixed to the substrate and can be used as stator electrodes. The postetching procedure is identical to the one described in Section 3.1.1.

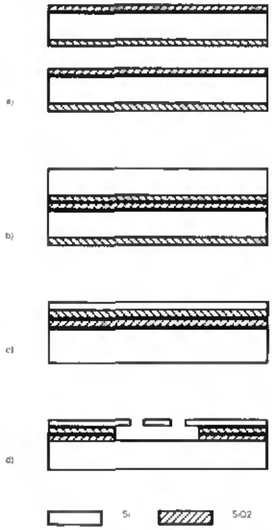

Fig. 3.9 Processing sequence for the fabrication of surface micromachined silicon structures: **a)** hydrophilisation of two thermally oxidized (1.5 µm SiO_2) silicon wafers, **b)** prebonding due to physical contact and SFB in furnace, **c)** thinning of upper wafer in KOH, **d)** patterning of silicon membrane and liberating of device by timed BHF etching.

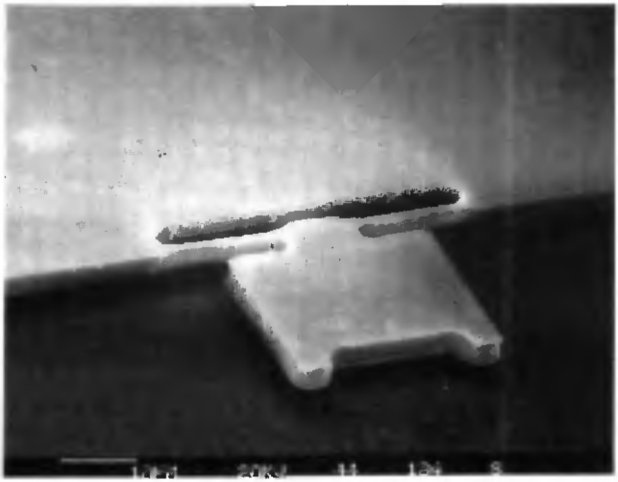

Fig. 3.10 Details (SEM) of a surface micromachined silicon torsional mirror. The surface of the finished device is particularly smooth when employing KOH wafer thinning.

3.3.2 Combination of silicon surface and bulk micromachining

For constructing complex microsystems, it is useful to combine single crystal silicon surface and bulk micromachining. Devices for which such a sophisticated technology is a preliminary requirement for the fabrication are integrated SFM systems and optical shutters with integrated via holes. In the following, the fabrication of an integrated SFM unit will be discussed. For constructing this device, it will be important that the processes for patterning the actuator and for structuring the tip are separated. In the process displayed in Figure 3.11, this has been achieved by performing the two processes on the opposite sides of a wafer. The process starts with two oxidized wafers as described in Section 3.3.1. On one wafer, the actuator geometry is structured by dry etching (see Section 3.1.2); on the other wafer, the opening of the later via hole is already patterned in the oxide by BHF etching. After the hydrophilization procedure, described in the previous section, the wafers are prebonded on an Electronics Visions AL6-2 aligner. This equipment allows a double-side alignment with a precision of better than 2 µm. Afterwards, the SFB is performed under conditions described in the previous section. In the following, bulk back-etching is done in KOH; by a timed stop, a membrane of about 15 µm is left. Then, by thermal oxidation a SiO_2 layer of 1 µm is grown; it is patterned on the upper membrane to form 15 µm wide oxide pads aligned to the reference marks on the wafer [3.40]. A series of dry etching steps is performed afterwards to etch the sharp pyramidal tips by exploiting the lateral underetching of the SiO_2 pad [3.41]. Additional wet etching in a mixture of $HF:HNO_3:CH_3COOH$ simultaneously finishes the shaping of the tip and pierces through the membranes [3.42]. Finally, selective etching of the sacrificial SiO_2 in BHF liberates the movable actuator. Due to the holes through the membranes, the SFM systems become very fragile, especially when processing the liberated structures in the liquids. Hence, any fast or abrupt movements have to be avoided during the postprocessing.

Figure 3.12 displays the finished SFM system fabricated by the combination of bulk and surface micromachining. The working principle of the device will be explained in Chapter 4.2.

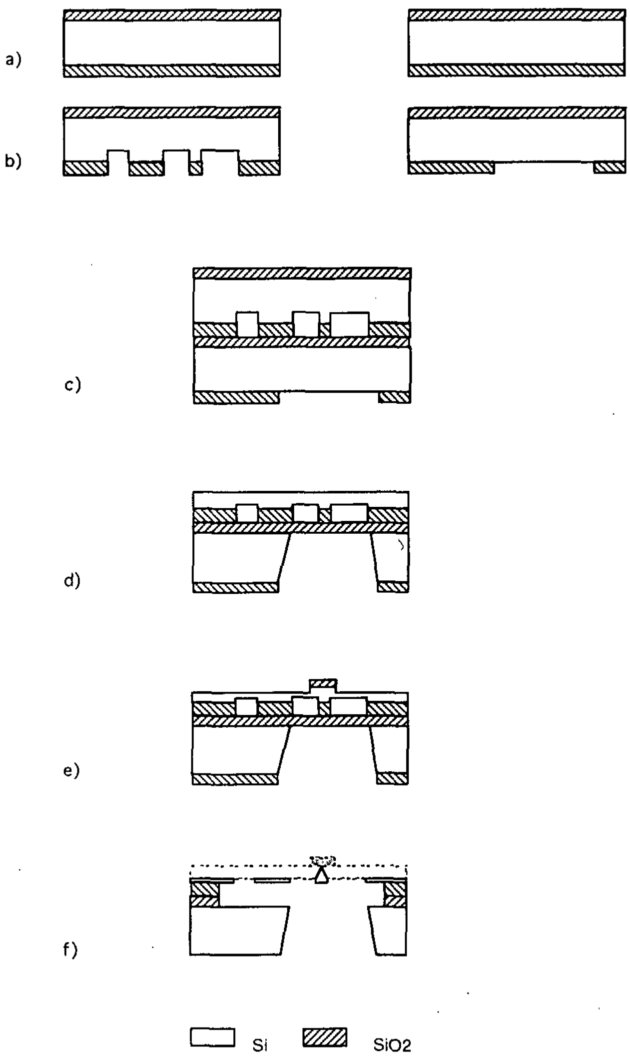

Fig. 3.11 Process sequence of an integrated tip-scanning unit fabricated by a combination of silicon surface micromachining and bulk micromachining: **a)** thermal oxidation of wafers (1.5 µm); **b)** patterning of actuator on one wafer and mask for via hole on the other wafer; **c)** aligned SFB; **d)** KOH etching from both sides, leaving a membrane of 15 µm on top; **e)** forming of the tip by dry etching; **f)** forming of the tip by wet etching, liberating of the actuator in BHF.

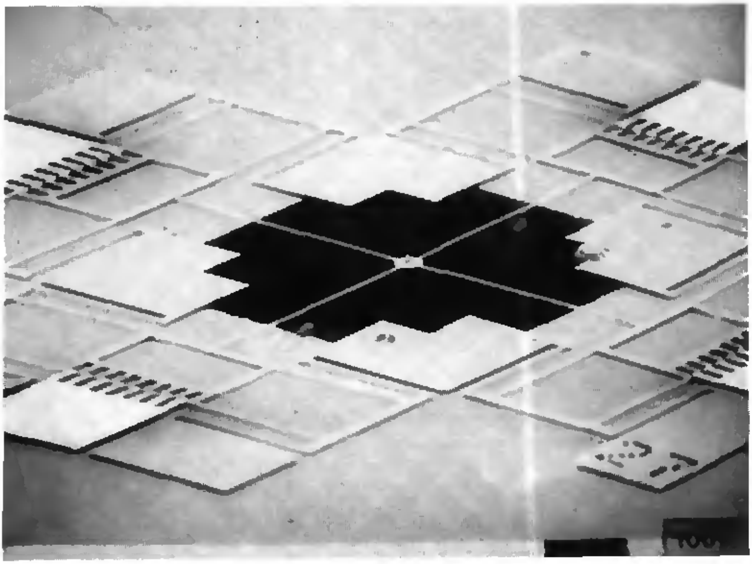

Fig. 3.12 SEM micrograph of a tip-scanning unit fabricated by a combination of silicon surface and bulk micromachining.

References

[3.1] H. Seidel, "The mechanism of anisotropic, electro-chemical silicon etching in alkaline solutions", in *Tech. Dig. IEEE Solid-State Sensor and Actuator Workshop*, Hilton Head Island, SC, USA, June 1990, pp. 86-91.

[3.2] B. Kloeck, S. D. Collins, N. F. de Rooij, and R. L. Smith, "Study of electromechanical etch-stop for high-precision thickness control of silicon membranes", *IEEE Trans. Electron Devices*, vol. 36, no. 4 (1989), pp. 663-669.

[3.3] K. Petersen, "Silicon as a mechanical material", *Proc. IEEE*, vol. 70 (1982), pp. 420-457.

[3.4] L. A. Christel, K. Petersen, "A catheter pressure sensor with side vent using multiple silicon fusion bonding", in *Tech. Dig. 7th International Conference on Solid-State Sensors and Actuators*, Yokohama, Japan, June 1993, pp. 620-623.

[3.5] H. Allen, S. Terry, D. de Bruin, "Accelerometer Systems with built-in testing", *Sensors and Actuators*, vol. A21-23, 1990, pp. 381-386.

[3.6] A. J. van der Wiel, N. F. de Rooij, and A. C. Hoogerwerf, "A calometric mass-flow sensor for hostile environment", in *Tech. Dig. 7th International Conference on Solid-State Sensors and Actuators*, Yokohama, Japan, June 1993, pp. 800-803.

[3.7] H. C. Nathanson, W. E. Newell, R. A. Wickstrom, and J. R. Davis Jr., "The resonant gate transistor", *IEEE Trans. Electron Devices*, ED-14 (1967), pp. 117-133.

[3.8] R. T. Howe and R. S. Muller, "Polycrystalline silicon micromechanical beams", *J. Electrochem. Soc.*, vol. 130 (1983), pp. 1420-1423.

[3.9] C. Linder, L. Paratte, M.-A. Grétillat, V. P. Jaecklin, and N. F. de Rooij, "Surface micromachining", *J. Micromech. Microeng.*, vol. 2 (1992), pp. 122-132.

[3.10] J. B. Sampsell, "The digital micromirror device and its application to projection displays", in *Tech. Dig. 7th International Conference on Solid-State Sensors and Actuators*, Yokohama, Japan, June 1993, pp. 24-27.

[3.11] Lj. Ristic, R. Gutteridge, J. Kung, D. Koury, B. Dunn, and H. Zunino, "A capacitive type accelerometer with self-test feature based on a double-pinned polysilicon structure", in *Tech. Dig. 7th International Conference on Solid-State Sensors and Actuators*, Yokohama, Japan, June 1993, pp. 810-813.

[3.12] S. J. Sherman, W. K. Tsang, T. A. Core, R. S. Payne, D. E. Quinn, K. H.-L. Chau, J. A. Farash, S. K. Baum, "A low cost monolithic accelerometer; product/technology update", *IEDM*, 1992, pp. 501-504.

[3.13] T. I. Kamins, "Design properties of polycristalline silicon", *Sensors and Actuators*, vol. A21-A23 (1990), pp. 817-824.

[3.14] H. Guckel, "Surface micromachining for microsensors and microactuators", *Sensors and Actuators*, vol. A28 (1991), pp. 133-146.

[3.15] M. Mehregany, K. J. Gabriel, and W. S. N. Trimmer, "Integrated fabrication of polysilicon micromechanisms", *IEEE Trans. Electron Devices*, vol. 35 (1988), pp. 719-730.

[3.16] C. Linder, "Electromechanical polysilicon structures and micromachining processes for sensor and actuator applications", *Ph. D. Dissertation*, Neuchâtel, Switzerland, 1993.

[3.17] C. Linder and N.F. de Rooij, "Investigations on free-standing polysilicon beams in view of their applications as transducers", *Sensors and Actuators*, A21-23 (1990), pp. 1053-1059.

[3.18] H. Guckel, D. W. Burns, H. A. C. Tilmans, D. W. de Roo, and C. R. Rutigliano, "Mechanical properties of fine grained polysilicon; the repeatability issue", *IEEE Solid-State Sensors Workshop*, Hilton Head Island, SC, USA, June 1988, pp. 96-99.

[3.19] C. Linder, T. Tschan, N. F. de Rooij, "Deep dry etching of silicon - a novel micromachining technique", *Sensors and Materials*, vol. 3, no. 6 (1992), pp. 311-324.

[3.20] H. Guckel, J. J. Sniegowski, and T. R. Christenson, "Advances in processing techniques for silicon micromechanical devices with smooth surfaces", *Tech. Dig. IEEE Micro Electro Mechanical Systems Workshop*, Salt Lake City, UT, Feb. 1989, pp. 71-75.

[3.21] R. L. Alley, G. J. Cuan, R. T. Howe, and K. Komvopoulos, "The effect of release-etch processing on surface microstructure stiction", in *Tech. Dig. IEEE Solid-State Sensors and Actuators Workshop*, Hilton Head Island, SC, USA, June 1992, pp. 202-207.

[3.22] C. J. Mogab, "Dry etching", in *VLSI Technology* (Chapter 8), ed. S. M. Sze, McGraw-Hill, New York, 1983.

[3.23] J. P. Mc Vittie and C. Gonzales, "Anisotropic etching of Si using C_2ClF_5/SF_6", *Extended Abstracts Fall Meeting Electrochem. Soc.*, vol. 84-2, pp. 584-585.

[3.24] M. A. Schmidt, R. T. Howe, S. D. Senturia, and J. H. Haritonidis, "Surface micromachining of polyimide/metal composites for a shear-stress sensor", in *Tech. Dig. IEEE Micro Robots and Teleoperators Workshop*, Nov. 1987.

[3.25] L. J. Hornbeck, "Deformable-mirror spatial light modulators" in *Proc. Soc. Photo-Opt. Instrum. Eng.*, vol. 1150 (1989), pp. 86-102.

[3.26] J. A. van Raalte, "A new Schlieren light valve for television projection", *Appl. Opt.*, vol. 9 (1970), pp. 2225-2230.

[3.27] M. A. Cadman, A. Perret, F. Porret, R. Vuilleumier, and P. Weiss, "New micromechanical display using thin metal films", *IEEE Electron Device Letters*, vol. 4, no. 1 (1983).

[3.28] V. P. Jaecklin, C. Linder, J. Brugger, N. F. de Rooij, J.-M. Moret, and R. Vuilleumier, "Mechanical and optical properties of surface micromachined torsional mirrors in silicon, polysilicon, and aluminum", in *Tech. Dig. 7th International Conference on Solid-State Sensors and Actuators*, Yokohama, Japan, June 1993, pp. 958-961.

[3.29] U. R. Evans, *The Corrosion and Oxidation of Metals: Scientific Principles and Practical Applications*, Chapt. 5, St. Martin's Press, New York, 1960.

[3.30] J. J. Gajda, "Techniques in failure analysis of MOS devices", *Annu. Proc. Reliab. Phys.*, 12th, 1974, pp. 30-37.

[3.31] J. Y. Tsao and D. J. Ehrlich, "Laser-controlled wet chemical etching for corrective trimming of thin films", *J. Electrochem. Soc.*, vol. 133, no. 11 (1986), pp. 2244-2248.

[3.32] Y. B. Gianchandani and K. Najafi, "A bulk silicon dissolved wafer process for microelectromechanical devices", *J. Microelectromech. Syst.*, vol. 1, no. 2 (1992), pp. 77-85.

[3.33] K. Petersen, D. Gee, F. Pourahmadi, R. Craddock, J. Brown, L. Christel, "Surface micromachined structures fabricated with silicon fusion bonding", in *Tech. Dig. 6th International Conference on Solid-State Sensors and Actuators*, San Francisco, CA, USA, June 1993, pp. 397-399.

[3.34] B. Diem, M. T. Delaye, F. Michel, S. Renard, and G. Delapierre, "SOI (SIMOX) as a substrate for surface micromachining of single crystalline silicon sensors and actuators", in *Tech. Dig. 7th International Conference on Solid-State Sensors and Actuators*, Yokohama, Japan, June 1993, pp. 233-236.

[3.35] T. Nakamura, "Semiconductor device", *US Patent 3 288 656* (Nov. 29. 1966).

[3.36] J. B. Lasky, "Wafer bonding and its application to silicon-on-insulator technologies", *Appl. Phys. Lett.*, vol. 48, no. 1 (1986), pp. 78-80.

[3.37] P. W. Barth, "Silicon fusion bonding for fabrication of sensors, actuators and microstructures", *Sensors and Actuators*, vol. A21-A23 (1990), pp. 919-926.

[3.38] L. A. Christel, K. Petersen, "A catheter pressure sensor with side vent using multiple silicon fusion bonding", in *Tech. Dig. 7th International Conference on Solid-State Sensors and Actuators*, Yokohama, Japan, June 1993, pp. 620-623.

[3.39] C. Harendt, B. Höfflinger, H. Graf, E. Penteker, "Silicon direct bonding for sensor applications: characterization of the bond quality", *Sensors and Actuators*, vol. A25-27 (1991), pp. 87-92.

[3.40] J. Brugger, V. P. Jaecklin, C. Linder, N. Blanc, and N. F. de Rooij, "High-precision aligned silicon wafer bonding for a micromachined AFM sensor", *Tech. Dig. 2nd Int. Symp. Semicond. Wafer Bonding*, Honolulu, Hawaii, USA, May 1993.

[3.41] J. Brugger, R. A. Buser, N. F. de Rooij, "Silicon cantilevers and tips for scanning force microscopy", *Sensors and Actuators*, vol. A34 (1992), pp. 193-200.

[3.42] J. Brugger, V. P. Jaecklin, C. Linder, N. Blanc, P.-F. Indermühle, and N. F. de Rooij, "Microfabricated tools for nanoscience", in *Tech. Dig. 4th Workshop on Micromachining, Micromechanics and Microsystems*, Neuchâtel, Switzerland, September, 1993, pp. 105-114.

Testing of Devices

Actuators have at least one moving part, which is designed to perform a controlled displacement. Therefore, testing includes always the measurement of a displacement in function of different input parameters such as applied voltage or frequency of actuation. In general, traditional methods can be used for characterizing microactuators. Very often, static or quasistatic displacements are measured with the help of a light microscope, a scanning electron microscope (SEM), or a confocal microscope. However, these methods have their limitations in resolution. Hence, for nanometric displacements other techniques, as for example interferometry [e.g., 4.1], have to be employed. For angular displacements, optical-beam deflection [e.g., 4.2] has been successfully utilized. Another approach is to integrate a micromachined position sensor with the actuator as proposed for example for a scanning probe cantilever with electrostatic actuation and capacitive position detection [4.3] or for a comb drive with an integrated lateral tunneling sensor [4.4].

For high frequency actuation, testing can be done using a stroboscope [e.g., 4.5], a confocal microscope [e.g., 4.6], or an interferometer [e.g., 4.7]. The interferometer allows in the dynamic mode to perform measurements with subnanometre resolution.

In this chapter, three different types of actuators will be investigated by employing some of the measuring techniques mentioned above. Chapter 4.1 presents the performance of comb actuators and sarcomere actuators (several comb actuators in parallel). In view of a one-dimensional positioner, the displacement versus voltage behavior will be explained; further, levitation and side sticking effects will be discussed. In Chapter 4.2, these actuators will be used as driving elements for an *xy*-nanopositioner. The integration of a tip on the center stage allows to construct a complete scanning force system. Chapter 4.3 presents three different optical devices, namely, an optical microshutter, which allows to interrupt a laser beam; a pivoting micromirror, which can deviate a focused laser beam; and interference light modulators, which change a phase step or the width of an optical resonance cavity.

4.1 Comb Actuators

Different laterally movable actuators have been presented such as a large displacement actuator by *Brennen et al.* [4.8], an electrostatic parallelogram actuator by *Takeshima et al.* [4.9], and a linear stepper actuator by *Suzuki and Tanigawa* [4.10]. But no other device has had the same impact as the comb actuator proposed by *Tang et al.* [4.5]. The controlled lateral displacements and the rather large amplitudes (about 10 μm) are making it the favorite electrostatic linear microactuator. Based on this actuator, new devices have been realized such as a microgripper presented by *Kim et al.* [4.11]. These structures depend on the performance characteristics of the single comb actuator. Therefore, detailed studies of the actuator performance have been undertaken; especially, the influence of the suspension beam length has been investigated by *Tang et al.* [4.5], the importance of a small gap width has been discussed by *Hirano et al.* [4.12], and the actuator performance dependence on the profile of the suspension has been reported by *Judy and Howe* [4.13].

Section 4.1.1 focuses on the influence of suspension beam length and width. It turns out that long beams of submicrometer width allow for low driving voltages [4.14, 4.15]. Further, the resonance behavior of a comb actuator is investigated. A way to improve the comb actuator performance is presented in Section 4.1.2. It consists in increasing the driving force at a given voltage. This has been achieved with a sarcomere actuator, where - like in a muscle cell - several comb actuators are placed in parallel. This concept allows for a compact and powerful driving unit. Section 4.1.3 reports on experimental investigations of electrostatic levitation; the results are compared with the theoretical computations of Section 2.1.4. Finally, in Section 4.1.4, the sticking caused by electrostatic actuation will be considered, and experimental testing will be compared with the theoretical conclusions drawn in Section 2.2.2.

4.1.1 Normal comb actuators

A typical comb actuator, fabricated in our laboratories, is shown in Figure 4.1. As can be seen from the SEM photograph, the actuator consists of two electrodes, the fixed electrode and the movable electrode. The functional components of the actuator are the suspension, which gives a mechanical guidance for the actuator movement, and the comb, where the force for the actuation is created. The shown comb actuator has 200 µm long, 0.4 µm wide and 2 µm high suspension beams. The gap between the fingers is 3.2 µm. With a microprober needle the actuator can be moved up to 15 µm mechanically. Even after intensive operation, the movable part of the actuator returns to its initial position; hence, the submicrometer polysilicon suspension meets the basic elasticity requirement for repeatable, precise positioning.

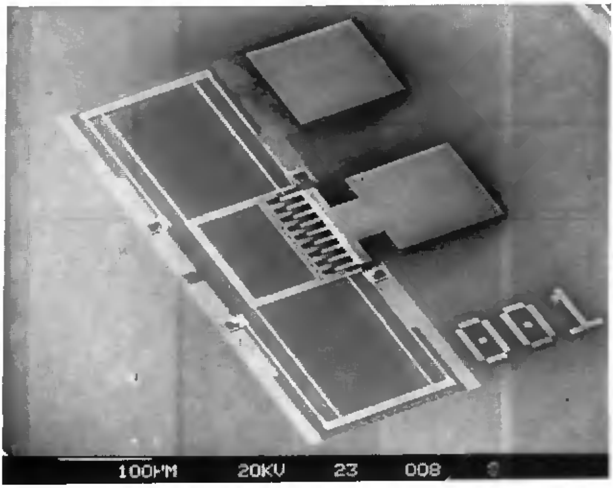

Fig. 4.1 SEM micrograph showing a low voltage comb actuator. The movable electrode (on the left side) is suspended by folded 200 µm long and 0.4 µm wide beams.

For electrostatic actuation, a voltage is applied on the fixed electrode, while the movable electrode and the ground plate underneath are on ground potential. The movable electrode will be displaced in the x-direction. As follows from Equations 2.13 and 2.29, the displacement x can be written as

$$x = n\varepsilon_0 V^2 \frac{L_1{}^3 + L_2{}^3}{4gEw^3} \tag{4.1}$$

where n is the number of fingers, ε_0 is the free space permittivity, E is the Young's modulus, assumed to be 170 GPa for polysilicon, L_1 is the length of the longer beams, L_2 is the length of the 20 μm shorter beams, and w is the width of the suspension. A displacement versus voltage curve is shown in Figure 4.2. While the points are the measured displacements, the curve is the best parabolic fit. The error of the displacement measurements using the light microscope is assumed to be ± 0.5 μm. The figure shows clearly that the displacement is a square function of the voltage as predicted by Equation 4.1. In particular, a 7.3 μm displacement has been observed for 14.5 V.

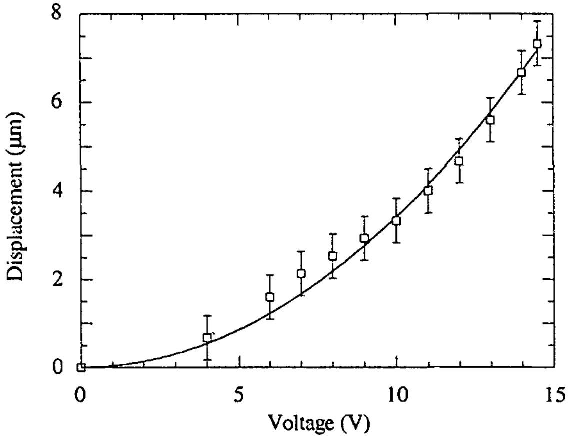

Fig. 4.2 Low voltage actuator: the diagram shows the displacement of 17 finger actuator with 300 μm long beams at various applied voltages. The solid line is the best parabolic fit to the data points.

The low driving voltage is mainly a result of the very flexible suspensions. The flexibility has been achieved by the submicrometer width (0.4 μm) of the suspension beams on the one hand and by the length (up to 300 μm) of the suspension on the other hand. Width and length have been optimized because they are the two cubic terms of Equation 4.1. The influence of the beam length can be seen in Figure 4.3, where comb actuators with identical driving unit (9 finger comb) but different suspension beam length are compared. In particular, a 150 μm long suspension allows a displacement of the comb of 0.6 μm for 10 V while the comb suspended on 300 μm long suspension beams will be moved 3.3 μm for the same voltage. In Table 4.1, the measured and the calculated slopes of displacement versus voltage squared characteristics are compared. The discrepancy between the actual and predicted slopes is probably due to variations in suspension beam width and gap distance. The highest measured slope is 36.1 nm/V^2; this is about 24 % higher than the best values reported by *Hirano et al.* for submicrometer gap comb actuators [4.12].

The comb actuators have also been operated in a resonant mode. This method is particularly useful to move actuators with a rigid suspension. For example, in the first fabrication run, the width of the comb actuator suspension was 2.8 µm, making the suspension to rigid for linear displacements.

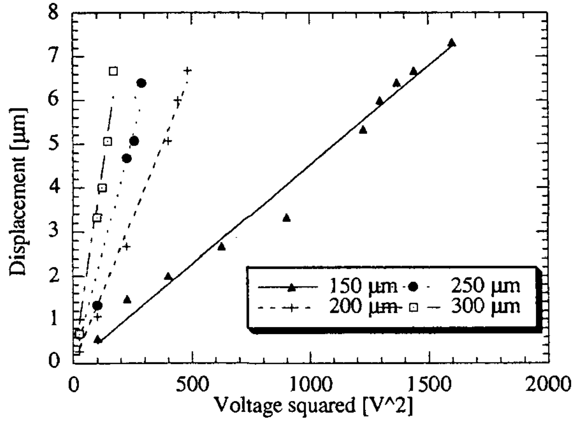

Fig. 4.3 Comparison of actuators with identical 9 finger comb but different suspension beam lengths. The straight lines are the best linear fits for the given sets of data points.

Beam Length [µm]	Measured Slope [nm/V^2]	Calculated Slope [nm/V^2]
150	4.5	3.2
200	13.3	7.9
250	20.7	15.8
300	36.1	27.9

Table 4.1 For four different beam lengths, the calculated and measured displacement characteristics are compared.

Therefore, the resonance behavior has been investigated as shown in Figure 4.4. A DC voltage of 180 V is applied on the stator electrode, and an AC voltage of ±15 V is superposed. A maximum amplitude of 15.2 µm has been observed by visual inspection using a light microscope. While the resonance frequency can be determined using the formulae explained in Section 2.2.2, it is helpful to have a mathematical expression for the mechanical damping. We will use the quality factor Q - it is defined as

$$Q := 2\pi\frac{\text{maximum energy stored in one period}}{\text{dissipated energy per period}} \tag{4.2}$$

Low energy losses imply a high Q. The quality factor cannot be determined directly but can be deduced from the response characteristics. A common method to obtain Q from a frequency response like Figure 4.4 is given by the following equation [4.16]

$$Q = \frac{f_{res}}{\Delta f_{\text{-3dB}}} \qquad \text{for } Q \gg 1 \tag{4.3}$$

where f_{res} is the resonant frequency, and $\Delta f_{\text{-3dB}}$ is the half power bandwidth

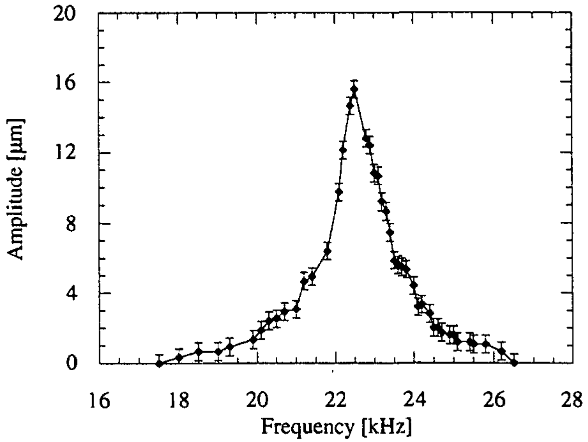

Fig. 4.4 Resonance behavior of comb actuator having 200 µm long, 2 µm high, and 2.8 µm wide suspension beams. A DC voltage of 180 V is applied and an AC voltage of ±15 V is superposed. The resonance frequency is 22.5 kHz, and the quality factor is 25.

of the frequency response. Equation 4.3 indicates that Q is a measure for the sharpness or in other words for the selectivity of the frequency response. Using this equation, a quality factor Q of 25 can be deduced from Figure 4.4; the measured resonance frequency is 22.5 kHz. As proposed by *Schmidt et al.* [4.17], for such a structure the damping is dominated by the Couette flow underneath the moving structure. As will be seen later, the quality factors for lateral displacement are considerably higher than for vertical displacements, where the resonance behavior is dominated by the squeeze film damping.

4.1.2 Sarcomere actuators

To increase the force per voltage squared, we propose a novel actuator, where several comb structures are placed in parallel - like in a muscle fibril (sarcomere); therefore, we call it sarcomere actuator [4.18]. As illustrated in Figures 4.5 and 4.6, the three fixed combs are electrically connected with the first thin polysilicon; the interconnection passes below the suspended structure. The driving force of such a sarcomere actuator is increased by almost a factor of three. This can be seen in Figure 4.7, where the displacement versus voltage squared diagram is shown for a normal comb actuator and a sarcomere actuator with three combs in parallel; both actuators have the identical suspension (200 μm long beams). Because the normal comb actuator has 18 partly overlapping surfaces and the sarcomere actuator has 50, the slope of the sarcomere actuator curve is expected to be a factor of 2.78 (4.39 nm/V^2) higher than the slope of the normal comb actuator. The measured factor is 2.60 (4.10 pN/V^2). This difference may be caused by the uncertainty of the precise geometric dimensions as well as by electrostatic effects that we ignored for simplicity. In particular, the stator comb in the middle of the moving electrode (cf. Figure 4.6) is contributing to additional fields, which are lowering the effective driving force.

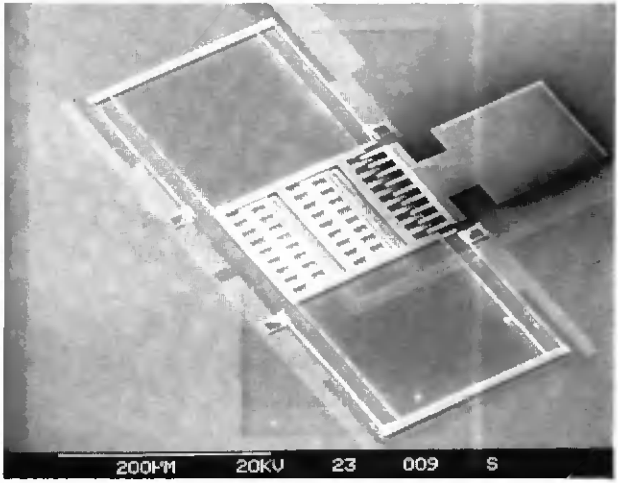

Fig. 4.5 SEM micrograph showing a sarcomere actuator - like in muscle fibril several comb actuators are placed in parallel.

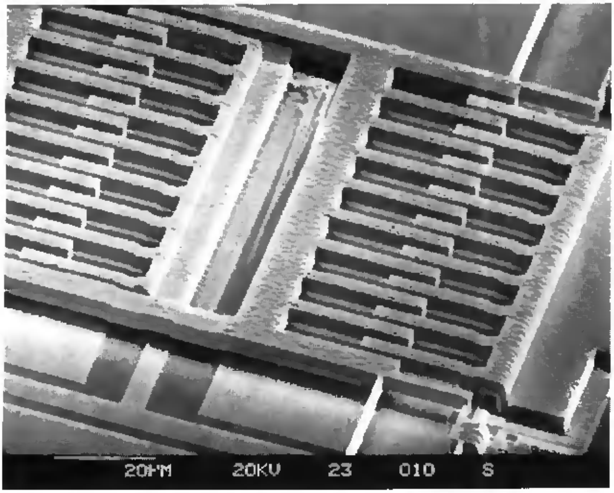

Fig. 4.6 SEM micrograph displaying the compact and powerful driving unit of a sarcomere actuator.

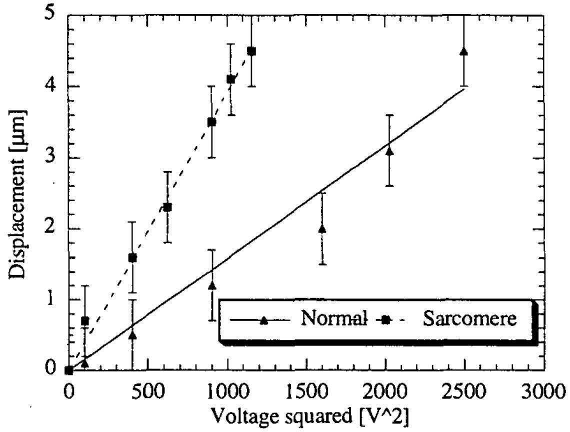

Fig. 4.7 In the diagram the performance characteristics of a normal comb actuator and a sarcomere actuator with identical suspension are compared. The straight lines are the best linear fits of the given stets of data points. The slope of the sarcomere actuator curve is a factor of 2.60 steeper than that of the normal comb actuator.

4.1.3 Levitation phenomenon

As described in Section 2.1.4, the electrostatic levitation of the movable electrode is caused by the nonsymmetric fringing fields surrounding the planar electrode. The levitation effect has been observed in the SEM. Figure 4.8 shows that by applying a voltage, the movable comb is levitated and at the same time displaced in the direction of the fingers. Quantitative investigations have been performed in the SEM as well as with the help of a confocal microscope. The measured displacements, observed with the SEM, are shown in Figure 4.9; the measurement error is assumed to be ± 0.1 µm. In agreement with the results reported by *Tang et al.* [4.19], the vertical displacement is almost a linear function of the applied voltage. However, at higher voltages, for the tested structure above 60 V, the equilibrium position is attained, and no further vertical displacement will occur. The measurements indicate a maximum levitation of 1.25 µm. This is in good agreement with the simulation of Section 2.1.4, which predict an equilibrium position at 1.2 µm above the fixed electrode.

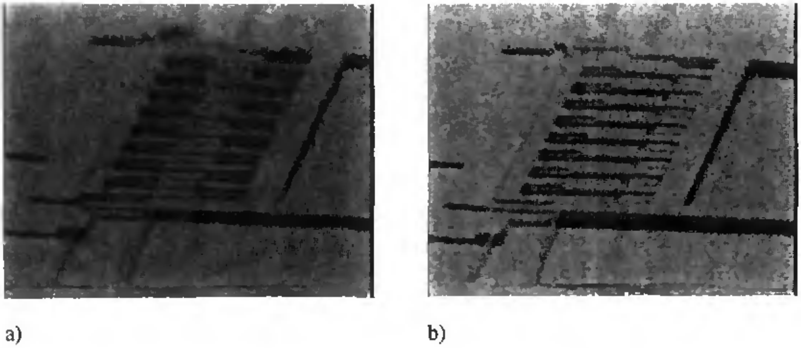
a)

b)

Fig. 4.8 Observation of the electrostatic levitation of the movable comb in the SEM. **a)** no voltage is applied - the fixed and the movable comb are at the same level; **b)** 60 V are applied - the movable comb is levitated and at the same time displaced in the direction of the fingers.

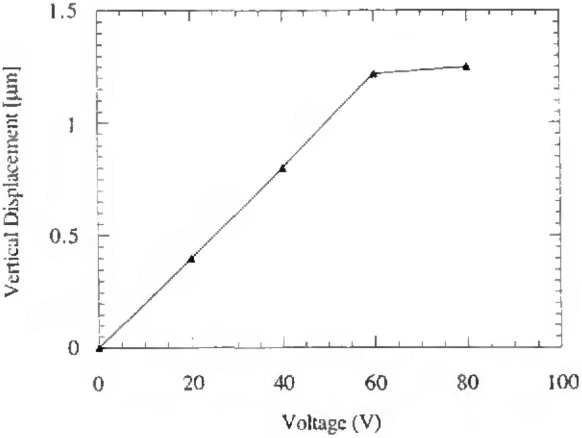

Fig. 4.9 The measured electrostatic levitation of a comb actuator as a function of the applied voltage.

4.1.4 Sticking caused by electrostatic actuation

The working range of the comb actuators may be limited if the design does not take into account several effects. One category of effects consists of sticking caused by the electrostatic actuation: if two electrodes which are not on the same potential are mechanically touching each other during operation, they stick together and very often remain stuck even when the potential is removed. This permanent sticking is believed to be caused by soldering during the charge exchange of the the two electrodes [4.20]. Depending on the design of the actuator, the movable comb will, at a critical voltage, either stick on the sides of the fixed fingers (side-sticking) or on the front ends of the fixed finger (front-sticking). As discussed in Section 2.1.3, the movable comb is in an inherently unstable position. Therefore, the movable comb has to be guided by the mechanical suspension. For side-sticking to occur, as proposed by *Hirano et al.* [4.12], a critical spring constant k_{cr} can be expressed based on the derivative of the force F_y given by Equation 2.18

$$k_{cr} = \left.\frac{\partial F_y}{\partial y}\right|_{y=0} = \frac{2n\varepsilon_0 tlV^2}{g^3} \tag{4.4}$$

As can be deduced from the equation, the sticking is dominated by the inverse of the cube of the gap while the driving force is proportional to the inverse of the square of the gap. In other words, a small gap increases the driving force but limits the actuation range. Therefore, very small gaps may not be optimal for a 'well-behaved' comb actuator performance. This is the reason why we tried to improve the performance mainly by lowering the width of the suspension beams.

By taking the geometric dimensions of real structures (not the standard dimensions) and the experimental values for the critical voltage V where sticking occurs, k_{cr} can be calculated. For the actuator shown in Figure 4.10, the critical spring constant is $k_{cr} = 1.45$ N/m. This value can be compared with the simulated spring constant, $k_y = 1.29$ N/m. Hence, the two spring constants are almost equal. By setting $k_{cr} = k_y$, we can predict at what voltage side-sticking should occur. Experimental and calculated values for side sticking are listed in Table 4.2.

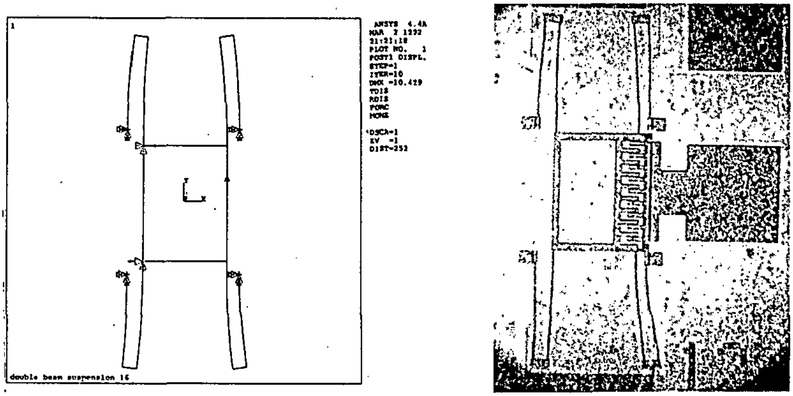

Fig. 4.10 Side sticking phenomenon. For a particular structure, the ANSYS simulation (left illustration) and the real event (right illustration) are compared. The suspension beams are 150 μm long.

Beam length [μm]	Sticking Voltage Calculated [V]	Sticking Voltage Measured [V]
150	27	26
200	23	21
250	20	16
300	17	13

Table 4.2 Calculated and measured sticking voltages are compared for different suspension dimensions.

In order to investigate the front sticking phenomena, let F_t be the sum of the comb drive force F (Equation 2.13) and of the force F_p, due to the parallel capacitor plates formed by the front ends of the comb fingers (Equation 2.19). This driving force has to be compensated by the restoring force of the spring F_x, which is given by the Hooke's law. For a stable equilibrium position, two conditions have to be fulfilled. First, the total driving force F_t has to be equal to the restoring force of the spring F_x and second, the derivative of the driving force has to be smaller than the derivative of the spring force

$$\frac{\partial F_t}{\partial x} < \frac{\partial F_x}{\partial x} \tag{4.5}$$

The two conditions allow to calculate for a given structure the maximum displacement x_{max} before sticking occurs. The equation for x_{max} is a third order polynomial with the following variables: finger width w, gap g, and initial distance d. For the geometry of the structure shown in Figure 4.11, the calculated maximum displacement is $x_{max} = 9.5$ μm. In the experiments, a maximum displacement of $x = 7.3$ μm can be measured. The structure will front-stick at a voltage of 23 V.

The reason why no side-sticking occurs can be seen if the spring constants k_y and k_{cr} are compared. k_y is 0.93 N/m and k_{cr} is 0.19 N/m (for 23 V). Hence, k_y is bigger than k_{cr}, and therefore, no side-sticking takes place.

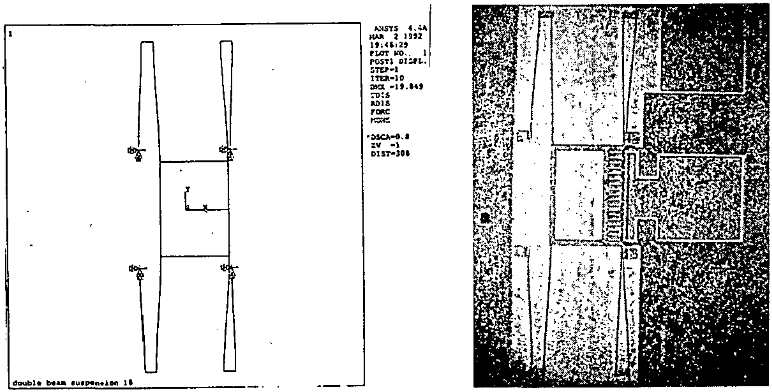

Fig. 4.11 Front-sticking phenomenon. For a particular structure, the ANSYS simulation (left illustration) and the real event (right illustration) are compared. The long suspension beams are 200 μm long.

4.2 *XY*-Nanopositioners

Precise two-dimensional positioning is an important technological field. High positioning performance is necessary for the machining and processing of semiconductors, optoelectronic elements, and high density magnetic storage devices. Scanning tunneling microscope (STM) and scanning force microscope (SFM) are further examples, where very high positioning control is needed.

Servo motors and piezoelectric drives are two methods frequently used for achieving the required precision [4.21]. Micromachined electrostatically driven devices may be an interesting alternative. We propose a two-dimensional microstage which is driven by the characterized comb actuators. Testing on the first prototypes showed that precise positioning is feasible.

The invention of the STM [4.22] and the SFM [4.23] has opened completely new opportunities for high resolution surface probing instruments for research and industrial purposes [e.g., 4.24]. In particular, the scanning drive of a microprobe unit is less sensitive to vibrations and thermal drift if it is miniaturized [4.23]. A micromachined piezoelectrically driven scanner realized by *Akamine et al.* followed this concept [4.25]. Recently, also capacitively driven micromachined scanners have been proposed [4.26, 4.27]. Its features are quick response time, IC-compatible driving voltages, little or no hysteresis in the positioning, and the feasibility of an integrated capacitive positioning detection.

Section 4.2.1 presents a nanopositioner fabricated in the polysilicon sacrificial layer technology. A more complex positioner with integrated tip for SFM applications is fabricated in single crystal silicon; its working principle is discussed in Section 4.2.2.

4.2.1 Polysilicon nanopositioners

A typical xy-nanopositioner that we fabricated is shown in Figure 4.12. The microstage consists of four comb actuators assembled around a center stage. The design of the microstage is based on a pull mechanism - the table is moved to any position in the xy-plane by energizing two of the four comb drives. The decoupling of the x- and y-position is given by the construction of the suspension. Figure 4.12 shows a complete view of the fabricated stage, and Figure 4.13 displays details of the free standing stage. The square table (8 μm by 8 μm) is suspended by four 270 μm long, 0.4 μm wide, and 2 μm high beams.

This prototype allows to displace the table in any direction in the xy-plane. Mechanically, a maximum surface of 30 μm by 30 μm can be covered. For the electrostatic actuation, a displacement versus voltage curve is shown in

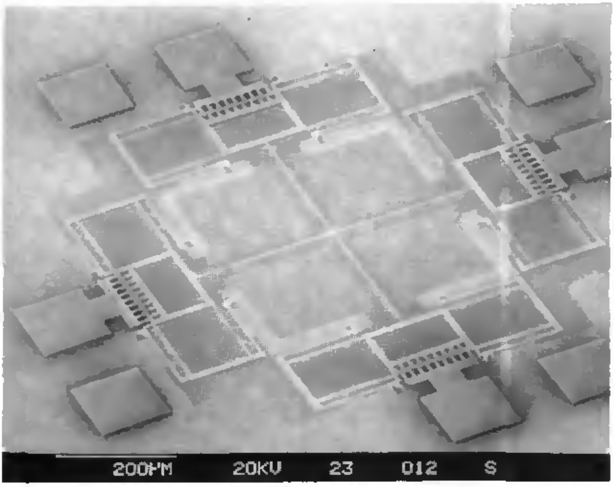

Fig. 4.12 SEM micrograph showing an *xy*-microstage. The center stage is suspended by four 270 μm long, 0.4 μm wide, and 2 μm high polysilicon beams.

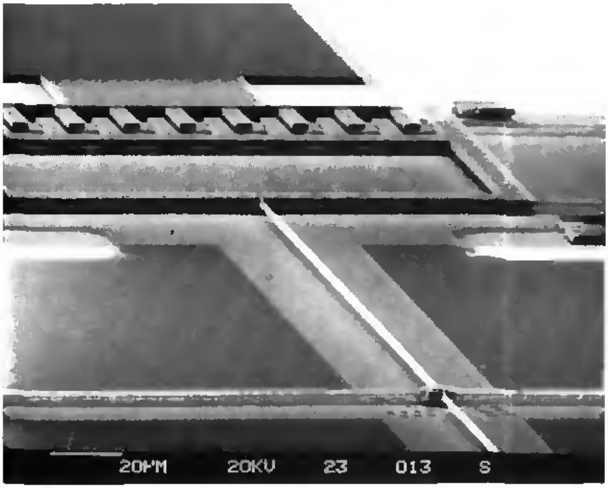

Fig. 4.13 SEM micrograph displaying the free-standing *xy*-microstage with a comb actuator in the background. The polysilicon stage has a surface of 8 μm by 8 μm and is suspended 2 μm above the substrate.

Figure 4.14. While the points are the measured displacements, the curve is the best square fit. In particular, a 5.3 μm displacement in x-direction has been observed if on the corresponding comb actuator a potential of 40 V is applied. Since the displacement characteristic has been investigated with the light microscope and the SEM, where the measurement resolution is limited to approximately ±0.1 μm, it can only be postulated that the positioning precision is better than the measurement accuracy. Because of these limitations, the temperature dependence of the displacement characteristics has not been investigated yet. There, the two major influences are assumed to be the thermal expansion of structure (for silicon, the linear coefficient of expansion is 2.6 ppm/°K at room temperature [4.28]), which will modify the created force as well as the flexibility of the suspension, and the temperature changes of the Young's modulus (for silicon, it is around -90 ppm/°K for all crystalline orientations [4.28]), which will alter the mechanical properties of the suspension. Based on these assumptions, it can be estimated that for the polysilicon comb actuators the total effect of temperature on the displacement-voltage characteristic is below 100 ppm/°K.

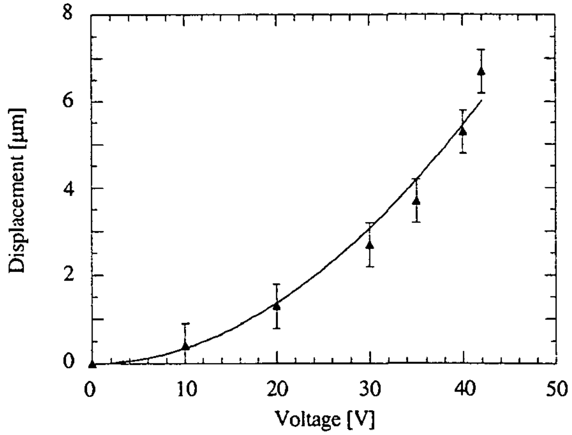

Fig. 4.14 Displacement versus voltage curve of a polysilicon xy-nanopositioner.

An interesting feature of these xy-manipulators is that the position sensing can be done by capacitive measurements. It is conceivable to use the capacitance changes of the comb actuators for the position measurements. Another possibility is shown in Figure 4.15; the changes in the capacitive coupling between the table and four ground plane pads may be used for the position detection [4.29].

In view of an application of the stage as a manipulator for an SFM tip, the resonance behavior is important. The sensitivity to vibrational noise from the building - around 100 Hz - has to be minimized [4.23]. For the stage of Figure 4.12, a resonance frequency in x-direction of 4.3 kHz has been observed while the amplitude was around 4 μm for the 30 V peak to peak sinusoidal signal. The resonance frequency in z-direction has not been measured yet; however, it is estimated to be also well above the frequencies of the vibrational noise.

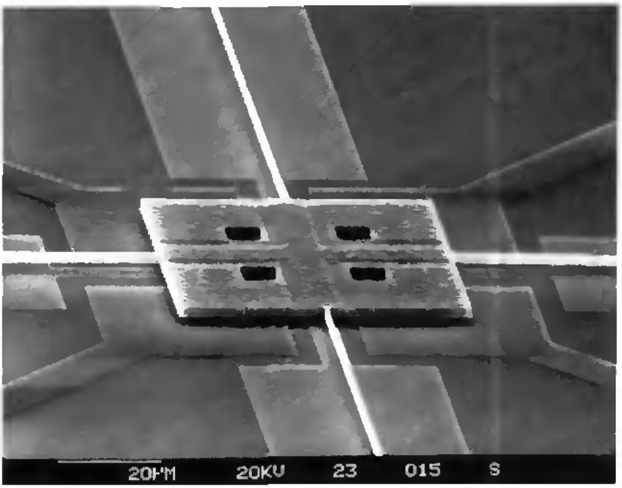

Fig. 4.15 SEM micrograph showing a 60 μm by 60 μm free-standing xy-microstage, which is suspended by four 320 μm long and 0.4 μm wide beams. The four polysilicon 1 pads below the stage may be used for capacitive positioning detection or for vertical actuation.

These rather complex and fragile looking devices could be constructed with submicrometer beams because, following the scaling laws, an increased inertial strength can be expected at small dimensions. For the large stage in Figure 4.15, a vertical deflection due to gravitation of 6.2 nm can be calculated.

4.2.2 Silicon scanning unit with integrated protruding tip

The key features of the integrated monocrystalline silicon microsystem are the following: the xy-nanopositioner, a sharp protruding tip for surface probing integrated on the microstage providing improved sample access, and a via hole through the wafer enabling optical measurement of the vertical tip

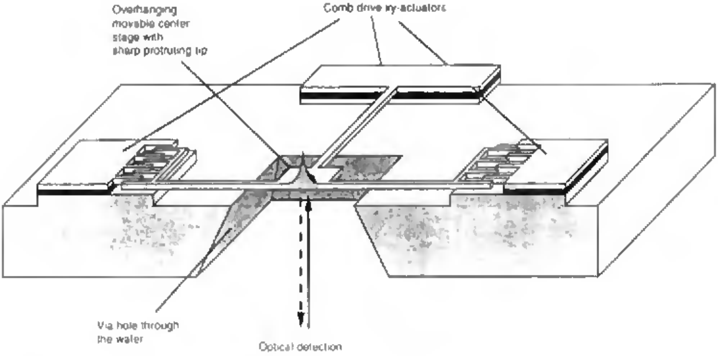

Fig. 4.16 Design and operation of a microsystem with overhanging xy-nanopositioner, integrated sharp protruding tip and optical position readout.

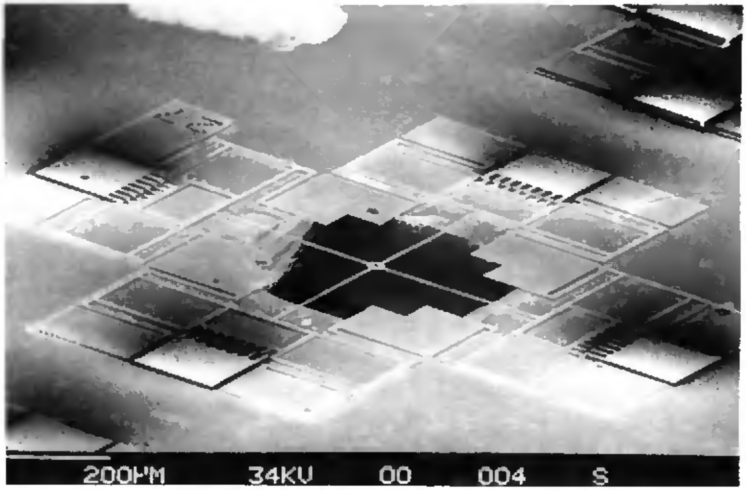

Fig. 4.17 SEM graph of a micromachined silicon xy-nanopositioner with via hole and protruding tip. The square shaped hole has a length of 480 μm.

position. A scheme of the complete device is shown in Figure 4.16. The via hole in the substrate underneath the positioner allows to focus a laser beam on the center stage for interferometric detection of the tip displacement in z-direction. With this detection mechanism subnanometre resolution is achieved [4.30]. A finished device is shown in Figure 4.17. Figure 4.18 gives a detailed view of the tip on the table; it is 8 μm high and the estimated tip radius is 40 nm.

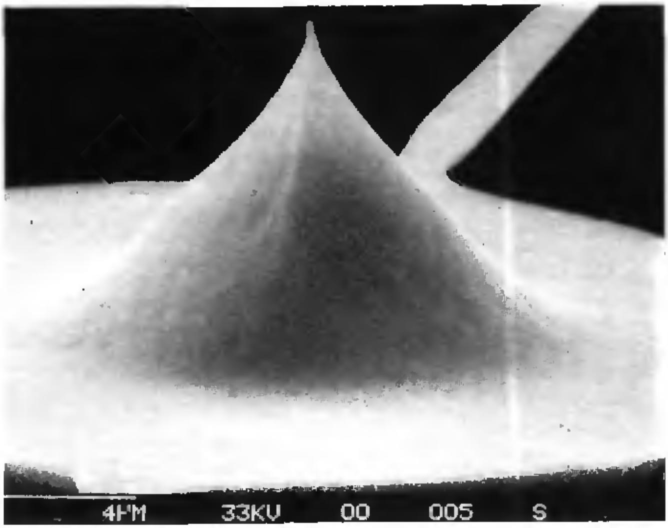

Fig. 4.18 Detailed view (SEM) of micromachined tip integrated on the scanning table. Its height is 8 μm and the tip radius is estimated to be 40 nm.

4.3 Light Modulators

Light modulators are used to alter the amplitude, the phase, or the polarization of light. There exists a multitude of macromechanical light modulators ranging from venetian blinds, over camera shutters, to highly sophisticated interferometers. Since the 1970s, electro-optics has added fast switching structures making use for example of the Pockels effect. Acousto-optical shutters have been devised, which employ the Bragg diffraction due to an acoustic wave. Further, very popular devices are based on the controlled transmissivity of liquid crystal. Finally, there is also the class of light modulators actuated by micromechanical structures.

Already in the late 1960s, high density arrays of micromachined phase shifters, addressed by an electron beam, have been proposed by *Preston* [4.31] and a few years later by *van Raalte* [4.32] and *Thomas et al.* [4.33]. In the late 1970s, *Petersen* has constructed electrostatically driven laser beam deflectors [4.34] and silicon scanning mirrors [4.35]. These pioneering devices have not been successful in commercial applications. Nevertheless, a lot of activity was going on in this domain, and it was in 1992 that Texas Instruments announced an airticket printer, which has an integrated micromechanical light modulator [4.36]. This product was based on the ongoing research and development of the company for over two decades [4.37-4.39]. Other recent research and development is further away from commercialization; it involves the realization of optical choppers [4.40, 4.41], Fabry-Perot interferometers [4.42-4.44], diffraction light modulators [4.45], scanning mirrors [4.46-4.48], optical shutters [4.49], and optical switches [4.50]. A lot of research activities are directed towards telecommunication. In particular, optical crossbar switches for interconnection networks are of interest. Recently, micromachined spatial light modulators have been proposed for this purpose [4.51-4.53].

The development on light modulators reported in this work were triggered by earlier activities of the Swiss Center for Electronics and Microtechnology Inc. (CSEM) for the fabrication of an array of shutters [4.54, 4.55]. In particular, results of comb-driven microshutters will be discussed in Section 4.3.1. On the performance of torsional micromirrors will be reported in Section 4.3.2, and interference light modulators will be presented in Section 4.3.3.

4.3.1 Optical shutters

As shown in Figure 4.19, the optical microshutter is composed of a comb for creating the electrostatic force, a movable shutter (100 μm by 30 μm), and a compact meander folded beam suspension, for guiding the shutter in the actuation direction. The surface occupied by the new meander spring is drastically reduced (130 μm by 60 μm) as compared with that of earlier comb actuator suspensions (500 μm by 150 μm). This suspension, made of five double beam spring elements, has still a high stiffness in the direction transverse to the actuation.

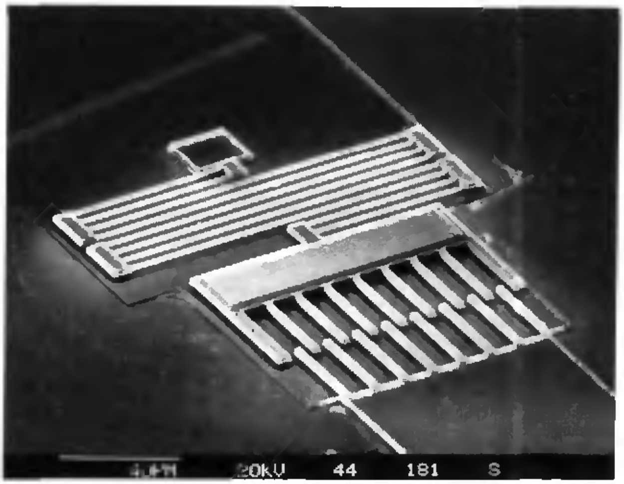

Fig. 4.19 Top view of an optical microshutter (SEM). The aluminized shutter surface is 90 µm by 25 µm.

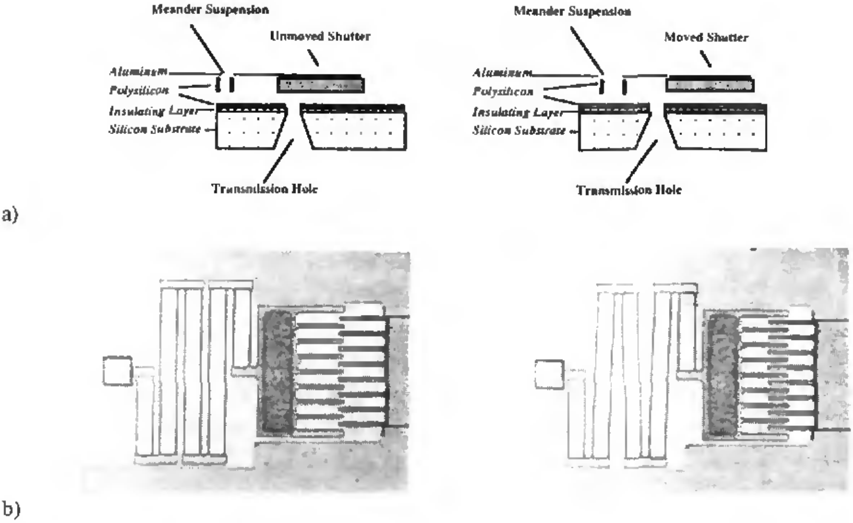

Fig. 4.20 Microshutters at rest and actuated positions: **a)** schematic drawings show cross sections - a transmission hole is closed or opened by the displacement of an aluminized shutter; **b)** optical micrographs show top views of the real device (a total displacement of 8 µm is achieved).

Figure 4.20 visualizes the two positions of the shutter. While Figure 4.20a displays schematic cross sections, in Figure 4.20b the optical micrographs show the real device. The displacement characteristic of the optical microshutter is given in Figure 4.21. As for the earlier comb actuators, the displacement is proportional to the square of the applied voltage. A maximum displacement of 8.3 μm is measured at 53 V; hence, this performance allows the modulation of a focused laser beam of 5 μm diameter. The device has a measured resonance frequency of 4.5 kHz.

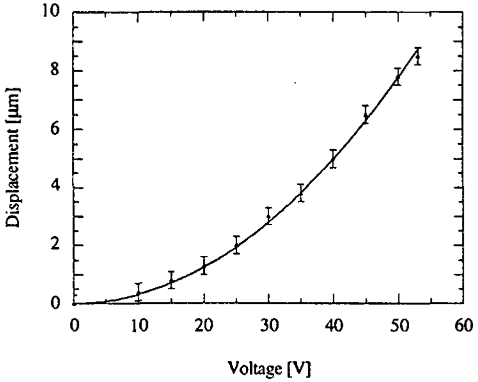

Fig. 4.21 Displacement versus voltage curve of the optical microshutter. Measurements have been performed on a light microscope.

The optical microshutter allows for two different operation modes. In the reflection mode, the light source and the photosensitive part are placed both in front of the shutter; the laser beam is either reflected by the aluminum film on top of the shutter plate (83% reflectivity - on condition) or, for the displaced shutter, the beam is mainly absorbed by the underlying substrate surface, which is less reflective (31% reflectivity - off condition). In the transmission mode, the shutter is placed between the light source and the photosensitive part. The closed state is given by the interruption of the laser beam - it is reflected on the shutter plate back to the light source. In the open state, i.e., for the displaced shutter, the beam can pass. A very high contrast ratio can be obtained with this operation principle. A close-up view of a transmission-mode microshutter, overhanging a 60 μm by 60 μm substrate via hole, is shown in Figure 4.23; it allows for interrupting a focused laser beam.

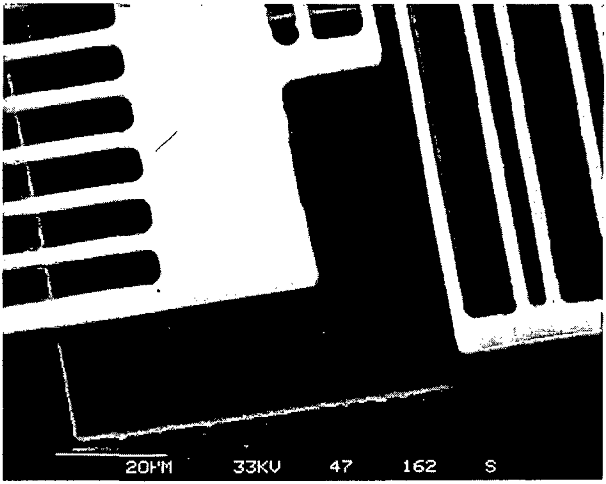

Fig. 4.23 Top view (SEM) showing details of the optical microshutter suspended over a KOH-etched 60 µm by 60 µm hole.

4.3.2 Pivoting mirrors

Figure 4.24 shows the function principle of a torsion micromirror. When a voltage higher than V_1 (switch voltage) is applied on the address electrode, the electrically grounded mirror rotates by an angle of 7.6° and hits the landing electrode. The latter is also electrically grounded for avoiding charge sticking effects. For the mirror to return to its initial position, the address voltage is reduced below V_2 (release voltage). Therefore, the system is bistable - by choosing an appropriate hold and address voltage, mirrors can be addressed individually in a two-dimensional array. A fabricated torsional micromirror of 30 µm by 30 µm, suspended by 10 µm long and 0.4 µm wide beams, is displayed in Figure 4.25. The SEM picture shows clearly the address electrode and the landing electrode below the mirror.

The displacement and switching characteristics have been observed with the confocal optical length measurement system, UBM Microfocus. The torsion angle of a micromirror, with the identical geometric dimensions as used for the calculations, is shown in function of the applied voltage in Figure 4.26.

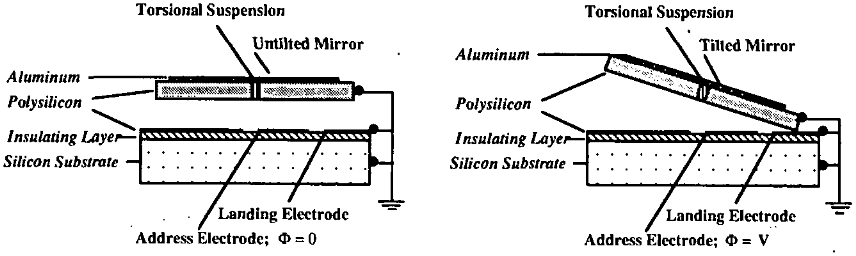

Fig. 4.24 Cross sections of rest (left illustration) and tilted position (right illustration). In the tilted position the mirror is touching a landing electrode, which is at the same potential as the mirror.

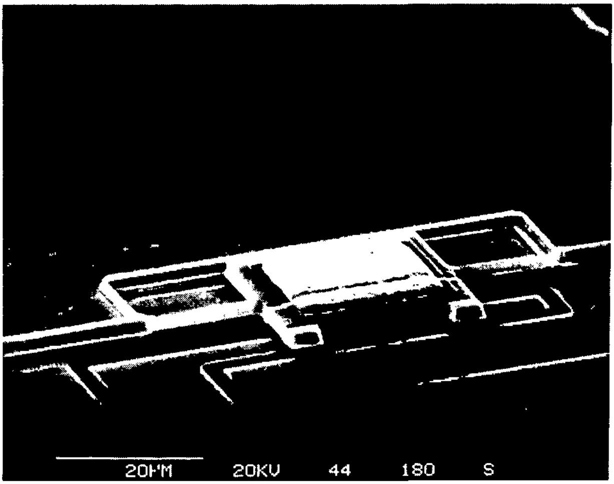

Fig. 4.25 Top view (SEM) of pivoting micromirror. The aluminized mirror surface is 26 µm by 26 µm, and the mirror is suspended 2 µm above the substrate.

The error of the measurements with the confocal microscope is ± 50 nm, which corresponds to an uncertainty of the angular resolution of ± 0.13°. As predicted by the theoretical considerations, the tilted angle is initially nearly a square function of the applied voltage. The constant angle per voltage squared of $25.2 \cdot 10^{-6}\,\mathrm{rad/V^2}$ can be deduced from the measurements (computations in Section 2.3.3 have resulted in a constant of $24.5 \cdot 10^{-6}\,\mathrm{rad/V^2}$). Abrupt tilting takes place in agreement with theory, which predicts the occuring of the instability after roughly one third of the total displacement. The exact critical displacement depends on the geometry of the design [4.38]. The measured switching voltage V_1 is 31 V. If afterwards the voltage is lowered, the mirror stays tilted until the release voltage V_2 of 16 V is reached. Once the mirror is released, the displacement follows the same characteristic as in the attraction cycle. In Figure 4.27, the threshold voltages V_1 and V_2 are plotted versus the beam length of the suspensions.

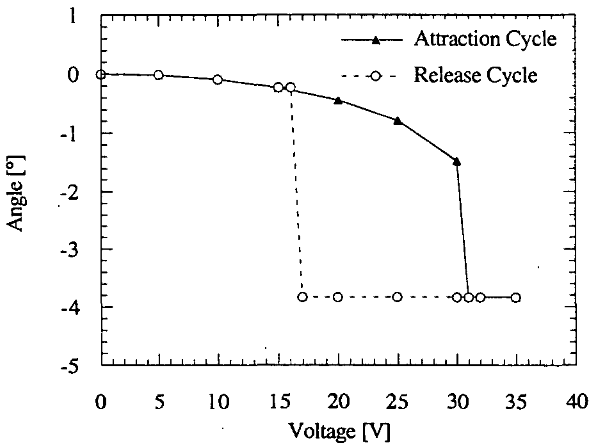

Fig. 4.26 Displacement characteristic of torsional micromirror (torsion beams fixed near the mirror edge). The threshold voltage of abrupt position change is denoted V_1 (31 V) in the attraction cycle and V_2 (16 V) in the release cycle.

If the applied voltage is abruptly switched from V_1 to 0 V, the mirror will come back to its initial position (cf. Figure 4.28); but because the system is under critically damped, some oscillations will occur until the mirror is at rest. After 100 µs, V_1 is applied again and the mirror will be tilted. Because the mirror hits the landing electrode, no oscillations are observed. This behavior has been studied with the help of the confocal microscope. As shown in Figure 4.28, the resonance frequency is approximately 100 kHz, and the 1/e amplitude is reached after roughly 29 µs. If this time constant of damping is named τ_d, the following equation can be written [4.16]

$$Q = \frac{f_1 \tau_d}{2} \tag{4.6}$$

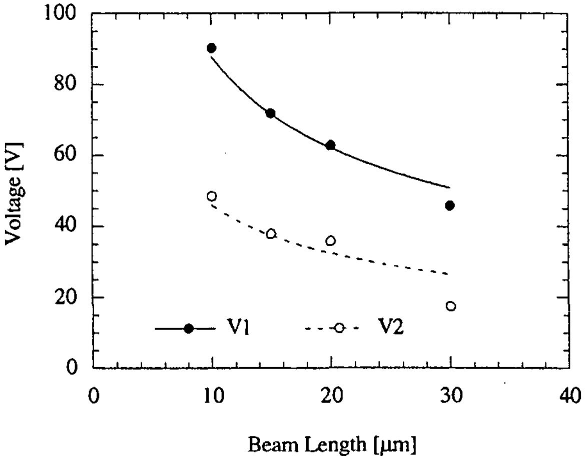

Fig. 4.27 Switching characteristics of 30 μm by 30 μm pivoting micromirrors having various beam lengths; the torsion bars are fixed on the middle of the mirror edge. The lines are the best fits proportional to $1/\sqrt{l}$, where l is the length of the suspension beam.

Hence, the calculated quality factor is about 1.5. The bandwidth of forced vibrations of a mechanical structure is simply related to the resonant frequency f_{res} and the quality factor. Since the quality factor is rather low, i.e., the damping is important, it must be clearly distinguished between the resonant frequency f_{res} and the natural frequency f_1. Following the theory of vibrations, the amplitude $A(f)$ of a forced vibration at a certain frequency f is given by [4.56]

$$A(f) = A(0)\frac{1}{\sqrt{\left(1 - \left(\frac{f}{f_1}\right)^2\right)^2 + \left(\frac{f}{Qf_1}\right)^2}} \tag{4.7}$$

where $A(0)$ is the amplitude of static displacement and f_1 is the natural frequency of the system. The resonance frequency of a damped system can be obtained from the natural frequency with the following relation

$$f_{res} = f_1\left(1 - \frac{1}{2}Q^{-2}\right)^{1/2} \tag{4.8}$$

Therefore, if the quality factor and the resonance frequency of a system are given, the bandwidth of operation can be determined.

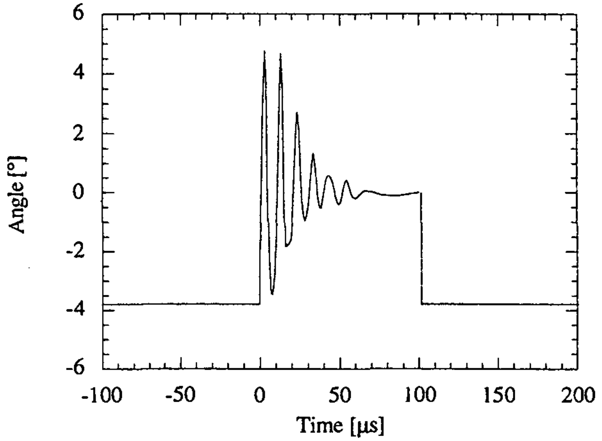

Fig. 4.28 Switching characteristics of pivoting micromirror. If the mirror is released from its tilted position, a number of oscillations are observed until it reaches its stable zero position.

In order to establish the resonance frequency precisely, a transfer curve of the pivoting mirror has been measured; it is given in Figure 4.29. This has been done by exciting the mirror electrostatically to small amplitudes in the range of a few nanometers. The data are collected and analyzed using a confocal microscope and a lock-in amplifier. The measured resonance frequency is 97 kHz. For these small oscillations, a quality factor of 4.8 can be deduced from the shape of the resonance curve (Equation 4.3). This factor is more than three times higher than the one established by the observation of the ringing oscillations. The difference is believed to be due to the much smaller amplitudes (3 orders of magnitude smaller), where the medium gap is larger and therefore the damping is less dominated by the squeeze film damping. As predicted by a model developed by *Newell*, the quality factor Q of such a setup is proportional to the cube of the gap width [4.57]. For determining the bandwidth of operation, the quality factor Q of 1.5 is taken; then the 1.5-dB bandwidth of the pivoting micromirror is 1.7 times larger than the resonance frequency. Hence, for the structure under investigation a 1.5-dB bandwidth of operation of 165 kHz can be established.

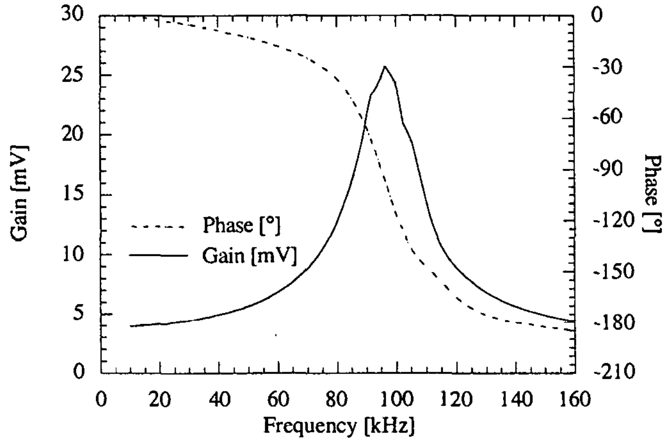

Fig. 4.29 Transfer function of torsional micromirror. From these measurements, a resonance frequency of 97 kHz and a quality factor of 4.8 can be deduced.

Based on the encouraging results of the single torsional mirrors, two-dimensional arrays have been constructed. A two-dimensional rectangular grid of electrodes is formed which allows, by properly choosing the voltages, to address every single mirror individually. Figure 4.30 shows two mirrors in the center of an array, and Figure 4.31 displays a corner of the 32 by 32 mirror array. The device is designed to allow simple wire bonding; hence, it is not optimized for a high filling factor which is only 11 %. The finished and packaged chip is presented in Figure 4.32; it is mounted on a pin-grid array with 124 pins (PGA 124). The reason to utilize a PGA 124 is the large size of the chip (12.5 mm by 12.5 mm) not the number of pins since only 64 pins are used. To protect the chip from dust, it is covered with a thin glass plate.

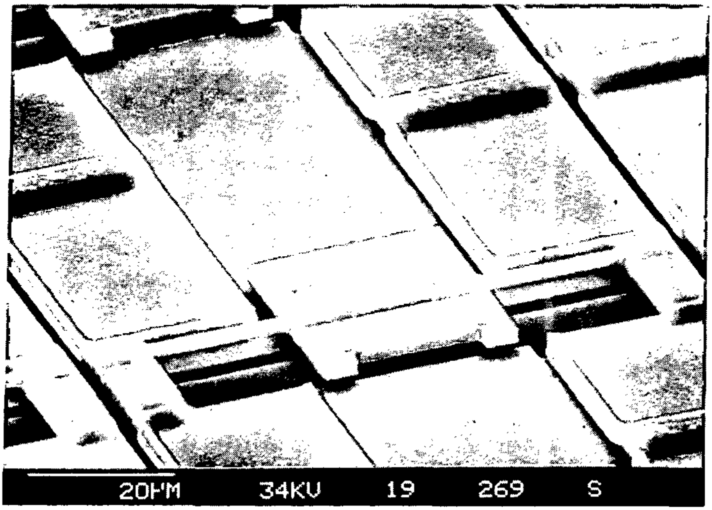

Fig. 4.30 Two-dimensional polysilicon mirror array - close view of two mirrors (SEM). The horizontal address electrodes (fabricated in the first thin polysilicon) passing below the suspended mirrors and the vertical mirror electrodes (fabricated in the second thick polysilicon) can be clearly distinguished.

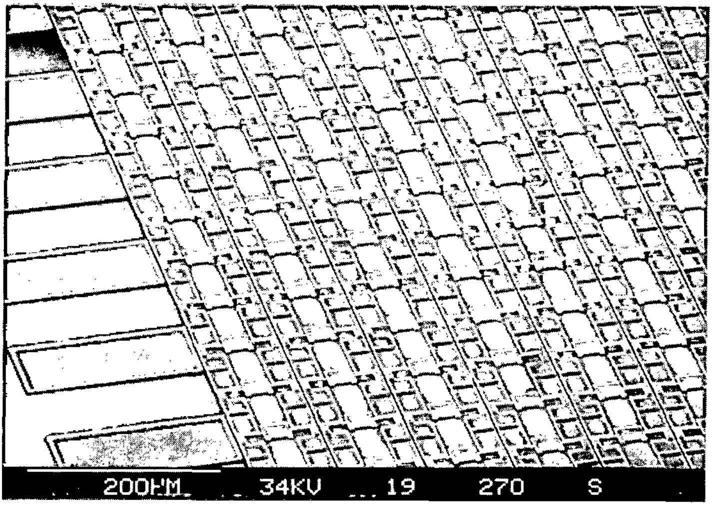

Fig. 4.31 Two-dimensional polysilicon mirror array. SEM displays a corner of a 32 by 32 mirror array.

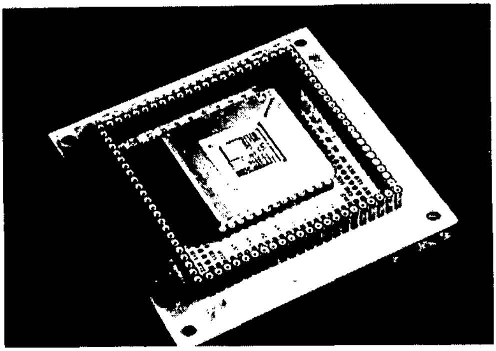

Fig. 4.32 Photograph showing mirror matrix mounted on a PGA 124 support for testing.

First testing has been performed by the use of a charge-coupled device (CCD) camera. As shown in Figure 4.33a, a collimated source projects light onto the mirror array. Only if the mirrors are deflected, the light is reflected directly into the CCD camera. In Figure 4.33b, it is illustrated that a displacement of the mirror by an angle ϕ results in a deviation of the laser beam by an angle 2ϕ. A typical image that can be obtained with this set-up is visualized in Figure 4.34: a 32 mirror by 32 mirror matrix is shown at two different switching states. In the first micrograph, no voltage is applied on the mirrors - all devices are at rest - and hardly no light is received by the camera. In the second micrograph, on particular lines and rows, a potential higher than V_1 has been applied. It can be clearly seen that the addressed lines and columns are tilted. At the crosspoints of an addressed line and column the potential difference between the two electrodes is zero, this results in mirrors at rest position.

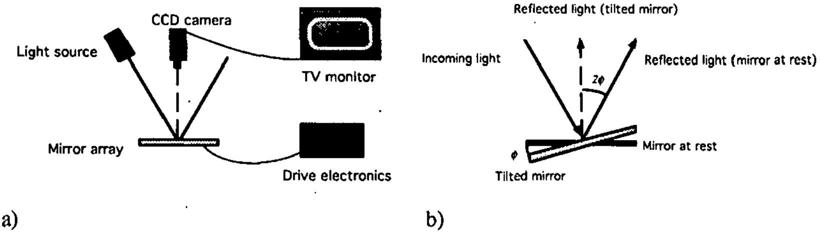

Fig. 4.33 Setup used to test pivoting mirror matrix: **a)** complete setup; **b)** deflection of the incoming light on a mirror at rest and in the tilted position, while the mirror is tilted by an angle ϕ, the light is deflected by an angle 2ϕ.

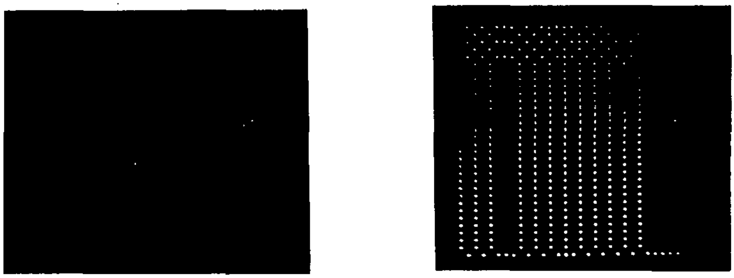

a) b)

Fig. 4.34 Optical micrographs of 32 by 32 mirror matrix at two different addressing states: **a)** no voltage is applied - all mirrors are at rest position, **b)** lines and rows have been selectively addressed.

Since the 1024 mirrors have to be addressed individually, multiplexing is important. The method we used is based on the bistability of the mirror displacement. The proper choice of the following voltages is important. V_c is a hold voltage which is between the threshold voltages V_1 and V_2, $V_c + V_d$ is still smaller than V_1, and $V_c + 2V_d$ is larger than V_1. The constant potential V_c is applied on all the columns, and all the lines are on ground potential. If a particular mirror has to be tilted, on the column a pulse of the height $+ V_d$ is applied, simultaneously a pulse of the height $- V_d$ is applied on the specific line. Since the mirrors will be tilted only if a voltage difference of $V_c + 2V_d$ is applied, all the mirrors will rest in their position and only the mirror at the position where the activated line crosses the activated column will be tilted. This procedure is visualized in Figure 4.35. The driving electronics has been realized by the CSEM. A Motorola microprocessor 68705R3 is the key component of the control setup. The mirrors which are to be tilted can be programmed by utilizing hex addresses. The result of addressing the three letters IMT on a 32 by 32 mirror array is shown in Figure 4.36. Because of the variation of the threshold voltages V_1 and V_2 over the different mirrors, it is difficult to address all the mirrors correctly by employing just one fixed V_c and V_d. The variation of the threshold voltages is believed to be due to local changes in the etching of the submicrometer wide torsional suspension beams.

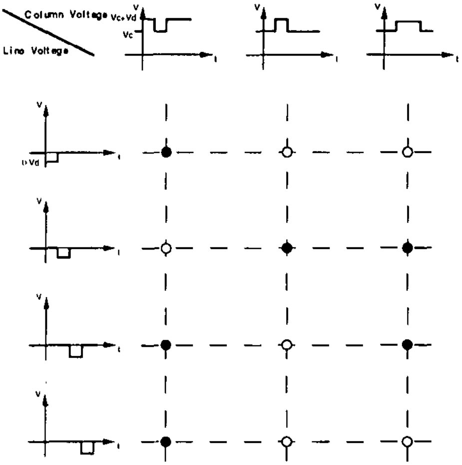

Fig. 4.35 Addressing of mirrors in a two-dimensional array. On the outside, diagrams of the different column and line voltages are displayed while on the inside, the switch states of the mirrors are indicated. Empty circles symbolize mirrors in zero position and full circles tilted mirrors.

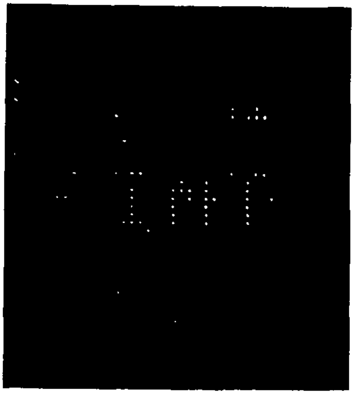

Fig. 4.36 The three letters IMT addressed on a 32 by 32 mirror array.

4.3.3 Interference light modulators

For modulating light at higher frequencies than the pivoting mirrors, interference light modulators have been conceived. While other high frequency light modulators are changing the refractive index of the material or the Bragg diffraction based on electro-optic, magneto-optic, respectively acousto-optic effects, our devices modulate the length of the optical path mechanically. In the first device, realized in collaboration with Ascom Tech, the optical path is changed by positioning two aluminum coated polysilicon bridges relative to each other (Figure 4.37a). The incident collimated laser beam is reflected on the aluminum coating; thereby, a phase difference is created between the light reflected on either of the bridges. By superposing the two light beams afterwards, interferences are created, which allow to modulate the amplitude of the light at a given point. The second device is not aluminum coated, and it takes advantage that the thin polysilicon bridge is semitransparent. It works as a Fabry-Perot interferometer, where the width of an optical resonance cavity, formed between the membrane and the substrate, can be modulated (cf. Figure 4.37b); thus, changing the spectral reflectivity of the incident beam.

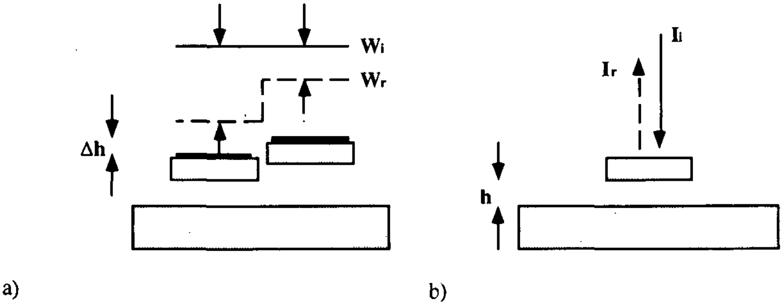

Fig. 4.37 Two operating principles of interference light modulators: **a)** a step is mechanically changed; by that means, a phase difference on the reflected beams is created (visualized is an incoming and reflected wave front). **b)** the width of an optical resonance cavity is changed; thereby, the total reflectance of the Fabry-Perot interferometer is modulated.

For a better understanding of the phase step modulator, the interferences occuring at the focal point of a lens have been investigated. Calculations have been performed using Fast Fourier Transformations of the commercial software package Matlab®. In Figure 4.38, the intensity distribution in the focal spot has been calculated for two phase step conditions. In both cases, the beam has a Gaussian intensity distribution before reflection. Figure 4.38a shows the situation when there is no phase difference between the beams reflected on the two bridges. A single peak exists - the light can propagate in a monomode fiber positioned at the focal point. Figure 4.38b displays the result when the bridges are displaced against each other by $\lambda/4$, i.e., the reflected beam has a phase difference of $\lambda/2$. Maximal interferences are obtained, and two peaks exist - the light will not propagate in a monomode fiber positioned at the focal point. Hence, with such a setup, the phase step modulator can be used as amplitude modulator.

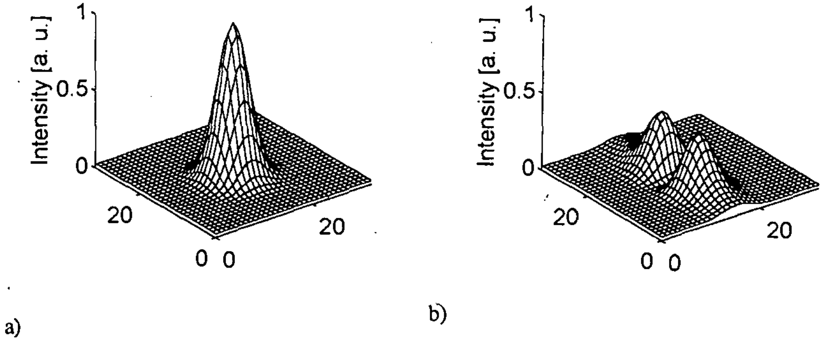

Fig. 4.38 Calculated intensity distribution at focal point of a lens for phase step modulator: **a)** no phase difference between the two reflected beams; **b)** phase difference of $\lambda/2$ between the two reflected beams.

The second operation mode - Fabry-Perot interferometer - is described analytically. The total reflectance R of the Fabry-Perot interferometer can be expressed by the Airy formula [4.16]

$$R = \frac{1}{1 + \frac{(1 - r_m)^2}{4r_m \sin^2(2\pi nh/\lambda)}} \tag{4.9}$$

where r_m is the mirror reflectance, h is the cavity gap, and λ is the wavelength. This formula assumes that the incident light is normal to the mirror surface, and it ignores absorption of the light. From the expression follows that a minimum reflectance is obtained if the width h of the cavity is a multiple of $\lambda/2$, and that the maximum reflectance is achieved if h is an uneven multiple of $\lambda/4$.

A finished device is shown in Figure 4.39. The polysilicon bridges are not aluminum coated; hence, this particular device can be used as Fabry-Perot interferometer. Figure 4.40 displays the displacement curve of the center of a straight beam light modulator. The measurements have been performed using the confocal microscope. A maximum displacement of 0.4 μm has been observed, larger displacements result in collapsing bridges. However, this displacement amplitude is sufficient for modulating visible light with the two operation principles because only displacements of the order of $\lambda/4$ have to be performed. The dynamic behavior of the structures has also been investigated. In Figure 4.41, the response in function of the driving frequency has been measured employing a laser interferometer (measurements performed by Ascom Tech). Depending on the bridge length, the system is under critically, critically, or over critically damped.

First tests, in the operation mode as Fabry-Perot interferometer, showed that the reflectivity of an incident laser beam of 780 nm wavelength can be modified between 38 % and 72 % when the cavity width is changed by applying a potential between the bridge and the lower electrode on the substrate. Also the light modulation by changing the phase step has been successful [4.58]. There, the following two problems exist: first, the gap of 2.7 μm between the two beams is rather large for this operation principle; and second, the speckle caused by the surface roughness of the aluminum reduces the efficiency of this operation mode.

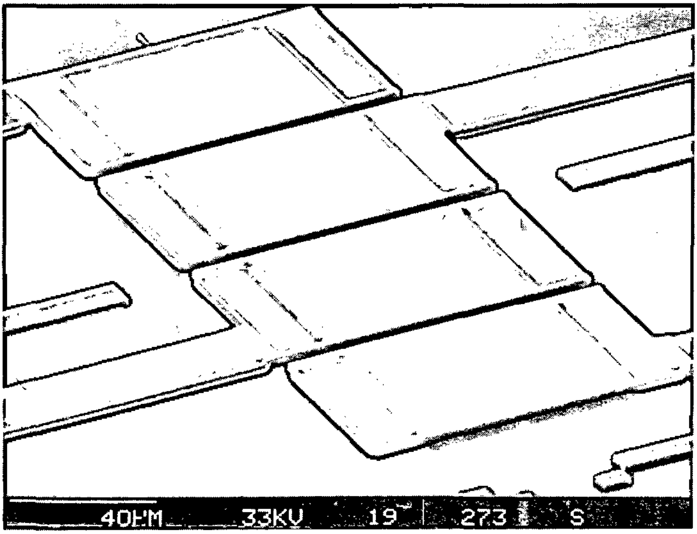

Fig. 4.39 Interference light modulator (SEM). It consists of four polysilicon bridges of a length of 70 μm, a width of 50 μm and a thickness of 2 μm. The bridges are separated by a gap of 2.7 μm and suspended 2 μm above the substrate.

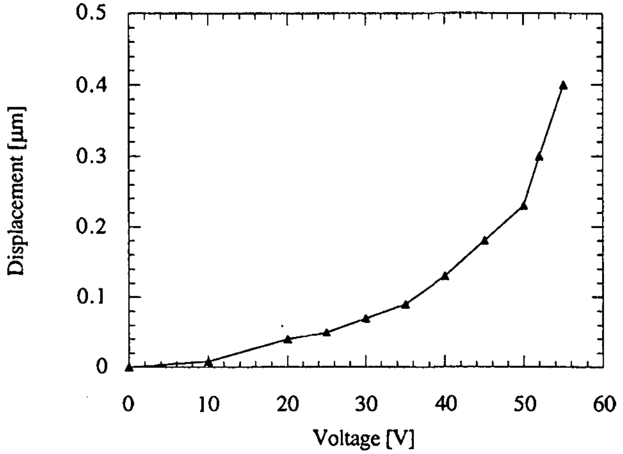

Fig. 4.40 Displacement versus voltage curve of interference light modulator (70 µm long and 0.5 µm thick polysilicon bridge). The measurements have been performed with a confocal microscope. At higher voltages the bridge will collapse and touch the substrate.

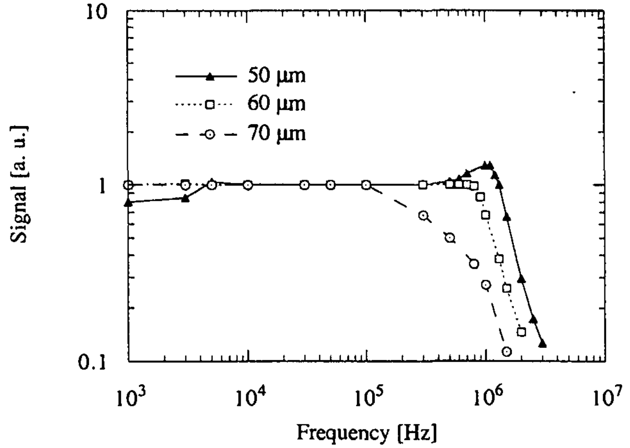

Fig. 4.41 Dynamic response of interference light modulators having different bridge lengths. The quality factor can be deduced - for bridges of 50 µm, 60 µm, and 70 µm length, it is 0.6, 0.5, 0.35, respectively.

The presented interference light modulators are prototype devices, which show that using two different operation principles incident light can be modulated at very high speed. However, if they are used for real applications, the structures have to be optimized. For example, if employed as Fabry-Perot interferometer, the reflectance of the mirrors has to be optimized for the wavelength of operation and at the same time the top mirror absorption has to be minimized. On the other hand, if used as phase step modulator, the gap between the two bridges and the surface roughness have to be minimized

References

[4.1] G. Tribillon, "Interférométrie et mesures", in *Recherches en Microtechniques: Réalités et Perspectives* , Collection du livre vert, Besançon, France, Jan. 1992.

[4.2] K. J. Strozewski, C.-Y. Wang, G. C. Wetsel, R. M. Boysel, and J. M. Florence, "Characterization of a micromechanical spatial light modulator", *J. Appl. Phys.*, vol 73, no. 11 (1993), pp. 7125-7128.

[4.3] J. Brugger, R. A. Buser, N. F. de Rooij, "Micromachined atomic force microprobe with integrated capacitive read-out", *J. Micromech. Microeng.*, vol. 2 (1992), pp. 218-220.

[4.4] D. Kobayashi, T. Hirano, T. Furuhata, H. Fujita, "An integrated lateral tunneling unit", in *Tech. Dig. IEEE Micro Electro Mechanical Systems*, Travemünde, Germany, Feb. 1992, pp. 214-219.

[4.5] W. C. Tang, T. H. Nguyen and R. T. Howe, "Laterally driven polysilicon resonant microstructures", *Sensors and Actuators*, vol. A20 (1989), pp 25-32.

[4.6] V. P. Jaecklin, C. Linder, N. F. de Rooij, J.-M. Moret, and R. Vuilleumier, "Optical microshutters and torsional micromirrors for light modulator arrays", in *Tech. Dig. IEEE Micro Electro Mechanical Systems Workshop*, Fort Lauderdale, FL, USA, Feb. 1993, pp. 124-127.

[4.7] O. Brand, H. Baltes, and U. Baldenweg, "Thermally excited silicon oxide bridge resonators in CMOS technology", *J. Micromech. Microeng.*, vol. 2 (1992), pp. 208-210.

[4.8] R. A. Brennen, M. G. Lim, A. P. Pisano, and A. T. Chou, "Large displacement linear actuator", in *Tech. Dig. IEEE Micro Electro Mechanical Systems Workshop*, Napa Valley, CA, USA, Feb. 1990, pp. 135-139.

[4.9] N. Takeshima, K. J. Gabriel, M. Ozaki, J. Takahashi, M. Horiguchi, and H. Fujita, "Electrostatic parallelogram actuator", in *Tech. Dig. IEEE Micro Electro Mechanical Systems Workshop*, Nara, Japan, Jan. 1991, pp. 63-66.

[4.10] K. Suzuki and H. Tanigawa, "Alternative process for silicon linear micro-actuators", in *Tech. Dig. 9th Sensor Symposium*, Tokyo, Japan, May 1990, pp. 125-128.

[4.11] C. J. Kim, A. P. Pisano, R. S. Muller, and M. G. Lim, "Silicon-processed overhanging microgripper", *J. Microelectromech. Systems*, vol. 1, no. 1 (1992), pp. 31-36.

[4.12] T. Hirano, T. Furuhata, J. J. Gabriel, and H. Fujita, "Design, fabrication, and operation of submicron gap comb-drive microactuators", *J. Microelectromech. Syst.*, vol. 1, no. 1 (1992), pp. 52-59.

[4.13] M. W. Judy and R. T. Howe, "Highly compliant lateral suspensions using sidewall beams", in *Tech. Dig. 7th International Conference on Solid-State Sensors and Actuators*, Yokohama, Japan, June 1993, pp. 54-57.

[4.14] V. P. Jaecklin, C. Linder, N. F. de Rooij, J.-M. Moret, R. Bischof, and F. Rudolf, "Novel polysilicon comb-actuators for xy-stages", in *Tech. Dig. IEEE Micro Electro Mech. Syst. Workshop*, Travemünde, Germany, Feb. 1992, pp. 147-149.

[4.15] V. P. Jaecklin, C. Linder, N. F. de Rooij, and J.-M. Moret, "Micromechanical comb actuators with low driving voltage", *J. Micromech. Microeng.*, vol. 2, no. 4 (1992), pp. 250-255.

[4.16] F. Kneubühl, *Repetitorium der Physik*, Teubner Studienbücher Physik, Stuttgart, 1982.

[4.17] M. A. Schmidt, R. T. Howe, S. D. Senturia, and J. H. Haritonidis, "Design and calibration of a microfabricated floating-element shear stress sensor", *IEEE Trans. Electron Devices*, vol. ED-35 (1988), pp. 750-757.

[4.18] V. P. Jaecklin, C. Linder, N. F. de Rooij, and J.-M. Moret, "Comb actuators for xy-microstages", *Sensors and Actuators*, vol. A39 (1993), pp. 83-89.

[4.19] W. C. Tang, M. G. Lim, R. T. Howe, "Electrostatic comb drive levitation and control method", *J. Electromech. Syst.*, vol. 1, no. 4 (1992), pp. 170-178.

[4.20] C. Linder, V. P. Jaecklin, and N. F. de Rooij, "Modeling and performance of electromechanical polysilicon actuators", submitted to *J. Microelectromech. Syst.*

[4.21] S. Futami, A. Furutani, and S. Yoshida, "Nanometer positioning and its micro-dynamics", *Nanotechnology*, vol. 1 (1990), pp. 31-37.

[4.22] G. Binnig, H. Rohrer, Ch. Gerber, and E. Weibel, "Surface studies by scanning tunneling microscopy", *Phys. Rev. Letters*, vol. 49, no. 1 (1982), pp. 57-61.

[4.23] G. Binnig, C. F. Quate, and Ch. Gerber, "Atomic force microscopy", *Phys. Rev. Letters*, vol. 56, no. 1 (1986), pp. 930-933.

[4.24] H.-J. Güntherodt and R. Wiesendangher (ed.), "Scanning tunneling microscopy. Further applications and related techniques", *Springer Series in Surface Sciences 28*, Berlin 1992.

[4.25] S. Akamine, T. R. Albrecht, M. J. Zdeblick, and C. F. Quate, "A planar process for microfabrication of a scanning tunneling microscope", *Sensors and Actuators*, A21-A23 (1990), pp. 964-970.

[4.26] J. J. Yao, S. C. Arney, and N. C. MacDonald, "Fabrication of high frequency two-dimensional nanoactuators for scanned probe devices", *J Microelectromech. Syst.*, vol. 1 (1992), pp. 14-22.

[4.27] J. Brugger, V. P. Jaecklin, R. A. Buser, C. Linder, and N. F. de Rooij, "Micromachined silicon tools for nanometer-scale science", in *Nanosources and Manipulation of Atoms Under High Fields and Temperatures: Applications*, V. T. Binh et al. (eds.), Kluwer Academic Publishers, Netherlands, 1993, pp. 311-317.

[4.28] The Institution of Electrical Engineers, *Properties of Silicon*, Unwin Brothers, The Gresham Press, Surrey, United Kingdom, 1988.

[4.29] A. Bossche, H. C. J. M. van Gestel, J. R. Mollinger, "On-chip metal deformation measurements: a capacitive approach" *Sensors and Actuators*, A25-A27 (1991), pp. 789-792.

[4.30] D. Rugar, H. J. Mamin, and P. Guethner, "Improved fiber-optic interferometer for atomic force microscopy", *Appl. Phys. Lett.*, vol. 55 (1989), pp. 2588-2591.

[4.31] K. Preston Jr., "An array optical spatial phase modulator", in *Tech. Dig. IEEE International Solid State Circuits Conference* (Institute of Electrical and Electronics Engineers, New York, 1968), p. 100.

[4.32] J. A. van Raalte, "A new Schlieren light valve for television projection", *Appl. Opt.*, vol. 9 (1970), pp. 2225-2230.

[4.33] R. N. Thomas, J. Guldberg, H. C. Nathanson, and P. R. Malmberg, "The mirror-matrix tube: a novel light valve for projection displays", *IEEE Trans. Electron. Devices*, vol. 22 (1975), pp. 765-775.

[4.34] K. E. Petersen, "Micromechanical light modulator array fabricated on silicon", *Appl. Phys. Lett.*, vol. 31, no. 8 (1977), pp. 521-523.

[4.35] K. E. Petersen, "Silicon torsional scanning mirror", *IBM J. Res. Develop.*, vol. 24, no. 5 (1980), pp. 631-637.

[4.36] "Mikromechanik verlängert Lebensdauer", *Markt & Technik*, vol. 15 (1992), pp. 47-48.

[4.37] D. R. Pape, L. J. Hornbeck, "Characteristics of the deformable mirror device for optical information processing", *Opt. Eng.*, vol. 22, no. 6 (1983), pp. 675-681.

[4.38] L. J. Hornbeck, "Deformable-mirror spatial light modulators", in *Tech. Dig. Soc. Photo-Opt. Instrum. Eng.*, vol. 1150 (1989), pp. 86-102.

[4.39] J. B. Sampsell, "The digital micromirror device and its application to projection displays", in *Tech. Dig. 7th International Conference on Solid-State Sensors and Actuators*, Yokohama, Japan, June 1993, pp. 24-27.

[4.40] H. Toshiyoshi, H. Fujita, T. Kawai, and T. Ueda, "Piezoelectrically operated actuators by quartz micromachining for optical application", in *Tech. Dig. IEEE Micro Electro Mechanical Systems Workshop*, Fort Lauderdale, FL, USA, Feb. 1993, pp. 133-138.

[4.41] O. Tabata, R. Asashi, N. Fujitsuka, M. Kimura, and S. Sugiyama, "Electrostatic driven optical chopper using SOI wafer", in *Tech. Dig. 7th International Conference on Solid-State Sensors and Actuators*, Yokohama, Japan, June 1993, pp. 124-127.

[4.42] J. H. Herman and D. J. Clift, "Miniature Fabry-Perot interferometers micromachined in silicon for use in optical fiber WDM systems", in *Tech. Dig. 6th International Conference on Solid-State Sensors and Actuators*, San Francisco, CA, USA, June 1991, pp. 372-375.

[4.43] K. Aratani, P. J. French, P. M. Sarro, R. F. Wolffenbuttel, and S. Middlehoek, "Process and design considerations for surface micromachined beams for a tuneable interferometer array in silicon", in *Tech. Dig. IEEE Micro Electro Mechanical Systems Workshop*, Fort Lauderdale, FL, USA, Feb. 1993, pp. 230-235.

[4.44] N. F. Raley, D. R. Ciarlo, J. C. Koo, B. Beiriger, J. Trujillo, C. Yu, G. Loomis, and R. Chow, "A Fabry-Perot microinterferometer for visible wavelengths", in *Tech. Dig. IEEE Solid-State Sensors and Actuators Workshop*, Hilton Head Island, SC, USA, 1992, pp. 170-173.

[4.45] O. Solgaard, F. S. A. Sandejas, and D. M. Bloom, "Deformable grating optical modulator", *Opt. Lett.*, vol. 17 (1992), no. 9, pp. 688-690.

[4.46] K. Gustafsson and B. Hök, "A silicon light modulator", *J. Phys. E: Sci. Instrum.*, vol. 21 (1988), pp. 680-685.

[4.47] R. A. Buser, N. F. de Rooij, H. Tischhauser, A. Domman, and G. Staufert, "Biaxial scanning mirror activated by bimorph structures for medical applications", *Sensors and Actuators*, vol. A31 (1992), pp. 29-34.

[4.48] K. E. Mattsson, "Surface micromachined scanning mirrors", *Microelect. Eng.*, vol. 19 (1992), pp. 199-204.

[4.49] E. Obermeier, J. Lin, and V. Schlichting, "Design and fabrication of an electrostatically driven micro-shutter", in *Tech. Dig. 7th International Conference on Solid-State Sensors and Actuators*, Yokohama, Japan, June 1993, pp. 132-135.

[4.50] J. Mohr, M. Kohl, and W. Menz, "Micro optical switching by electrostatic linear actuators with large displacements", in *Tech. Dig. 7th International Conference on Solid-State Sensors and Actuators*, Yokohama, Japan, June 1993, pp. 120-123.

[4.51] K. Gustafsson and B. Hök, "Fiberoptic switching and multiplexing with a micromechanical scanning mirror", in *Tech. Dig. 5th International Conference on Solid-State Sensors and Actuators*, Montreux, Switzerland, June 1987, pp. 212-215.

[4.52] T. G. MacDonald, R. M. Boysel, and J. B. Sampsell, "4 x 4 fiber optic crossbar switch using the deformable mirror device", in *Tech. Dig. Spatial Light Modulators and Applications 1990*, Optical Society of America, Washington, D.C., vol. 14 (1990), pp. 80-83.

[4.53] R. W. Cohn, "Link analysis of a deformable mirror device based optical crossbar switch", *Opt. Eng.*, vol. 31, no. 1 (1992), pp. 134-140.

[4.54] M. A. Cadman, A. Perret, F. Porret, R. Vuilleumier, and P. Weiss, "New micromechanical display using metallic films", *IEEE Electron. Dev. Lett.*, vol. 4, no. 1 (1983).

[4.55] R. Vuilleumier, A.-E. Perret, F. Porret, and P. Weiss, "Novel electromechanical microshutter display device", *Tech. Dig. SID Eurodisplay '84*, Paris, France, Sept. 1984, pp. 41-44.

[4.56] S. Timoshenko, D. Young, W. Weaver, *Vibration Problems in Engineering*, John Wiley & Sons, 4th edition, New York, USA, 1974.

[4.57] W. E. Newell, "Miniaturization of tuning forks", *Science*, vol. 161 (1968), pp. 1320-1326.

[4.58] O. Anthamatten, personal communication.

Characterization of Materials

For the design of micromechanical devices, it is important to have a good knowledge about the mechanical properties of the materials used. This is not a new requirement, it holds true for any kind of mechanical engineering. What is distinct, however, is that some materials have different characteristics in macroscopic dimensions than in microscopic dimensions. For example, everyday laboratory experience is that silicon wafers tend to break or chip without any apparent provocation leading to the conception that silicon is a very fragile material. Such fracture is usually initiated at the surface; the probability of surface flaws of "critical" size decreases with decreasing area of stressed surface. From a statistical point of view, small sized elements can endure a higher maximum stress than larger samples. This is the main cause why we observe strength properties on micromachined silicon devices which are superior than those of high quality steel. Another reason why results from traditional macroscopic experiments are not accurate enough is that mechanical properties depend strongly on the deposition parameters of the thin films. For example, *Koskinen et al.* have demonstrated that the tensile strength of polysilicon depends on its grain size [5.1]. Therefore, it is often necessary, to reconsider the mechanical properties of the materials with the help of micromechanical tests. Depending on the application, other material characteristics will also be of concern such as electrical, chemical, or, as in our case, optical properties of thin films.

While some of the mechanical properties for micromachined devices have already been determined by other authors, our approach is novel in so far as we used the same masks for surface micromachining different materials. This allows to compare mechanical characteristics on geometrically identical structures. The investigations on mechanical properties as internal strains, sticking phenomena, and yield strains are reported in Chapter 5.1 while Chapter 5.2 focuses on optical characteristics such as surface reflectivities as well as low and wide angle scattering characteristics. In the literature, there are few contributions about the long time stability of micromachined devices - about life testing of polysilicon structures we have not found any report. Therefore, Chapter 5.3 is dedicated to the description of endurance testing that has been performed on polysilicon torsional mirrors.

The pivoting micromirrors used throughout this chapter for characterization are shown in Figure 5.1. Fabricated in the three materials single crystal silicon, polycristalline silicon and aluminum, they have the same geometric dimensions: they are 30 μm by 30 μm squares suspended by 15 μm long and about 0.6 μm wide torsion beams [5.2].

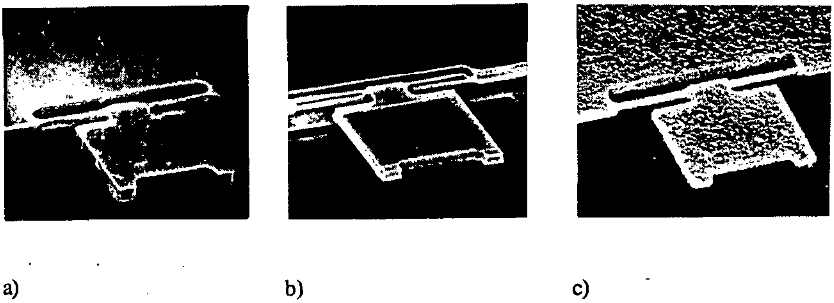

Fig. 5.1 SEM top views showing torsional micromirrors fabricated in: **a)** single crystal silicon, **b)** polycrystalline silicon, **c)** aluminum.

5.1 Mechanical Properties

Investigations about mechanical characteristics of micromachined devices have been performed since the beginning of micromechanics. For example, *Nathanson et al.* have determined the Young's modulus by observing the resonance behavior of small vibrating cantilevers fabricated in different metals [5.3], *Eisner* has performed tensile stress tests on silicon whiskers [5.4], *Guckel et al.* have established strain tests by visually observing the deflection/buckling of custom designed release structures [5.5], and *Cho et al.* employ the electromechanical performance of simple structures to estimate Young's modulus and intrinsic stress [5.6]. *Schweitz* gives a good summary of mechanical properties and characterization methods of thin films in a review article [5.7].

Section 5.1.1 investigates internal strains based on observations on simple test structures. The sticking of free standing surface micromachined doubly clamped beams to the substrate is discussed in Section 5.1.2. By performing bending tests on cantilevers, the yield strain of the different materials is established in Section 5.1.3. Finally, the electromechanical performance is compared for structures fabricated in the different materials in Section 5.1.4. Throughout the whole chapter, pivoting micromirrors will serve as test vehicle.

5.1.1 Internal strains

Internal stress and strain of deposited films are routinely observed in IC fabrication lines by investigating the wafer bow. More sophisticated techniques include tests on micromachined structures such as the shift of resonance frequency [5.8] or the continuous deformation of structures due to strains [5.9, 5.10]. The method used here is the investigation of buckling of test structures. The advantage of this procedure is that by simple visual inspections under the light microscope, it can be determined whether a certain strain limit is attained or not.

Compressive internal strains are investigated by observing the buckling of doubly clamped beams (compressive stress). As stated by *Guckel et al.*, the buckling strain can be calculated by determining the length L of the shortest beams that are buckling [5.11]. The Euler's buckling criterion is employed to establish the yield strain

$$\varepsilon_c = \frac{\pi^2 h^2}{3L^2} \tag{5.1}$$

For polysilicon and silicon the longest beams that can be observed are 400 μm long - they did not show buckling. Therefore, the compressive strain can be assumed to be below 82.3 ppm. Unannealed aluminum beams showed buckling for a beam length of 100 μm and longer (cf. Figure 5.2a); the computed compressive strain is thus 0.132 %. When the aluminum has been annealed at 450°C during 30 minutes (Section 3.2.1), also the 200 μm long beams did not show any buckling (cf. Figure 5.2b).

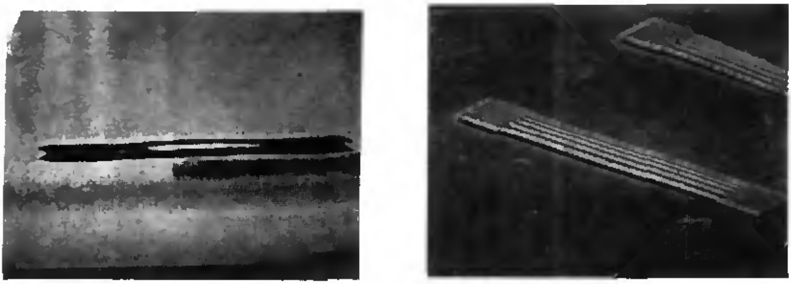

a) b)

Fig. 5.2 Doubly clamped beams for investigating compressive stresses: **a)** 100 µm long aluminum beams before annealing, **b)** 200 µm long aluminum beams after annealing.

Since polysilicon tends to have slight tensile strain after annealing as proposed by *Kamins* [5.12], also test structures for tensile stresses have been devised. For the investigation, we have employed the ring and beam structures proposed by *Guckel et al.* [5.13]. Contraction of the ring structure is inducing strain on the cross beam, causing it eventually buckle. Since the beam is also contracting, mathematical description is rather complicated, and for a detailed analysis we refer to the paper quoted above. The largest ring and beam structures we are able to observe have a radius of 200 µm (cf. Figure 5.3). None of these devices exhibits any buckling; therefore, it can be concluded that the tensile strain is below 300 ppm.

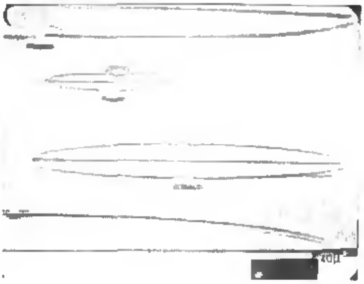

Fig. 5.3 Polysilicon ring and beam structure for investigation of internal tensile strain; no buckling is observed.

5.1.2 Sticking phenomena

Sticking of surface micromachined structures to the substrate is a phenomenon, which has been examined by different laboratories recently. Most authors agree that sticking occurs after the final rinse, where the diminishing liquid draws the suspended structure into contact with the underlying substrate. After complete drying, the structure remains stuck to the surface. It has been proposed that etch residues [5.14, 5.15], electrostatic forces [5.16], condensation of water between the two surfaces [5.17, 5.18], and van der Waals forces [5.19] are responsible for the sticking. In summary, the nature and the magnitude of these adhesion forces are not well understood to date. Therefore, we have not tried to confirm a particular theory, but we compared experimentally the sticking of structures fabricated in the different materials.

The sticking phenomenon is examined on the doubly clamped beams which are suspended 2 μm above the substrate (the identical structure as employed for the investigation of internal compressive strain). The maximum length, the bridges can stand free in more than 80% of the observations, are reported in Table 5.1; this is the status after the final rinse in alcohol. Comparatively long polycrystalline silicon beams (400 μm) are completely free standing after processing; this may be due to the increased surface roughness of the polysilicon. Even a small degree of roughness will reduce adhesion forces by several orders of magnitude [5.15]. The surface of the silicon beams are much smoother and the maximum length of free standing beams is 200 μm. The maximum length of free standing aluminum beams is limited to 100 μm; there the difference is believed to be caused by the lower Young's modulus, which reduces the spring constant of the bridge.

5.1.3 Yield strains

Yield strains are established by determining the maximum lateral bending of cantilevers (cf. Figure 5.4) before they break (silicon, polysilicon) or before they deform plastically (aluminum). By using a microprober needle, a cantilever is bent until it yields. The experiment has been observed under the light microscope and is recorded on a video tape for later analysis. The maximum tensile strains are calculated by nonlinear beam theory. The subsequent considerations follow a reasoning proposed by *Tai and Muller* [5.20]. The calculation starts with the classic bending equation [5.21]

$$\frac{1}{r(x,y)} = \frac{M(x,y)}{EI} \tag{5.2}$$

where $r(x,y)$ is the curvature radius, $M(x,y)$ is the bending moment, E is the Young's modulus, and I is the moment of inertia. In the case of a rectangular cross section, the moment of inertia can be expressed as $I = 1/12\ (w^3t)$, where w is the beam width and t is the beam thickness. The curvature radius r can be rewritten as a differential equation.

$$-\frac{\mathrm{d}^2y/\mathrm{d}x^2}{(1 + (\mathrm{d}y/\mathrm{d}x)^2)^{3/2}} = \frac{F(y(L_p) - y)}{EI} \tag{5.3}$$

With L, the length of the cantilever, L_p, the projection length of the beam at maximum bending on the undeflected cantilever, F, the applied force, and the boundary conditions of Equation 5.3, which are $y(0) = 0$, $\mathrm{d}y(0)/\mathrm{d}x = 0$, and $\mathrm{d}^2y(L_p)/\mathrm{d}x^2 = 0$, the solution of $y(Lp)$ can be written as [5.22]

$$y(L_p) = \frac{2pL}{K(p)} \tag{5.4}$$

where $K(p)$ is the complete elliptic integral of the first kind. The following intermediate solutions for the differential equation are obtained

$$L_p = L\left(\frac{2E(p)}{K(p)} - 1\right) \tag{5.5}$$

$$F = EI\frac{K^2(p)}{L^2} \tag{5.6}$$

The quantities $K(p)$ and $E(p)$ are complete elliptic integrals of the first and second kind, respectively. These two functions are defined by

$$K(p) = \int_0^{\pi/2} (1-p^2\sin\phi)^{-1/2}\mathrm{d}\phi \tag{5.7}$$

$$E(p) = \int_0^{\pi/2} (1-p^2\sin\phi)^{1/2}\mathrm{d}\phi \tag{5.8}$$

The variable p can be determined by employing Equation 5.6 and using the experimentally determined L_p. Knowing the force F and the maximum deflection $y(Lp)$, the maximum strain (which occurs at the clamped end) can be established [5.23]

$$\varepsilon_{\pm max} = \pm \frac{M(0,0)w}{2EI} - \frac{F}{wtE}$$

$$= \pm p\,K(p)\frac{w}{L} - \frac{1}{12}K^2(p)\left(\frac{w}{L}\right)^2 \tag{5.9}$$

where the + sign stands for tension and the - sign for compression. Since in brittle materials the tensile stress is regarded as the most significant cause of fracture, ε_{+max} has been used to obtain the following results.

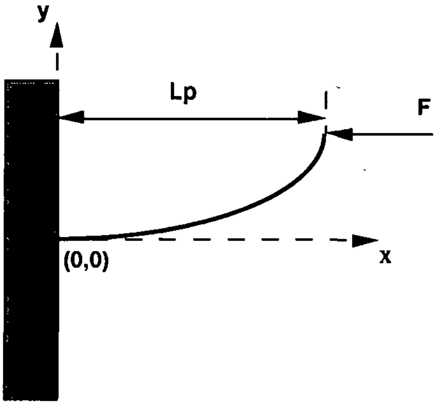

Fig. 5.4 Top view of axially loaded cantilever.

Typical maximum bending of silicon, polysilicon, and aluminum cantilevers is displayed in Figure 5.5; the calculated fracture strains are summarized in Table 5.1. The cantilevers are 3.8 µm wide and 200 µm long. For silicon beams in <110>-direction, an average fracture strain of 1.6 ± 0.1 % has been found; the uncertainty is given by the difficulty to measure precisely the width of the beams. This strain limit can be compared to measurements done on silicon whiskers by *Eisner* reporting a value of 2.03 % [5.4], *Pearson et al.* reporting a maximum fracture strain of 2.6 % [5.24], and *Johansson et al.* reporting an average fracture strain for <110> silicon cantilevers of 2.0 % [5.25]. On polysilicon structures, a fracture strain of 2.1 ± 0.1 % has been measured, which is higher than the limit of 1.72 % reported by *Tai and*

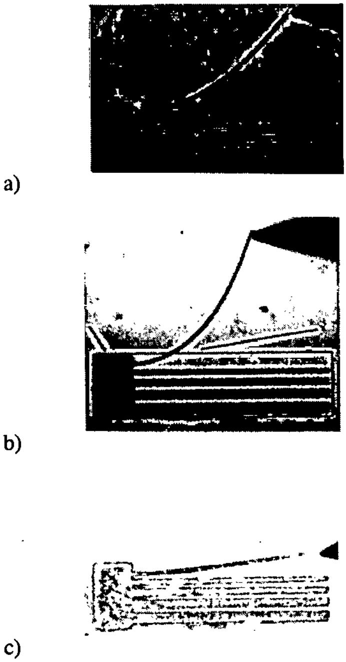

Fig. 5.5 Optical micrographs showing maximum lateral bending of cantilevers with identical dimensions (100 µm long, 2.8 µm wide, and 2 µm high) before yielding: a) silicon (fracture); b) polysilicon (fracture); c) aluminum (plastic deformation).

Muller [5.20]. The yield strain for aluminum (Al1%Si) cantilevers has been observed to be 0.5 ± 0.03 %; this is higher than the value (0.3 %) established for aluminum (Al5%Si) in traditional macromechanical yield strain tests [5.26].

In our tests, the stress concentration at the clamped edge has been ignored; therefore, the actual strain limits may be even higher. However, a major advantage of this method is that only geometric values and no material properties are required for determining the yield strain. Furthermore, fracture strength of brittle materials should be determined by statistical methods [5.27]. The reported results are based on an average value of five measurements; hence, the statistical significance is rather low.

5.1.4 Electromechanical performance

The electromechanical performance can be used to characterize material properties as proposed by *Nathanson et al.* [5.3]. This presumes that we have a good knowledge of the geometric dimensions of the structures under investigation. Since this is not the case for the torsion beams of pivoting micromirrors, the following paragraph is primarily a proof that working electromechanical devices can be constructed using the three different materials and technologies.

Using the notation of Section 4.3.2, the switching voltages V_1 can be compared. Since RIE under etching depends on the material, it produces unequal submicrometer beam widths (cf. Figures 5.1a and 5.1b). This mainly explains the voltage difference between the silicon (43 V) and polysilicon devices (15 V), that between polysilicon and aluminum devices (7 V) being essentially due to a difference in the Young's modulus.

Property	Mono-Si	Poly-Si	Al
Max. Temp. [°C]	1100	1050	450
Time [h]	4	0.67	0.5
Max. Freestanding Beam Length [µm]	200	400	100
Yield Strain [%]	1.6	2.1	0.5
Surface Reflectivity [%]	38.1	31.4	66.5

Table 5.1 Summary of properties of the three materials.

5.2 Optical Properties

The optical characteristics of the mirror surfaces are of great importance in view of future applications of micromachined mirrors in printing or projection display devices. While the surface roughness, which is causing the scattering, can be inspected directly by optical surface profiling or SFM profiling, we are interested in measuring the angle-resolved light scattering as proposed by *Heintze et al* [5.28]. The reflectivity has been determined by measuring the intensity of an almost perpendicular reflected laser beam.

5.2.1 Light scattering and reflectivity

Figures 5.6 and 5.7 show the scattering of a laser beam (633 nm) as a function of the incident angle (measurements are performed on a Jobin-Yvon Instruments ellipsometer). Little scattering is observed for narrow angles - the intensity follows the Gaussian distribution of the reflection on a perfect mirror (cf. Figure 5.6). However, at wider angles, there is some scattering observed for the aluminum mirrors (cf. Figure 5.7); it is due to the increased surface roughness caused by the BHF-$K_2Cr_2O_7$ etch solution ($\pm 1\sigma$ distribution: ±50 nm). As shown by *Heintze et al.* [5.28], the angle resolved scattering can be used to determine the surface roughness of polysilicon. Only recently, *Bawolek et al.* [5.29] compared such scattering results with roughness data obtained by a SFM measurements; they showed that there is a fair agreement between theory and measurements. The angle resolved scattering is a domain of itself, which we did not enter further because the obtained results assured us that pivoting mirror devices can be constructed with sufficient contrast ratios.

By integrating the angle resolved light intensity from -1 to +1 degree, the forward surface reflectivities are calculated (cf. Table 5.1). While the values for silicon (38.1 %) and polysilicon (31.4 %) are normal for IC-processing, the reflectivity of the aluminum mirror is rather low (66.5 %); the significant drop is caused by the etching in BHF-$K_2Cr_2O_7$; before this final step, the aluminum reflectivity was 83.0 %. For the optical devices presented in Chapter 4.3, the aluminum on top of the polysilicon has resisted an etching in a BHF-glycerol solution; this did induce less modification of the surface topography, and the measured reflectivity is 79 %.

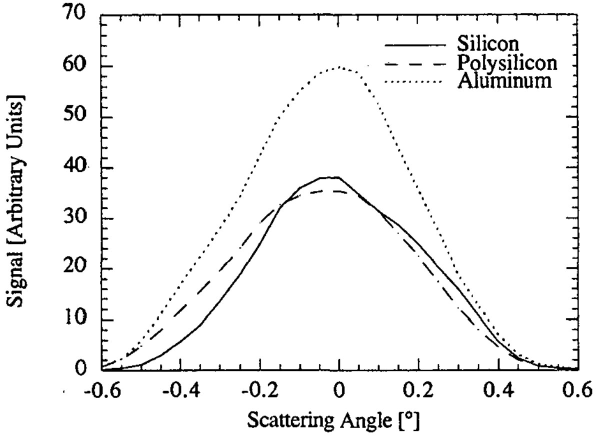

Fig. 5.6 Narrow angle scattering of silicon, polysilicon and aluminum mirrors (linear scale)

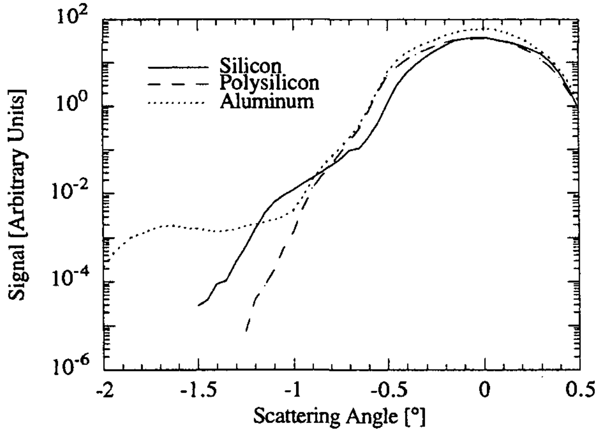

Fig. 5.7 Wide angle scattering of silicon, polysilicon and aluminum mirrors (logarithmic scale).

5.3 Endurance Testing

Fatigue effects are another domain of interest. Whether microdevices will be used as sensors or actuators, they have to perform a high number of cycles during their life time, and an aging could limit their applicability. Aging can result in catastrophic failures such as breaking or in less dramatic occurences like deformation or changes in the elastic constants. We have found only few reports about endurance tests. One of the earliest is about the life test of a silicon torsional scanning mirror by *Petersen*, where over 10^{12} cycles have been performed [5.30]. Aluminum mirrors have been cycled by *Hornbeck* over $1.2 \cdot 10^{10}$ times, where the devices are landing on an address electrode and no wear of the contact surfaces has been observed [5.31]. In the experiments of *Tabib-Azar et al.*, some aging of heavily doped (p^+) micromachined silicon cantilevers has been observed during aging tests of 10^{10} cycles [5.32]. Aging of aluminum coated silicon cantilevers is described by *Buser and Domman* [5.33]. In this chapter, results of life tests on polysilicon structures are reported; to our knowledge we were the first laboratory to publish on endurance testing of polysilicon structures [5.34].

5.3.1 Endurance tests on polysilicon pivoting mirrors

During 120 hours, a polysilicon micromirror with 20 µm long torsion beams, fixed near the edge of the 30 µm by 30 µm mirror, has been continuously cycled at frequencies of 1 kHz and 10 kHz, so that a total of over 10^9 cycles has been performed. At regular intervals, the switching characteristics have been investigated. A significant drift of the switch voltage V_1 and the release voltage V_2 has been observed during the test (cf. Figure 5.8). For example, the release voltage V_2 was initially 17 V - at the end of the test it was 10 V. We believe that these changes are due to trapped charges in the dielectric layer. Another measurement, which supports this hypothesis, is displayed in Figure 5.9. During dynamic operation at 1 kHz frequency the delay time of the mirror response has been measured, i.e., the time between the moment the potential has been set at zero and the moment the mirror is released from the landing electrode. While in the beginning of the test, the mirror is released immediately, after 100 hours of continuous testing, the device stays for some hundreds of microseconds longer in the down position. The performance characteristics has also been observed periodically

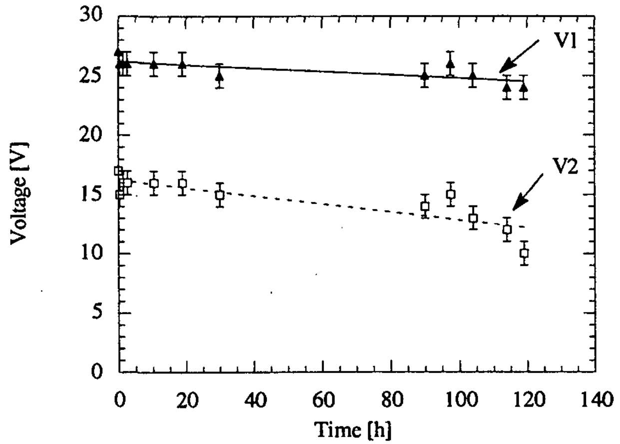

Fig. 5.8 Drift of switching voltage V_1 and release voltage V_2 during endurance test for a polysilicon torsional mirror (a total of over 10^9 cycles has been performed).

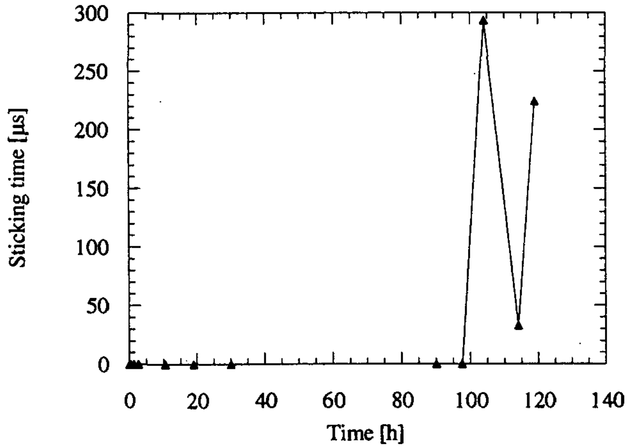

Fig. 5.9 Mirror response delay, i.e., the time between the moment the potential has been set at zero and the moment the mirror is released from the landing electrode.

after the endurance test. The delay time of the mirror response decreased continuously and 20 hours after the end, there was no measurable delay. The threshold voltages V_1 and V_2 increased slowly, but even one week after the test, they were only two to three Volts higher than at the end.

While there seems to be a certain charging of the electrodes, the mechanical characteristics did not shift during the whole test. Given the measurement limitations of ± 3 kHz, no drift of the resonance frequency has been observed.

References

[5.1] J. Koskinen, J. E. Steinwall, R. Soave, and H. H. Johnson, "Microtensile testing of free-standing polysilicon fibers of various grain sizes", *J. Micromech. Microeng.*, vol. 3 (1993), pp. 13-17.

[5.2] V. P. Jaecklin, C. Linder, J. Brugger, J.-M. Moret, R. Vuilleumier, and N. F. de Rooij, "Mechanical and optical properties of surface micromachined torsional mirrors in silicon, polysilicon and aluminum", in *Tech. Dig. 7th International Conference on Solid-State Sensors and Actuators*, Yokohama, Japan, June 1993, pp. 958-961.

[5.3] H. C. Nathanson, W. E. Newell, R. A. Wickstrom, and J. R. Davis Jr., "The resonant gate transistor", *IEEE Trans. Electron Devices*, ED-14 (1967), pp. 117-133.

[5.4] R. L. Eisner, "Tensile tests on silicon whiskers", *Acta Metallurgica*, vol. 3 (1955), pp. 414-415.

[5.5] H. Guckel, D. Burns, C. Rutigliano, E. Lovell, and B. Choi, "Diagnostic microstructures for the measurement of instrinsic strain in thin films", *J. Micromech. Microeng.*, vol. 2 (1992), pp. 86-95.

[5.6] S. T. Cho, K. Najafi and K. D. Wise, "Internal stress compensation and scaling in ultrasensitive silicon pressure sensors", *IEEE Trans. Electron Devices*, vol. 39, no. 4 (1992), pp. 836-842.

[5.7] J.-Å. Schweitz, "Characterization of mechanical properties of thin films", in *Tech. Dig. 3rd European Workshop on Micromachining, Micromechanics and Microsystems*, June 1992, Leuven, Belgium, pp. 56-85.

[5.8] L. M. Zhang, D. Uttamchandani, and B. Culshaw, "Measurement of the mechanical properties of silicon microresonators", *Sensors and Actuators*, vol. A29 (1991), pp. 79-84.

[5.9] J. F. L. Goosen, B. P. van Drieënhuizen, P. J. French, and R. F. Wolffenbüttel, "Stress measurement structures for micromachined sensors", in *Tech. Dig. 7th International Conference on Solid-State Sensors and Actuators*, Yokohama, Japan, June 1993, pp. 783-786.

[5.10] C.-J. Kim, R. S. Muller, and A. P. Pisano, "Residual strain measurement of thin films using microfabricated Vernier gauges", *Sensors and Materials*, vol. 4 (1993), pp. 291-304.

[5.11] H. Guckel, T. Randazzo, and D. W. Burns, "A simple technique for the determination of mechanical strain in thin films with applications to polysilicon", *J. Appl. Phys.*, vol. 57, no. 5 (1985), pp. 1671-1675.

[5.12] T. I. Kamins, "Design properties of polycristalline silicon", *Sensors and Actuators*, vol. A21-A23 (1990), pp. 817-824.

[5.13] H. Guckel, D. Burns, C. Rutigliano, E. Lovell, and B. Choi, "Diagnostic microstructures for the measurement of intrinsic strain in thin films", *J. Micromech. Microeng.*, vol. 2 (1992), pp. 86-95.

[5.14] H. Guckel, J. J. Sniegowski, and T. R. Christenson, "Advances in processing techniques for silicon micromechanical devices with smooth surfaces", in *Tech. Dig. IEEE Micro Electro Mechanical Systems Workshop*, Salt Lake City, UT, USA, June 1989, pp. 71-75.

[5.15] R. L. Alley, G. J. Cuan, R. T. Howe, and K. Komvopoulos, "The effect of release-etch processing on surface microstructure stiction", in *Tech. Dig. IEEE Solid-State Sensors and Actuators Workshop*, Hilton Head Island, SC , USA, June 1992, pp. 202-207.

[5.16] C. Linder and N.F. de Rooij, "Investigations on free-standing polysilicon beams in view of their applications as transducers", *Sensors and Actuators*, A21-23 (1990), pp. 1053-1059.

[5.17] P. R. Scheeper, J. A. Voorthuyzen, W. Olthuis, and P. Bergveld, "Investigations of attractive forces between PECVD silicon nitride microstructures and an oxidized silicon substrate", *Sensors and Actuators*, vol. A30 (1992), pp. 231-239.

[5.18] C. H. Mastrangelo and C. H. Hsu, "A simple technique for the measurement of the work of adhesion of microstructures", in *Proc. IEEE Solid-State Sensors and Actuators Workshop*, Hilton Head Island, SC , USA, June 1992, pp. 208-212.

[5.19] R. Legtenberg, J. Elders, and M. Elwenspoek, "Stiction of surface micromachined structures after rinsing and drying: model and investigation of adhesion mechanisms", in *Tech. Dig. 7th International Conference on Solid-State Sensors and Actuators*, Yokohama, Japan, June 1993, pp. 198-201.

[5.20] Y. C. Tai and R. S. Muller, "Fracture strain of LPCVD polysilicon", in *Tech. Dig. IEEE Solid-State Sensor and Actuator Workshop*, 1988, pp. 88-91.

[5.21] S. Timoshenko and D. H. Young, *Elements of Strength of Materials*, D. Van Nostrand Co., Princeton, NJ, 1968

[5.22] R. Frisch-Fay, *Flexible Bars*, Butterworth Inc., Washington, 1962.

[5.23] R. J. Roark and W. C. Young, *Formulas for Stress and Strain*, 5th ed., McGraw-Hill International Editions, Singapore, 1976.

[5.24] G. L. Pearson, W. T. Read Jr., and W. L. Feldmann, "Deformation and fracture of small silicon crystals", *Acta Metallurgica*, vol 5 (1955), pp. 181-191.

[5.25] S. Johansson, J.-Å. Schweitz, L. Tenerz, and J. Tirén, "Fracture testing of silicon microelements in situ in a scanning electron microscope", *J. Appl. Phys.*, vol. 63, no. 10 (1988), pp. 4799-4803.

[5.26] H. M. Trent, D. E. Stone, and L. A. Beaubien in D. E. Gray (ed.), *American Institute of Physics Handbook*, McGraw-Hill, Inc., New York, 1982, ch. 2e, pp. 2-62.

[5.27] A. de S. Jayatilaka, *Fracture of Engineering Brittle Materials*, Applied Science Publisher LTD, London, 1979.

[5.28] M. Heintze, P. E. Schmidt, F. Lévy, P. Weiss, and R. Guy, "Characterization of polycristalline and amorphous silicon films by angle-resolved light scattering", *J. Phys. D: Appl. Phys.*, vol 26 (1993), pp. 271-280.

[5.29] E. J. Bawolek, J. B. Mohr, E. D. Hirleman, and A. Majumdar, "Light scatter from polysilicon and aluminum surfaces and comparison with surface-roughness statistics by atomic force microscopy", *Appl. Opt.*, vol. 32 (1993), pp. 3377-3400.

[5.30] K. E. Petersen, "Silicon torsional scanning mirror", *IBM J. Res. Develop.*, vol. 24, no. 5 (1980), pp. 631-637.

[5.31] L. J. Hornbeck, "Deformable-mirror spatial light modulators" in *Proc. Soc. Photo-Opt. Instrum. Eng.*, vol. 1150 (1989), pp. 86-102.

[5.32] M. Tabib-Azar, K. Wong, and W. Ko, "Aging phenomena in heavily doped (p^+) micromachined silicon cantilever beams", *Sensors and Actuators*, vol. A33 (1992), pp. 199-206.

[5.33] R. A. Buser and A. Domman, "Accurate microscopic method to investigate the aging of micromachined silicon actuators", in *Tech. Dig. 7th International Conference on Solid-State Sensors and Actuators*, Yokohama, Japan, June 1993, pp. 172-174.

[5.34] V. P. Jaecklin, C. Linder, N. F. de Rooij, J.-M. Moret, R. Vuilleumier, "Mechanical and optical properties of surface micromachined torsional mirrors in silicon, polysilicon and aluminum", in *Tech. Dig. 7th International Conference on Solid-State Sensors and Actuators*, Yokohama, Japan, June 1993, pp. 958-961.

Conclusion and Outlook

Microactuators are a domain where the know-how still lacks behind that of sensors or electronics. Therefore, this work focused mainly on constructing working electrostatic actuators. The first class of such devices investigated here are the comb actuators; testing proved their applicability as precise positioners. They are also employed as the driving elements for a two-dimensional nanopositioner, on which a surface probe tip has been integrated. The second class of devices are the light modulators. Three different types of actuators we fabricated fall into this class: first, the comb-driven optical shutter, which allows to interrupt a focused laser beam; second, the deflectable micromirrors, which are particularly powerful if assembled in a dense array, where they can be used for light modulation as required in printing or projection display applications; and third, the interference light modulators which can modify a phase step or an optical resonance cavity at very high speed. The design, fabrication, and performance of all these devices has been studied in details and many promising results have been obtained. Insofar, the goal of this work to broaden the know-how about microactuators has been reached. But the motivation of the author and the researchers at the Institute of Microtechnology (IMT) for future work go beyond that, towards integrating the microactuators into microsystems - towards devices which are attractive for industrial purposes.

6.1 From Microactuators to Microsystems

For sensor and electronics fully integrated approaches already exist, as for example, the integrated mass flow sensor by *Yoon and Wise* [6.1], where the on chip CMOS circuitry allows the signal readout and control. For actuators, there are few devices for which such an integration with electronics has been accomplished. An excellent example, however, is the deformable mirror device fabricated by Texas Instruments - the micromechanical mirrors and the addressing electronics (SRAM) have been integrated on one chip [6.2]. The integration of the three elements, sensors, actuators, and electronics on one chip is further away, and today only hybrid assemblies for such microsystems exist [e.g., 6.3]. For future research in the microactuator domain, it will be important that the concept of an integration with electronics is considered and followed from the beginning.

For the devices presented in this work, this means for example that the *xy*-nanopositioner is to be integrated with the electronics for capacitive position detection and feed back on the electrostatic actuators. The micromirror array is to be fabricated on a chip containing an addressing electronics. And the interference light modulator is to be integrated with a solar cell for light detection and an electronics which allows to modify the phase step or the optical resonance cavity in function of the detected light signal.

The integration of actuators into microsystems is very important if industry has to interested, but it is not the only requirement. It is the personal belief of the author that there are a number of less technical issues, which have to be improved, in order to make from the research successes of the micromachinists also successes in the market. Such 'non-technic' issues are the subject of the last chapter.

6.2 From Academia to Market

Despite the booming research at universities in the domain of microactuators and microsystems, the commercialization of the technology is very sluggish. And there are only a handful of successful products containing microfabricated actuators on the market. The technology transfer from university to industry seems to be hampered.

One problem is certainly that the communication between industry and university is absent or not very open. Because of lacking inputs from industry, researchers at the university begin to dream up things they believe industry might need. Very often these prototypes are only replacements of products the industry already sells successfully, and, understandably, the interests on the industry side are limited. On the other hand, if people from the industry are coming to the university, they often have vague ideas about microsystems which are not compatible with the existing technology or cannot be developed in the required time frame. Because of such discrepancies, both sides are disappointed, and a joint project will never be formulated. To enhance the communication, it will be necessary that people from university and industry meet more frequently and that both discuss in an open and casual manner about their ideas and requirements. Good ways to promote this exchange of ideas are conferences, or as a different approach, the Community Programme for Education and Training in Technology (COMETT), where only recently an University Enterprise Training Partnership (UETP) for microelectromechanical systems (MEMS) has been launched. In short courses, people from industry and university can meet and inform themselves about general and selected topics of MEMS.

A further problem is that packaging is normally regarded as a non-academic issue. Because of this attitude many good devices will never be tested in a real environment - the barrier for the industry to get interested is often too high if the device is just glued on a printed circuit board. In this respect, the Neu-Technikum Buchs is a positive exception because they develop for most of their devices also an adapted package.

Another main concern is that the equipment required to fabricate the microsystems is very expensive, and the industry is afraid to invest a large amount of money in a risky technology. Here, the idea of silicon foundries as proposed by *Petersen* [6.4] might be a viable solution. As in IC foundries, customers can design their own micromechanical structure and receive small to medium quantities of chips from the same foundry within weeks. A silicon micromechanics foundry would consist of three major divisions: silicon microstructure design and modeling, silicon micromechanical wafer fabrication facility, silicon microstructure packaging and testing. Such a foundry has been recently opened in the United States, where the Microelectronics Center of North Carolina offers a two layer polysilicon surface micromachining process. Another approach is the fabrication of microsensors and actuators with CMOS technology and using some postprocessing of the mechanical devices as performed by a group at the Swiss Federal Institute of Technology in Zurich [6.5]. The investment of capital is rather low in such multiproject wafer services, and if a successful device is developed, it can be produced with rather fast fabrication cycles.

A further way is proposed by the IMT. In the fabrication facility of the institute prototypes can be developed and even small series for commercial purpose can be constructed. This is very successful, for example, for fabricating small series of micropumps sold in commercial equipments. For production on a larger scale, this may not be optimum since the institute wants to stay at the very edge of research in microsystems. However, in co-operation with the Swiss Center for Electronics and Microtechnology (CSEM) this dilemma can be avoided. The two-layer polysilicon process developed and described in this work is now being installed at the CSEM production facility. The advantage is that prospect industry partners can develop in collaboration with the IMT technology and design of new sensor and actuator devices. Once this has been achieved, the production can be transferred to the CSEM. As proved in this work, the technologies of the two institutions are almost compatible and the problems encountered usually with such technology transfers can be avoided. This flexibility and compatibility will allow to shorten the time from prototype to product, and it will also permit to cut development costs.

In summary, there exist ways to develop the fascinating prototypes realized in an academic environment into devices that are successful on the market. They will not be easy to follow and they are plenty of obstacles, but they are the great challenge of todays micromachinists.

References

[6.1] E. Yoon and K. D. Wise, "An integrated mass flow sensor with on-chip CMOS interface circuitry", *IEEE Trans. Electron Devices*, vol. 39, no. 6, pp. 1376-1386.

[6.2] J. B. Sampsell, "The digital micromirror device and its application to projection displays", in *Tech. Dig. 7th International Conference on Solid-State Sensors and Actuators*, Yokohama, Japan, June 1993, pp. 24-27.

[6.3] B. van der Schoot, S. Jeanneret, A. van der Berg, and N. F. de Rooij, " A silicon integrated miniature chemical analysis system", *Sensors and Actuators*, vol. B-6 (1992), pp. 57-60.

[6.4] K. Petersen, "The silicon micromechanics foundry", in *Proc. IEEE Micro Robots and Teleoperators Workshop*, Hyannis, MA, USA, November 1987.

[6.5] H. Baltes, D. Moser, R. Lenggenhager, O. Brand, and D. Jaeggi, "Thermomechanical microtransducers by CMOS and micromachining", in *Micromechanical Sensors, Actuators and Systems*, DSC-vol. 32, New York, 1991, pp. 61-75.

Acknowledgements

First of all, I like to thank Prof. Dr. N. F. de Rooij for giving me the opportunity to work in his group and for his enthusiastic support and guidance at any moment of the project.

Dr. C. Linder got me started on the polysilicon surface micromachining technology; his knowledgeable support and advice I acknowledge highly. For many inspiring discussions and for the fruitful collaboration on micromachined devices for nanoscale science, I would like to thank J. Brugger and Dr. N. Blanc. It is a pleasure for me to thank both of them also for reviewing my thesis. For the collaboration on silicon actuators with integrated tips, I owe thanks to P.-F. Indermühle. I appreciate greatly that P.-A. Clerc and S. Jeanneret were sustaining this work by their excellent technical support in the fabrication of the structures. Further, I like to thank all my colleagues from the Group de Rooij for help, fun, and a stimulating working environment.

Highly acknowledged are the discussions with Dr. J.-M. Moret and Dr. R. Vuilleumier from the CSEM. They shared with me their vast technological know-how and helped to found a good relationship between the IMT and CSEM, which was an important asset to the success of this work. For characterizing the micromirror array, the assistance of G. Perregaux, P. Debergh, P. Minguely was very important and greatly recognized. Further, I owe thanks to Dr. I. Kjelberg for performing the scattering measurements and to Dr. F. Sollberger for advices concerning the development of the aluminum surface micromachining process. The help and patience of M. Perdrix and C. Ketterer in creating beautiful illustrations, photographs and SEM pictures is highly appreciated.

The work on interference light modulators is based on a collaboration with Ascom Tech. It is a pleasure for me to thank O. Anthamatten, Dr. R. Bättig, and Dr. P. Vogel for inspiring conversations. Many insights into the working principles of these modulators and also ideas for new devices I acquired during discussions with Dr. P. Regnault from the CSEM. He also performed the calculations for the phase step modulator.

What I appreciated most during the work in the IMT-CSEM environment is that for any problem - may it be in electronics, chemistry, optics, mechanics, or simulation - I always found a knowledgeable expert, who was ready to share his know-how. While I am not naming all these persons, I do estimate their inputs highly and like to thank them all.

Further, I like to thank Prof. Dr. R. Dändliker, Prof. Dr. P. Renaud, and Dr. P. Vettiger for kindly agreeing to co-examine this thesis.

And, of course, many thanks to Nicolette Grob for her love and friendship during the whole time.

This work was supported by the Swiss Foundation for Microtechnology Research (FSRM 90/08).

Bibliography

V. P. Jaecklin, C. Linder, N. F. de Rooij, J.-M. Moret, and R. Vuilleumier, "Micromechanical polysilicon shutters and mirrors for light modulator arrays", in *Tech. Dig. 6th International Congress for Sensors and Systems Technology*, Nürnberg, Germany, October 1993, vol. 5, pp. 63-67.

V. P. Jaecklin, J. Brugger, C. Linder, P.-F. Indermühle, and N. F. de Rooij, "Micromachined overhanging *xy*-actuator with protruding tip for scanned probe devices", in *Tech. Dig. EUROSENSORS VII*, Budapest, Hungary, September 1993, p. 492.

V. P. Jaecklin, C. Linder, N. F. de Rooij, J.-M. Moret, and R. Vuilleumier, "Line-addressable torsional micromirrors for light modulator arrays", in *Tech. Dig. EUROSENSORS VII*, Budapest, Hungary, September 1993, p. 491; also accepted by *Sensors and Actuators*.

J. Brugger, P.-F. Indermühle, V. P. Jaecklin, C. Linder, and N. F. de Rooij, "Nanopositioniersystem", in *Mikromaschinen, Fachbeilage Mikrosystemtechnik*, Publication of VDI/VDE-Technologiezentrum Informationstechnik, me Bd. 7 (1993) Heft 5, p. 78.

J. Brugger, V. P. Jaecklin, C. Linder, N. Blanc, P.-F. Indermühle, and N. F. de Rooij, "Microfabricated tools for nanoscience", in *Proc. 4th Workshop on Micromachining, Micromechanics and Microsystems*, Neuchâtel, Switzerland, September 1993, pp. 105-114.

P.-F. Indermühle, C. Linder, J. Brugger, V. P. Jaecklin, and N. F. de Rooij, "Design and fabrication of an overhanging *xy*-microactuator with integrated tip for scanning surface profiling", accepted by *Sensors and Actuators*.

C. Linder, V. P. Jaecklin, and N. F. de Rooij, "Modeling and performance of electromechanical polysilicon actuators", submitted to *IEEE J. Microelectromech. Syst.*

V. P. Jaecklin, C. Linder, N. F. de Rooij, and J.-M. Moret, "Comb actuators for *xy*-microstages", *Sensors and Actuators*, vol. 39, no. 1 (1993), pp. 83-89.

V. P. Jaecklin, C. Linder, N. F. de Rooij, J.-M. Moret, R. Vuilleumier, "Mechanical and optical properties of surface micromachined torsional mirrors in silicon, polysilicon and aluminum", in *Tech. Dig. 7th International Conference on Solid-State Sensors and Actuators*, Yokohama, Japan, June 1993, pp. 958-961; also accepted by *Sensors and Actuators*.

J. Brugger, V. P. Jaecklin, P.-F. Indermühle, C. Linder, and N. F. de Rooij, "Fabrication of an Overhanging *XY*-Microactuator with Integrated Tip for Scanned Surface Profiling", in *Late News 7th International Conference on Solid-State Sensors and Actuators*, Yokohama, Japan, June 1993, pp. 8-9.

J. Brugger, V. P. Jaecklin, C. Linder, N. Blanc, N. F. de Rooij, "High-precision aligned silicon wafer bonding for a micromachined AFM sensor", in *Proc. 2nd Int. Symposium on Semiconductor Wafer Bonding*, Electrochemical Society Meeting, Honolulu, Hawaii, USA, May 1993.

V. P. Jaecklin, "Surface micromachining - a versatile technology for microactuators", in *Tagungsbericht Grundlagen und Technologie elektronischer Bauelemente*, Grossarl, Österreich, April 1993, p. 59.

V. P. Jaecklin, C. Linder, N. F. de Rooij, J.-M. Moret, R. Vuilleumier, "Optical microshutters and torsional micromirrors for light modulator arrays", in *Tech. Dig. IEEE Micro Electro Mech. Syst. Workshop*, Fort Lauderdale, FL, USA, February 1993, pp. 124-127.

V. P. Jaecklin, "Light modulators and deflectors", *UETP-MEMS course on Microactuators*, 1993, pp. 47-61.

V. P. Jaecklin, C. Linder, N. F. de Rooij, and J.-M. Moret, "Micromechanical comb actuators with low driving voltage", *J. Micromech. Microeng.*, vol. 2, no. 4, 1992, pp. 250-255.

C. Linder, L. Paratte, M.-A. Grétillat, V. P. Jaecklin, and N. F. de Rooij, "Surface micromachining", *J. Micromech. Microeng.*, vol. 2, no. 3, 1992, pp. 122-132.

J. Brugger, V. P. Jaecklin, R. Buser, C. Linder, and N. F. de Rooij, "Micromachined tools for nanometer-scale science", in *Proc. NATO ARW on Manipulations of Atoms under High Fields and Temperatures: Applications*; Lyon, France, July 1992, pp. 311-317.

V. P. Jaecklin, C. Linder, N. F. de Rooij, and J.-M. Moret, "Micromechanical comb actuators with low driving voltage", in *Tech. Dig. VDI/VDE International Conference on New Actuators*, Bremen, Germany, June 1992, pp. 40-45.

C. Linder, L. Paratte, M.-A. Grétillat, V. P. Jaecklin, and N. F. de Rooij, "Surface micromachining", in *Proc. 4th Workshop on Micromachining, Micromechanics and Microsystems*, Leuven, Belgium, June 1992, pp. 43-55.

V. P. Jaecklin, C. Linder, N. F. de Rooij, J.-M. Moret, R. Bischof, and F. Rudolf "Novel polysilicon comb-actuators for *xy*-stages", in *Tech. Dig. IEEE Micro Electro Mech. Syst. Workshop*, Travemünde, Germany, February 1992, pp. 147-149.

J. Hayes, V. P. Jaecklin, Y.-K. Kim, and D. Schwauger, "Characterization of the Conmag III Sputtering Source", *VARIAN SEG Report No. 192*, November 1990.

V. P Jaecklin, *The M2000 Recipe Book*, Varian SEG Publication, Palo Alto, CA, USA, April 1990.

D. Häusler and V. P. Jaecklin, "Prozessentwicklung für ein 50 Å Streuoxid", *SIEMENS com. no. 87'123*, October 1987.

Biography

Victor P. Jaecklin was born on May 21, 1964 in Palo Alto, California, USA. He received his diploma in physics in 1989 from the Swiss Federal Institute of Technology in Zürich (ETHZ). His masters project dealt with the development of a plasma etch process for etching contact holes in the SACMOS (Self-Aligned-CMOS) technology. The work was performed at Faselec Inc. (subsidiary of Philips) in Zurich. From 1989 to 1991 he was employed by Varian Associates Inc., Palo Alto, California, where he did process development for VLSI and ULSI semiconductor equipment; in the marketing department he was also responsible for technical customer support. In spring 1991, he joined the Institute of Microtechnology (IMT) of the University of Neuchâtel, Switzerland, where he started working as a research assistant on a project of the Swiss Foundation for Microtechnology Research (FSRM 90/08).

Apart from his research work on surface micromachined electrostatic microactuators, Mr. Jaecklin is involved with the preparing, organizing, and teaching of a COMETT (Community Programme for Education and Training in Technology) course on microactuators. Further, he is a member of the organizing committee for the International Conference on Micro- and Nanoengineering '94.